Dissertation
submitted to the
Combined Faculty of Mathematics, Engineering and Natural Sciences
of Heidelberg University, Germany

for the degree of
Doctor of Natural Sciences

Put forward by
Luis Pazos Clemens
born in: Ciudad Juárez, México

Oral examination: December 4th, 2023

Development and investigation of an integrated preclinical PET-OT system concept

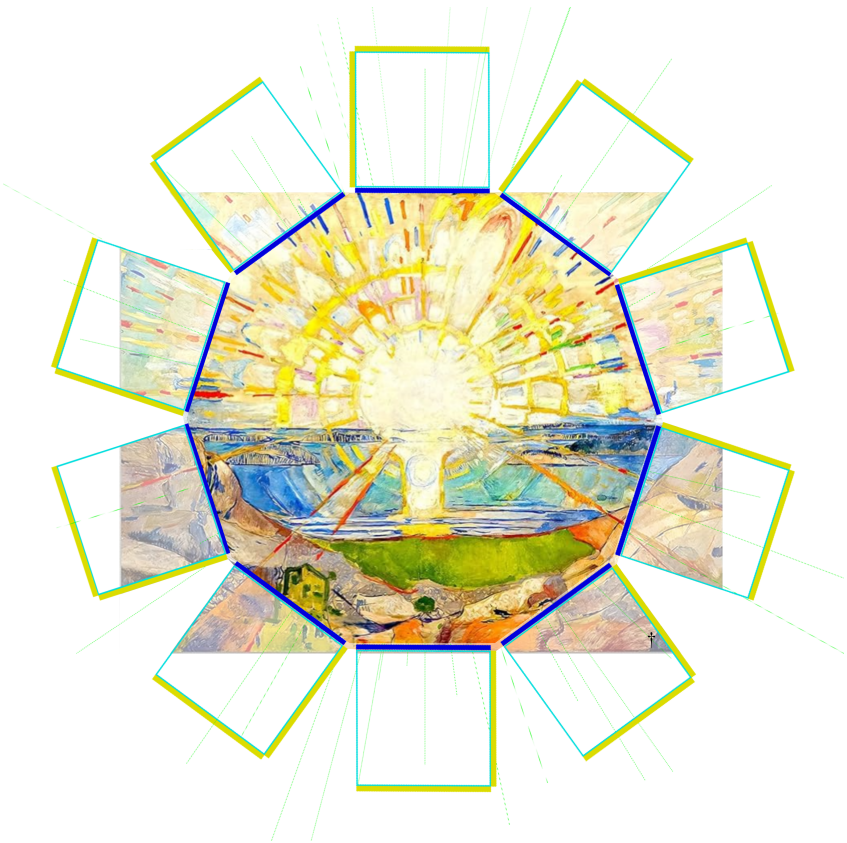

This work has been carried out
at the German Cancer Research Center (DKFZ) in Heidelberg
under the supervision of Dr. Jörg Peter

Referees: Prof. Dr. Mark Ladd
Prof. Dr. Oliver Jäkel

Summary

Efforts towards the development of a detector system designed for simultaneous optical and nuclear imaging, i.e. combining fluorescence/bioluminescence techniques with PET/SPECT modalities, have started over a decade ago. Given the potential that would be introduced by the capacity of simultaneously detecting gamma-rays and optical-probe photons, a concept for an integrated system being capable of achieving such task was developed in this work. The blueprint for an integrated preclinical PET-OT system consisting of detector modules that combine monolithic scintillating crystals with plenoptic detectors is presented. Each module of this system is specifically composed of a 25 x 25 x 25 mm LYSO crystal with two 8 x 8-channel photosensors of matching 2D size coupled to its back face and to another lateral face of the crystal in a perpendicular dual-readout configuration. The plenoptic detectors consist of a CMOS flat sensor of corresponding 2D size with a microlens array attached to them. A simulation and reconstruction framework for the investigation of monolithic-detector PET systems was developed for the conception and analysis of the proposed system. Within this framework, two alternative algorithms required for the operation of monolithic-detector PET systems were developed respectively based on a k-nearest neighbours and a convolutional neural network approach. The POI estimation FWHM-resolution of the former was found to be 0.68 mm, 0.66 mm and 0.52 mm in the x, y and z dimensions respectively for the monolithic-detector module in the proposed system. The latter presented a POI estimation FWHM-resolution of 0.42 mm, 0.41 mm and 0.49 mm in the x, y and z dimensions respectively. The crystal depth, the number of crystal faces to which a photosensor is coupled and the number of channels per photosensor were optimised in order to reach the final proposed design.

The performance of the system was evaluated through the analysis of standard PET figures of merit, namely its spatial resolution and geometrical efficiency. Spatial resolution values ranging between 0.58 mm and 1.24 mm FWHM of the point spread function of the system were obtained across its radial dimension. The geometrical efficiency presented a peak

value of 3.9% along its axial dimension. The imaging capabilities for both of the imaging modalities were assessed with the use of phantom simulations. A Derenzo PET phantom as well as a tumour-bearing mouse phantom were composed and investigated. The reconstruction of the Derenzo phantom using both of the proposed POI estimation algorithms yielded image results from which rods of 1.25 mm diameter could be clearly identified in the corresponding line profiles. The reconstruction of the simulated imaging acquisition of the mouse phantom yielded an activity distribution from which both relevant organs and the tumour could be clearly recognised. As a result of the performance evaluation and imaging assessments, the feasibility of the proposed multimodal system was demonstrated through outcomes that indicate a successful multimodal functionality with high PET performance characteristics. This work therefore contributes the development of a simulation and reconstruction framework for the design and investigation of monolithic-detector PET systems along with two high-performing algorithms used for their operation. As well as the proposal of the concept for an integrated multimodal PET-OT system with a demonstrated promising potential.

Zusammenfassung

Die Bemühungen um die Entwicklung eines Detektorsystems für die gleichzeitige optische und nukleare Bildgebung, d.h. die Kombination von Fluoreszenz-/Biolumineszenztechniken mit PET/SPECT-Modalitäten, begannen vor über zehn Jahren. In Anbetracht des Potenzials, das sich aus der Fähigkeit zur gleichzeitigen Detektion von Gammastrahlen und optischen Sondenphotonen ergeben würde, wurde in dieser Arbeit ein Konzept für ein integriertes System entwickelt, das diese Aufgabe erfüllen kann. Es wird der Entwurf für ein integriertes präklinisches PET-OT -System vorgestellt, das aus Detektormodulen besteht, die monolithische szintillierende Kristalle mit plenoptischen Detektoren kombinieren. Jedes Modul dieses Systems besteht aus einem 25 x 25 x 25 mm großen LYSO-Kristall mit zwei 8 x 8-Kanal-Photosensoren von gleicher 2D-Größe, die an die Rückseite und an eine andere Seitenfläche des Kristalls in einer senkrechten Dual-Readout-Konfiguration gekoppelt sind. Die plenoptischen Detektoren bestehen aus einem CMOS-Flachsensor mit entsprechender 2D-Größe, an dem ein Mikrolinsen-Array angebracht ist. Für die Konzeption und Analyse des vorgeschlagenen Systems wurde ein Simulations- und Rekonstruktions-Framework für die Untersuchung von PET-Systemen mit monolithischem Detektor entwickelt. Innerhalb dieses Framework wurden zwei alternative Algorithmen entwickelt, die für den Betrieb von PET-Systemen mit monolithischen Detektoren erforderlich sind und auf einem Ansatz mit k-nahen Nachbarn bzw. einem neuronalen Faltungsnetzwerk basieren. Die FWHM-Auflösung der POI-Schätzung wurde für das monolithische Detektormodul des vorgeschlagenen Systems mit 0,68 mm, 0,66 mm und 0,52 mm entlang der x-, y- und z-Dimension. Letzteres wies eine FWHM-Auflösung der POI-Schätzung von 0,42 mm, 0,41 mm bzw. 0,49 mm in den x-, y- und z-Dimensionen auf. Die Kristalltiefe, die Anzahl der Kristallflächen, an die ein Fotosensor gekoppelt ist, und die Anzahl der Kanäle pro Fotosensor wurden optimiert, um das endgültige vorgeschlagene Design zu erreichen.

Die Leistung des Systems wurde durch die Analyse der Standard-PET-Leistungskennzahlen,

d. h. der räumlichen Auflösung und der geometrischen Effizienz, bewertet. Für die räumliche Auflösung wurden Werte zwischen 0,58 mm und 1,24 mm FWHM der Punktantwortfunktion des Systems über die radiale Abmessung ermittelt. Die geometrische Effizienz wies entlang der axialen Dimension einen Spitzenwert von 3,9% auf. Die Bildgebungsfähigkeiten für beide Bildgebungsmodalitäten wurden mit Hilfe von Phantomsimulationen bewertet. Es wurden ein Derenzo-PET-Phantom sowie ein Mausphantom mit Tumor erstellt und untersucht. Die Rekonstruktion des Derenzo-Phantoms unter Verwendung der beiden vorgeschlagenen POI-Schätzalgorithmen lieferte Bildergebnisse, bei denen Stäbchen mit einem Durchmesser von 1,25 mm in ihren Linienprofilen eindeutig identifiziert werden konnten. Die Rekonstruktion der simulierten Bildaufnahme des Mausphantoms ergab eine Aktivitätsverteilung, aus der sowohl die relevanten Organe als auch der Tumor deutlich zu erkennen waren. Als Ergebnis der Leistungsbewertung und der Bildgebungsbeurteilungen wurde die Machbarkeit des vorgeschlagenen multimodalen Systems durch Ergebnisse nachgewiesen, die auf eine erfolgreiche multimodale Funktionalität mit hohen PET-Leistungsmerkmalen hinweisen. Diese Arbeit leistet daher einen Beitrag zur Entwicklung eines Simulations- und Rekonstruktions-Frameworks für den Entwurf und die Untersuchung von PET-Systemen mit monolithischen Detektoren sowie zu zwei leistungsstarken Algorithmen, die für deren Betrieb verwendet werden. Außerdem wird ein Konzept für ein integriertes multimodales PET-OT-System vorgeschlagen, das ein vielversprechendes Potenzial aufweist.

Contents

Introduction **1**

1 Positron Emission Tomography **5**
1.1 Physical principles of PET 6
1.1.1 Positron decay 6
1.1.2 Positrons in a medium 7
1.1.3 Gamma-ray interactions with matter 9
1.1.4 Scintillating crystals 10
1.2 PET instrumentation and operation 15
1.2.1 Conventional detectors 15
1.2.2 Silicon photomultipliers 18
1.2.3 Monolithic detectors 20
1.2.4 Coincidence sorting 21

2 System conception, optimisation and evaluation **25**
2.1 Design considerations and proposition 26
2.2 Simulation and reconstruction frameworks 28
2.2.1 PET subsystem 28
2.2.2 k-nearest neighbours algorithm 31
2.2.3 Convolutional neural network algorithm 38
2.2.4 Optical imaging subsystem 40
2.3 System design conception 40
2.3.1 PET subsystem optimisation 40
2.3.2 Optical imaging subsystem precursor 41
2.4 Proposed system 42
2.4.1 PET subsystem 43
2.4.2 Optical imaging subsystem 44

2.5 Performance evaluation 45
2.5.1 PET spatial resolution and sensitivity 45
2.5.2 Derenzo phantom imaging 46
2.5.3 Mouse phantom imaging 47

3 System development and performance results **51**
3.1 PET simulation and reconstruction framework 52
3.1.1 Initial trial with the *ReSCoGs A-kNN* algorithm 52
3.1.2 In-depth investigation of the *CoG* feature 55
3.2 System design conception 63
3.2.1 PET subsystem optimisation 63
3.2.2 Optical imaging subsystem precursor 67
3.2.3 Comparison between estimation algorithms 68
3.3 Performance evaluation 71
3.3.1 PET subsystem performance characteristics 75
3.3.2 PET subsystem's imaging capabilities 78
3.3.3 Bi-modal acquisition simulation 80

Conclusions **89**

Appendix **95**
List of figures 97
Glossary of acronyms 101
Scientific contributions 103

References **105**

Acknowledgements **111**

Introduction

They did not know it was impossible, so they did it

- Mark Twain

The field of medical imaging is constantly striving towards the goal of obtaining ever more accurate, precise and diverse information from the target being imaged in a way that is as non-invasive and convenient as possible. Such purpose is pursued through the development of new imaging methods and the continuous improvement and integration of those already in existence, hence the successful trend that has produced several multimodality imaging detectors over the past few decades. Some of the most widely used individual imaging techniques have been gradually merging to produce proficient systems such as PET/CT and PET/MRI that are able to simultaneously provide intrinsically co-registered functional and structural information, while granting practical and reconstruction advantages [1].

Along this direction, efforts towards the development of a detector system designed for simultaneous optical and nuclear imaging, i.e. combining fluorescence/bioluminescence techniques with PET/SPECT modalities, started over a decade ago [2]. Since then, different preclinical concepts have been proposed but as of today none of them has resulted in a feasible device. The main challenge hindering said task has thus far lain in the attempt to isolate the two different, yet potentially very similar, signals in a way that is both

accurate and practically convenient while minimising any negative cross-modality influence, such as sensitivity or spatial resolution degradation [3]. The level of integration between the two modalities in these systems has therefore been very diverse, from fully integrated concepts employing single detector modules for the detection of both signals to completely separated systems that nevertheless share the same field of view (FOV) contemporarily [4]. Such a type of bimodal imaging system would provide an unprecedented correlation between molecular and physiological information being locatable, simultaneous, co-registered and potentially time-resolved. The so far unharnessed complementarity of these two types of information occurs because, on the one hand, nuclear imaging reconstructs the position and concentration of radiotracers in a high-resolution quantifiable manner while on the other, optical imaging employs molecular probing systems, some of which can be circumstantially activated, that report on precise molecular or cellular processes [5, 6].

Said correlated information, obtained for instance with the use of combined probes, namely monomolecular multimodality imaging agents (MOMIAs), would be immediately applicable to the image reconstruction and cross-validating procedures currently needed to aid the ongoing emergence and translation of optical imaging techniques [7]. The other major prompt application of this type of technology belongs to the field of pharmacokinetics, where we could expect novel pharmacokinetic models incorporating optical imaging data that would advance drug development procedures. Another important application, in the field of oncologic biomedical research, consists in the imaging of preclinical tumour models, where metabolic activity and other physiological or molecular parameters such as protease activity could be simultaneously sampled [4]. It then becomes hard to exclude the prospect of the eventual incorporation of this multimodal technique into the clinical field, whether used for diagnostics, for tumour and therapy evaluation, for theranostics or for a new application yet to be recognised [7]. In short, the main imminent applications that would benefit from said information correlation, and that therefore motivate the development of such type of detector system, include drug development and pharmacokinetics, the study of tumour models and radiobilogy, and the advancement of optical tomography (OT) techniques themselves [4, 7].

In light of this potential for the introduction of such novel multimodal imaging technique, this work had as its main objective to develop the concept of a detector with the capability to detect both high energy photons, namely gamma-rays used in nuclear imaging, and optical photons, as obtained from bioluminescence and fluorescence imaging. Given the

applicability requirements already described, this detector must include the key characteristic of fully integrating the two subsystems so that they share the same field of view and so that their simultaneous use is possible. This objective was undertaken with the initial intention of achieving simultaneous PET and optical imaging in a preclinical context and with the outlook to potentially translate its use to the clinical field in the future.

In the field of PET instrumentation development, monolithic scintillating crystals have recently demonstrated to have advantageous characteristics that make them a potential alternative to the pixelated scintillation crystal blocks that are conventionally used. Two of their most attractive features are the capacity of achieving higher spatial resolution with intrinsic depth-of-interaction (DOI) information, and an increased detection efficiency resulting from the absence of the dead space normally introduced by the optical separators between crystal elements [8]. Unlike in nuclear imaging, tomographic image reconstruction in the context of optical imaging remains an arduous challenge with ample room for development due mainly to the high level of scattering undergone by optical photons in tissue. The use of plenoptic detectors has been therefore previously proposed as an approach to accomplish optical tomography [9]. Said devices consist of a microlens array placed in front of a conventional optical-photon imaging sensor. With such an arrangement it is possible to acquire both intensity and direction information of the light field produced by the object being imaged, thus obtaining different directional projections within one detector position. Acquiring images with a plenoptic detector at different annular positions around an object and employing the appropriate reconstruction algorithms makes it therefore possible to produce a 3D tomographic image [10].

In addition to the aforementioned advantages of monolithic-detector PET and the potentiality of plenoptic cameras for optical tomography, the compactness and simplicity that can be achieved with both instruments makes them excellent candidates to be merged into a multimodal imaging system. This work therefore proposes a new approach to this medical imaging instrumentation challenge by presenting the blueprint for an integrated preclinical PET-OT system consisting of detector modules that combine monolithic scintillating crystals with plenoptic detectors. A simulation and reconstruction framework for the investigation of monolithic-detector PET systems was developed for the conception and analysis of said proposed system. Within this framework, two alternative algorithms required for the operation of monolithic-detector PET systems were developed respectively based on a k-nearest neighbours (kNN) and a convolutional neural network (CNN) approach. In addition to this framework, another previously developed and proven simu-

lation tool that simplifies the investigation of plenoptic-detector optical imaging systems was employed. The development and characterisation of the proposed multimodal system was therefore primarily based on the conception and investigation of its PET subsystem through the pertinently created framework. An in-depth examination of this framework was thus required and carried out revealing its functionality and potential. The feasibility of the proposed system was thus evaluated through the investigation and optimisation of its components' characteristics and their impact on different performance criteria as well as on reconstructed-image quality.

The performance of the proposed system has been initially evaluated through the analysis of standard PET figures of merit, namely its spatial resolution and sensitivity. Furthermore, its imaging capabilities for both of the imaging modalities have been assessed with the use of phantom simulations. A Derenzo PET phantom as well as a tumour-bearing mouse phantom have been composed and investigated. The latter representing a realistic multimodal imaging situation in a preclinical context. As a result of the performance evaluation, the feasibility of the proposed multimodal system was demonstrated through its imaging outcomes that indicate a successful multimodal functionality with notable PET performance characteristics. The first main outcome of this work is therefore a simulation and reconstruction framework for the development and investigation of monolithic-detector PET designs along with two high-performing algorithms used for the operation of said types of systems. The other main outcome of this work is the concept for an integrated multimodal PET-OT system whose promising potential has been demonstrated through the use of computational simulations. These outcomes not only motivate the conduction of a new study to experimentally validate said potential but also strive to contribute to the transition towards monolithic detectors for the advancement of PET systems and the development of new multimodal techniques.

1

Positron Emission Tomography

What is essential is invisible to the eye

- Antoine de Saint-Exupery

This chapter describes the physical and technological principles of Positron Emission Tomography as an imaging modality. The physical processes by which gamma-rays are emitted from radiotracers and detected by PET scanners are presented. Furthermore, the main components of PET scanners as well as their characteristics and their corresponding operation are discussed. A particular section is devoted to the emerging use of monolithic scintillating crystals in PET detectors.

1.1 Physical principles of PET

Positron Emission Tomography (PET) is a nuclear imaging technique capable of revealing functional information about the subject being imaged. The reconstruction of the activity distribution emitted from radiotracers injected into the subject provides an insight of metabolic or physiological activities of interest. The retrieval of such information is achieved with a non-invasive procedure that has a high level of sensitivity [11]. As such PET has become a staple of oncology medicine and research, among other fields, applied through the use of imaging scans with clinical or preclinical PET scanners. The physical principles behind the PET imaging technique are described in the following sections.

1.1.1 Positron decay

One of the types of radioactive decay that unstable, usually proton-rich, nuclei can undergo is positron (β^+) decay. The positron (e^+), being the antiparticle of the electron, has the same mass and spin as an electron but a positive electric charge instead. In positron emission decay an unstable parent nuclide loses a proton that is converted into a neutron, thus making it an isobaric process where the daughter nuclide maintains the same total number of nucleons. Together with this conversion a positron and, because of lepton number conservation, an electron neutrino are emitted in this type of decay, as expressed by the following representation [12][13].

$$ {}^{\mathrm{A}}_{\mathrm{Z}}\mathrm{X} \longrightarrow {}_{\mathrm{Z}-1}{}^{\mathrm{A}}\mathrm{Y} + \beta^+ + \nu_e $$

Given that the daughter nuclide has one more proton than the parent nuclide and considering the neutrino mass as negligible, the calculation of the transition energy, or Q value, yields:

$$ \mathrm{Q} = [\mathrm{m}({}^{\mathrm{A}}_{\mathrm{Z}}\mathrm{X}) - \mathrm{m}({}_{\mathrm{Z}-1}{}^{\mathrm{A}}\mathrm{Y}) - 2\,m_e]\mathrm{c}^2 \tag{1.1} $$

where m denotes the atomic mass of the specified atom, m_e is the electron rest mass and c is the speed of light in vacuum. Being an exothermic process, β^+ decay must have a positive Q value and therefore the mass of the parent atom must be at least 1.022 MeV (twice m_e = 0.511 MeV) larger than the mass of the daughter atom. Any excess energy above this value will be split between the neutrino and the kinetic energy of the positron. This means that the transition energy of a specific β^+ decay dictates the maximum energy E_β^{max} that the emitted positron can have, equal to the Q value minus the minimum transition energy required of 1.022 MeV, as illustrated in Fig. 1.1 for the common PET radiotracer ${}^{18}_{9}\mathrm{F}$ [12][13].

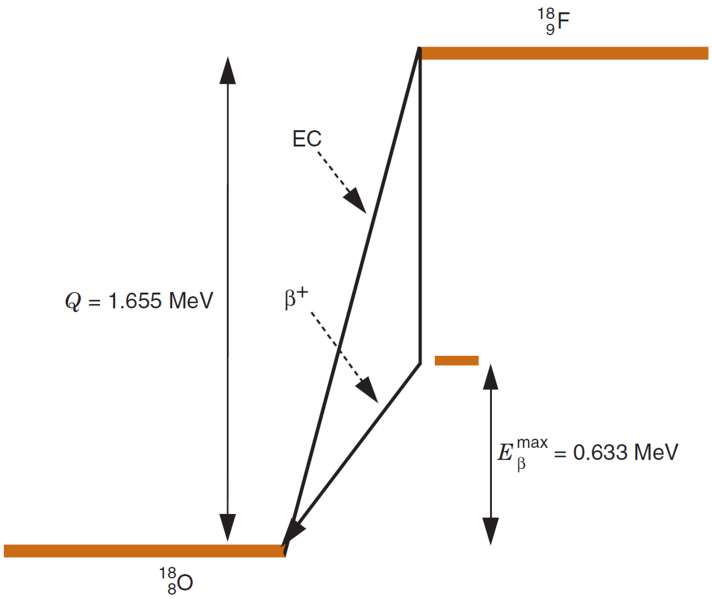

Figure 1.1: Decay scheme for the conventional PET radiotracer $^{18}_{9}$F, which decays both through positron emission (97%) and electron capture (EC). The maximum energy E_{β}^{max} that the emitted positron can have is given by Q - 1.022 MeV, the latter being represented by the vertical line. Diagram taken from [12].

1.1.2 Positrons in a medium

A positron emitted from a radiotracer that underwent β^+ decay will travel a certain distance that depends on its energy and on the composition of the medium. Along its path it loses its energy and changes direction through collisions with the atoms it encounters until it comes to rest by annihilating with an electron of the medium. The displacement of the positron after its contorted path is called the positron range and in water, a common surrogate of tissue, has a mean value of 0.6 mm and a maximum value of 2.4 mm [14].

Instead of directly annihilating with an electron at the end of its path, a positron can also bind the electron and together form an unstable exotic atom called positronium, whose mean lifetime in its most common ortho-positronium form is 1.8 ns in water [15]. In such a medium as tissue, positronium will also commonly decay through the annihilation of its positron with its electron or with another "picked-off" electron [15][16]. The electron-positron annhilation results in the production of two annhilitaion photons both with an energy of 511 keV, equal to m_e given the energy conservation requirement. In the rest frame of the annihilation and because of the momentum conservation requirement these photons are emitted in antiparallel directions. In the frame of the medium, however, both the positron and the electron are moving with their own momentum and thus angular vari-

ations in the order of 0.5 deg FWHM away from 180 deg are obtained in what is known as the non-collinearity effect [17]. Even though the two annihilation photons obtained are not emitted from a nucleus, in the PET community they are commonly referred to as gamma-rays given their 511 keV energy, and thus the term will also be used in this work.

The positron range and subsequent annihilation with an electron are illustrated in Fig. 1.2, where the non-colinear emission of the annihilation gamma-rays is also displayed. The spatial resolution of PET scanners depends on the ability to localise the radiotracer where the positron originates as accurately and precisely as possible. Since said task is tackled by tracking back the annihilation point in which the two gamma-rays were produced, Fig. 1.2 shows how the positron range is therefore one of the main factors intrinsically limiting the spatial resolution of PET scanners, and particularly preclinical ones [18]. The other main intrinsic factor being the non-colinearity error also indicated in Fig. 1.2.

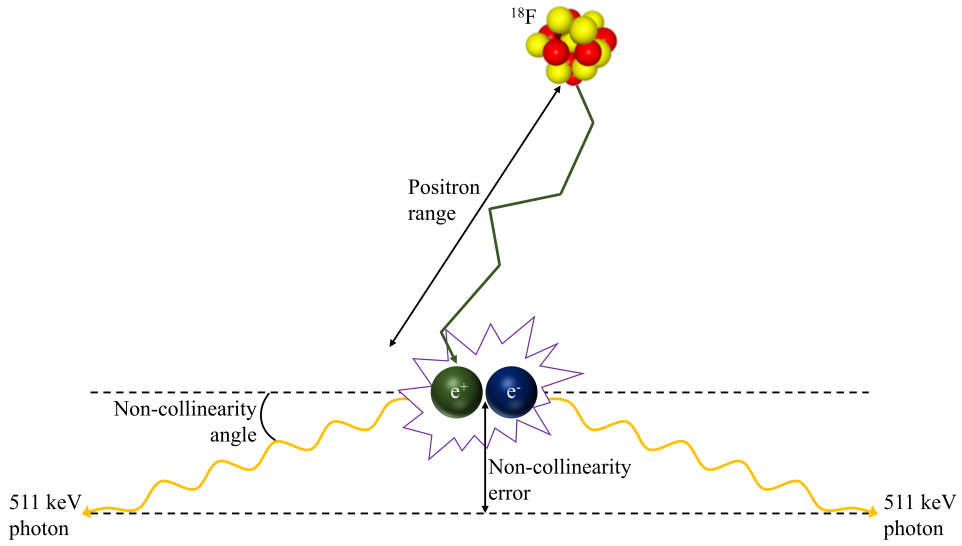

Figure 1.2: Diagram showing the path travelled by a positron after the β^+ decay of a $^{18}_{9}$F nucleus, as well as the direct annihilation with an electron that produces two anti-parallel 511 keV photons. The positron range, non-colinearity angle and corresponding non-colinearity error are indicated. Diagram not to scale.

1.1.3 Gamma-ray interactions with matter

The way in which gamma-rays interact with the medium that they are traversing depends on their energy as well as on the density and atomic number of the material. There are several types of interactions that gamma-rays can undergo with matter, of which the four most relevant to nuclear imaging are discussed below.

Compton scattering: In this type of interaction the gamma-ray inelastically "collides" with an outer-shell electron of an atom in the medium, whose binding energy is small enough, compared to the photon's, to be considered a "free" electron. The gamma-ray loses part of its energy as it is deflected, or scattered, by the collision at an angle θ, which is transferred to the electron, known therefore as a "recoil" electron. The energy transferred to the recoil electron is thus $E_{re} = E - E'$ where E is the energy of the incident gamma-ray and E' is the energy of the scattered gamma-ray. Taking into account the conservation of energy and momentum principles, the relationship between the scattered gamma-ray's energy and its scattering angle for a specific incident gamma-ray energy is given by the following equation:

$$E' = h\nu' = \frac{h\nu}{1 + \frac{h\nu}{m_0c^2}(1 - cos\theta)} \tag{1.2}$$

where m_0c^2 is the electron rest mass and $h\nu$ is the energy of the incident gamma-ray. The probability of Compton scattering directly depends on the number of electron targets available and thus scales linearly with the atomic number of the medium. As the energy of the incident gamma-ray is increased, however, said probability generally decreases, as shown in Fig. 1.3 for the scintillating material NaI(Tl) [12][19].

Photoelectric effect: In this interaction the incident gamma-ray is completely absorbed by an atom of the medium, which ejects an electron referred to as a photoelectron. The shell from which the photoelectron is emitted is with increasing likelihood closer to the nucleus and dictates, together with the energy of the incoming gamma-ray, the energy of the photoelectron as $E_{e^-} = h\nu - E_b$ where $h\nu$ is the energy of the incident gamma-ray and E_b is the binding energy of the target electron. The vacancy left behind in the shell of the ejected electron is then filled either by an electron from another shell or by the capture of a free electron, resulting in the possible emission of at least one characteristic X-ray. The probability of photoelectric absorption is approximately dependent on Z^4 and $E_\gamma^{3.5}$, where Z is the atomic number of the absorbing material and E_γ is the energy of the incident gamma-ray

[12][19].

Pair production: When an energetic photon has an energy of at least 1.022 MeV, twice the rest mass of the electron, it can interact with the Coulomb field of a nucleus and turn into a pair of β particles, one electron and one positron. In practice the probability for this interaction becomes significant only at gamma-ray energies above a few MeVs. The excess energy of the photon above the minimum requirement of 1.022 MeV is shared between the kinetic energy of the positron and that of the electron. The positron ejected form this interaction can then travel in the medium and annihilate with an electron producing two 511 keV photons as described in section 1.1.2. Given the minimum energy requirement, this type of interaction is negligible for the specific case of PET imaging [19].

Rayleigh scattering: Also known as coherent scattering, this processes constitutes an elastic collision between the incoming gamma-ray and the electrons in an atom, acting as a single target with which the gamma-ray interacts coherently. Even though the gamma-ray does not lose energy, its direction often changes. The probability of Rayleigh scattering is significant for energies below 50 keV and most prominent in atoms with a high atomic number. The importance of Rayleigh scattering in PET's fundamental interactions is therefore also negligible and even more so considering that the deflection angle decreases with increasing gamma-ray energy [12][19].

By way of example, Fig 1.3 shows how the probability that a gamma-ray interacts with a NaI(Tl) absorber depends on its energy and how this dependence is broken down into the first three interaction mechanisms described above. As will be discussed in the next section, said material is a referential inorganic scintillating material in the field of nuclear medicine. The relative prominence of these three types of interaction as a function of the energy of the incident photon and of the atomic number of the absorbing material is illustrated in Fig 1.4. In both figures, a red vertical dashed line is used to indicate the 511 keV energy of the annihilation photons key to PET, whereas in Fig 1.4 the effective atomic numbers of two referential scintillating crystal materials (NaI and LYSO) used in PET are indicated by horizontal dashed lines.

1.1.4 Scintillating crystals

Following the interaction of radiation, such as gamma-rays, with a material, the atoms of the material can be either excited or ionised. The subsequent recombination or de-excitation that occurs within these atoms results in an energy release that is most often in the form of thermal energy dissipation. Some materials, however, have the characteristic

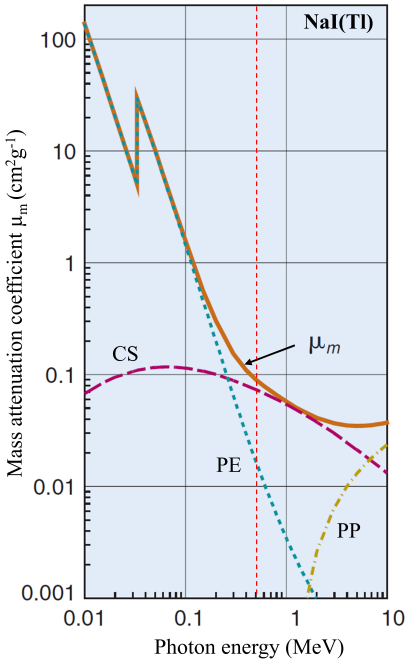

Figure 1.3: Probability of interaction between an incident photon and a NaI(Tl) medium. Total (μ_m), as well as individual Compton scattering (CS), photoelectric effect (PE) and pair production (PP) mass attenuation coefficient curves are displayed as a function of the energy of the photon. The red vertical dashed line indicates the 511 keV energy of the annihilation photons relevant for PET. Image adapted from [12].

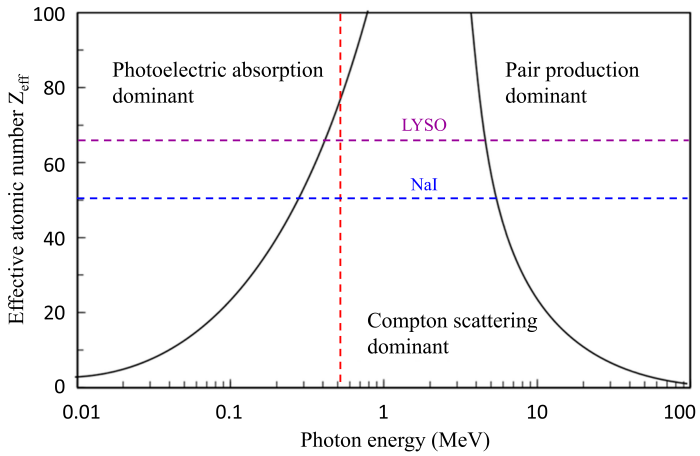

Figure 1.4: Relative importance of the three interaction mechanisms most relevant in nuclear medicine between energetic photons and matter. The predominant mechanism is presented as a function of the energy of the photon and of the effective atomic number of the absorbing material. Each of the three parameter-space sections delineated is labelled with the interaction mechanism that dominates it. The solid line curves delineating the sections represent the values for which the neighbouring interacting mechanisms are equally probable. A red vertical dashed line indicates the 511 keV energy of the annihilation photons relevant for PET. The horizontal dashed lines indicate the effective atomic numbers of two referential scintillating crystal materials used in PET. Image adapted from [20].

of releasing part of this energy by producing numerous visible or ultraviolet (UV) photons. Such type of material is known as a scintillating material, or scintialltor, as the processes by which it produces these photons are collectively referred to as scintillation [12][19]. Since the scintillators used in PET emit photons predominantly in the visible part of the electromagnetic spectrum, the scintillation photons will be hence possibly referred to also as scintillation light, visible photons or optical photons interchangeably.

In the broader field of radiation detection, scintillators are commonly categorised as being either organic or inorganic according to their chemical composition. One of the properties of all scintillators that makes them appropriate for nuclear imaging is that the number of photons produced by a scintillation event is proportional to the energy of the incident radiation particle. Moreover, the two types of scintillator can exhibit opposite behaviours when it comes to their main properties such as amount of light emitted per scintilaltion event and speed of the emission, which determines how suitable they are for specific applications. Even though inorganic scintillators, such as alkali halide crystals, are in general slower than their organic counterpart they tend to produce much more light per scintillation and in a more linear way. Together with their higher atomic number and density, these factors make scintillating crystals conventionally more appropriate for gamma-ray-related applications such as gamma-ray spectroscopy and nuclear medicine.

The main mechanism by which inorganic crystals scintillate is termed luminescence and depends on the altered band structure of the energy states that is obtained by doping the crystal's material. The altered band structure of inorganic scintillators as well as the luminescence mechanism are illustrated in Fig 1.5. The intrinsic valence and conduction bands formed by the lattice configuration of the atoms in a pure crystal are separated by a band gap, or forbidden band. Electrons in the valance band are bound to lattice sites, whereas those in the conduction band have enough energy to move within the lattice and are thus considered to be free. When a scintillating crystal absorbs energy, for example in the form of a radiation interaction, electrons might be excited from the valance band to the conduction band leaving holes behind. The subsequent de-excitation of an electron back to the valance band results in the emission of a photon whose energy depends on the band gap and is typically above the visible range in pure crystals. Since this is an inefficient process, in order to increase the scintillation probability and lower the energy of the emitted photons to the visible range scintillating crystals are generally doped with accordingly chosen impurities, also called activators. These impurities create new de-excitation sites in the lattice structure that add energy states within the band gap. The de-excitation of an

electron from such a site, termed luminescence or recombination centre, to the valance band represents a less energetic transition that thus results in the emission of a photon in the visible range. The emission spectrum of a scintillator depends therefore on the energy levels modified by the added activators [19]. Emission spectra examples of different scintillating crystals suitable for PET are shown in Fig 1.6.

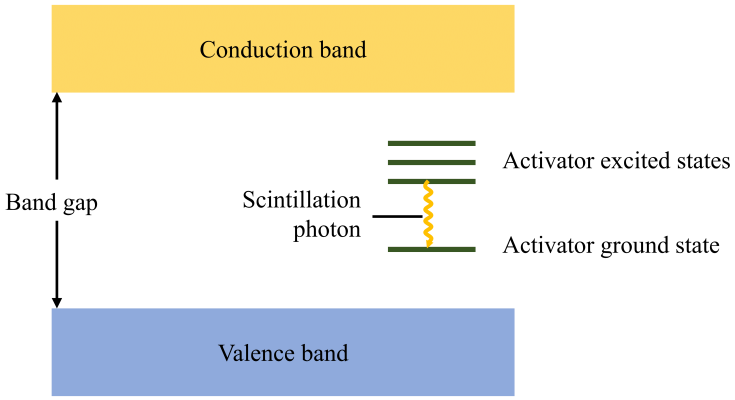

Figure 1.5: Schematic of the energy band structure of an inorganic scintillator. The emission of a scintillation photon through the de-excitation of an electron from an activator site is shown.

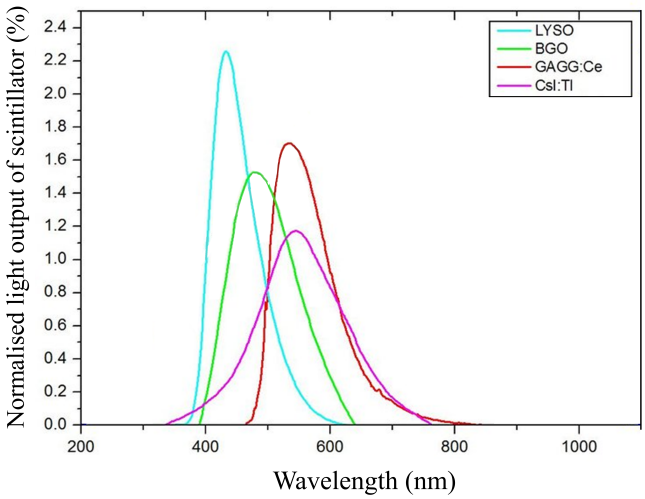

Figure 1.6: Normalised scintillation emission spectra of four inorganic crystals at room temperature. Figure adapted from [21].

The particular properties of scintillating crystals most relevant for nuclear medicine are defined in the list below and summarised in Table 1.1 for some conventional inorganic scintillators used in PET. As made evident by Table 1.1, the diverse properties of scintillating

materials together with other practical considerations such as price determine how appropriate they are as candidates, often presenting trade-offs, for specific PET designs.

Light yield: the number of scintillation photons emitted per unit energy deposited in the scintillator by an incident radiation particle [22]. Also known as light output.

Decay time: the time taken for the intensity of the scintillation light pulse to decrease to 1/e of its maximum value [23]. A single effective decay time is usually considered by averaging the multiple decay times that a scintillator may have corresponding to different light emission mechanisms.

Peak emission: the wavelength at which the peak of the scintillation emission spectrum occurs [24].

Hygroscopy: the characteristic of a material, given its chemical composition, of interacting with water molecules in the medium surrounding it. In the case of scintillators, it particularly refers to the process of moisture absorbance, a practical consideration to be made when designing a detector [25].

Table 1.1: Properties for some of the scintillating materials most commonly used in PET [12].

	NaI(Tl)	BGO	LSO(Ce)
Density (g/cm^3)	3.67	7.13	7.40
Effective atomic number	50	73	66
Index of refraction	1.85	2.15	1.82
Light yield (photons/keV)	38	8	20-30
Decay time (nsec)	230	300	40
Peak emission (nm)	415	480	420
Hygroscopic	Yes	No	No

1.2 PET instrumentation and operation

1.2.1 Conventional detectors

Scintillating materials and sensors capable of detecting their bursts of scintillation photons can be coupled into a single device known as a scintillation detector. A schematic diagram of the standard scintillation detector configuration used for radiation detection purposes is presented in Fig. 1.7, where its different components are shown. Traditionally, the sensor used to detect the scintillation photons was, and in many cases still is, a photomultiplier tube (PMT). In recent times, however, the use of solid-state sensors as substitutes for PMTs

has gradually increased for certain applications, PET being one of them [26]. These types of visible and near-visible photon sensors are sometimes collectively termed photodetectors but in this work they will be referred to as photosensors to avoid confusion with other terms. Photosensors have the capacity of producing an electrical signal that conveys information about the intensity of the scintillation light impinging on them. Together with the scintillator-inherent proportionality between that intensity and the energy of the incoming radiation particle, this property of photosensors makes scintillation detectors ideal for applications such as gamma-ray spectroscopy, calorimetry and nuclear imaging.

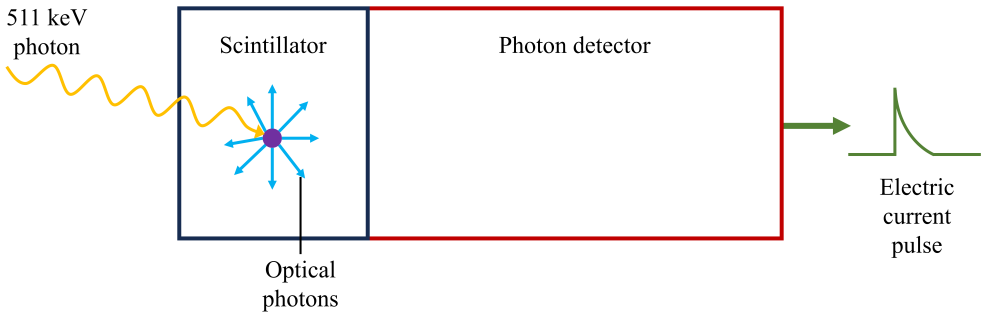

Figure 1.7: Simplified representation of a scintillation radiation detector composed of a scintillator coupled to a PMT. The detection of a scintillation process created by the interaction of a 511 keV gamma-ray is exemplified. Reproduced from [27].

Scintillation detectors are the building blocks of conventional PET scanners. The typical design of a fundamental PET module, known as a block detector, consists of a rectangular scintillating crystal block coupled to an array of PMTs or silicon photomultipliers. The majority of the PET scanners presently used in hospitals, which were introduced at the end of the last century and the beginning of the current one have modules with this type of block detector design employing PMTs [28]. A classic example of a block detector with an array of four PMTs is presented in Fig 1.8. As observed in Fig 1.8, the scintillating crystal block is transversely segmented into a square array of individual crystal elements that are optically isolated form each other by a thin layer of a reflective material. The reflective layer between segments and on the front gamma-ray-entrance face of the block has also the purpose of improving the scintillation light collection and transport towards the PMTs. The interface between the scintillation block and the windows of the photosensors consists of a coupling material with an appropriately chosen index of refraction that reduces the probability of internal reflection for the scintillation photons impinging on it. The whole block detector is sealed in a light and air-tight casing, or jacket, usually made out of aluminium or stainless steel that, apart from protecting its fragile components, isolates the

detector from external photons and humidity [12][29].

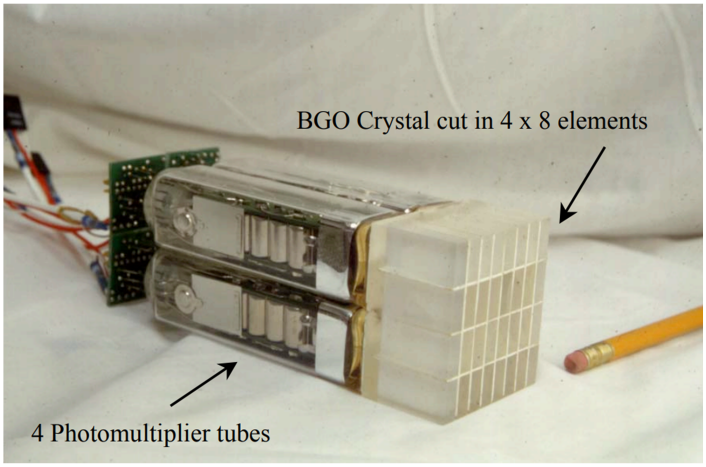

Figure 1.8: Photograph of a conventional PET block detector configuration. Two of the four PMTs employed can be seen coupled to the segmented crystal block. The metal jacket enveloping the detector has been removed in order to see its inner components. Reprinted from [29].

As can bee seen in Fig 1.8, the transversal segmentation of the crystal block does not span its whole depth, i.e. the dimension along the axis orthogonal to the back crystal face coupled to the photosensors. Close to this "photosensing" crystal face, or optical window, the segmentation has a variable pattern in which the crystal elements have different grouped depths. At the "photosensing" crystal face the segmentation is completely absent. This partial and variable segmentation-depth design allows the scintillation light emitted from any crystal element to spread towards all PMTs in the array, which collectively detect it by "sharing" the photons comprising it[1]. Hence the term light sharing is often used to describe this feature.

The specific segmentation-depth pattern used to delineate crystal elements is designed in order to obtain a unique collective PMT-response for scintillations occurring in each element. In other words, the scintillation light distribution reaching the optical window, and thus the corresponding position-weighted signal obtained from the PMT array, are proportional to the location (crystal element) where the gamma-ray interacted. Given this

[1]In some cases, and particularly in modern segmented block detector designs that employ solid-state sensor arrays, the segmentation does span the whole block depth. In this case a layer of high-transmittance-material is added between the crystal block and the photosensor array. Known as a light guide, this component allows the scintillation light coming from a specific crystal element to spread towards all photosensors as it does in a partial segmentation-depth design [30][31].

proportionality, two-dimensional coordinates can be used to represent a scintillation distribution detected by the photosensing array and thus determine the corresponding crystal element where it originated. A common type of positioning algorithm used to obtain said coordinates is presented below, where A, B, C, and D represent the intensity of the signal produced by a specific PMT in a 2 x 2 array [32].

$$x = \frac{(B+D)-(A+C)}{A+B+C+D}\ , \quad y = \frac{(A+B)-(C+D)}{A+B+C+D} \tag{1.3}$$

An example of a block detector configuration with 12x12 crystal elements coupled to a 2x2 PMT array is illustrated in Fig. 1.9 (left). The four circular PMTs are labelled in accordance to Eq. 1.3 and the crystal elements are superimposed to them. A so-called flood map of a detector can be obtained by exposing it to a gamma-ray source in such a way as to obtain numerous scintillation interactions that span the whole crystal volume as uniformly as possible. In a flood map the computed x,y coordinates of all the recorded scintillation distributions are presented together as a scatter plot where an isolated region of high intensity appears in correspondence to each one of the crystal elements. The flood map thus demonstrates how well a detector design is able to resolve the crystal element where a gamma-ray interaction occurred and to distinguish between all elements. A flood map obtained from a real block detector with the configuration illustrated in Fig. 1.9a is presented in Fig. 1.9 (right).

1.2.2 Silicon photomultipliers

As previously anticipated, the advent of solid state photodetectors had a strong influence on PET design through the gradual replacement of the PMT by the silicon-based photosensor known as a silicon photomultiplier (SiPM) [34]. In the present time, this phenomenon has reached the extent of the SiPM becoming the photosensor of choice for most current and imminent state-of-the-art PET scanner designs [35]. As solid state devices, SiPMs allow for more geometrical versatility in PET detector design by being more compact and less fragile than PMTs, which have a vacuum-sealed glass casing [36]. In order to obtain a readable amplified signal, the initial number of electrons generated at the photocathode of a PMT is sequentially multiplied with the use of a high voltage usually in the 1 kV range, thus making their performance susceptible to the presence of magnetic fields. SiPMs are instead operated with lower voltages in the order of tens of Volts and are not affected by the presence of magnetic fields, which is an advantageous property that makes the integration of SiPM-based PET and MRI techniques possible [36, 37]. Furthermore, modern SiPMs have reached gain values and time resolutions comparable to those of PMTs while

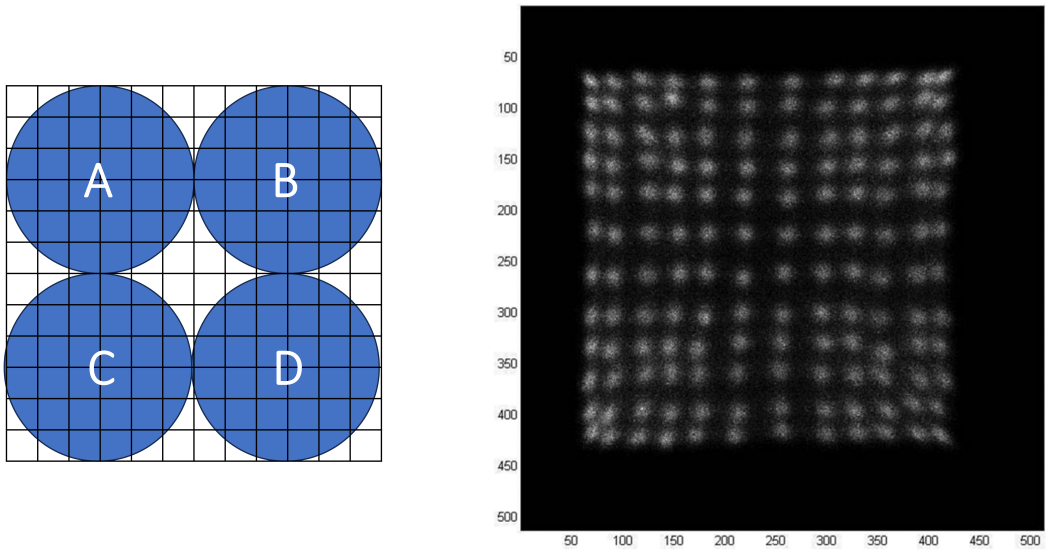

Figure 1.9: Left: Schematic of the cross-section of a PET block detector configuration segmented into 12 x 12 crystal elements coupled to 2 x 2 PMTs, labelled by letters. Right: Flood map obtained for a real block detector module with the configuration depicted on the left. Source: [33].

exhibiting higher sensitivity than PMTs and allowing for a diverse range of pixel sizes and arrangements [37, 38].

The SiPM, or sometimes also referred to as a Multi pixel photon counter (MPPC), is a solid state photodetector composed of micropixels that are connected to each other in parallel yielding typical densities that vary from hundreds to thousands of micropixels per millimetre squared [39]. A photograph of a typical single-channel SiPM with a squared shape is shown in Fig. 1.10a, where all its micropixels (in this case 900) can be identified. Each micropixel, sometimes referred to simply as pixel, contains an Avalanche photodiode (APD) that acts as a single photon counter, which is connected to a resistor in series, as illustrated in Fig. 1.10b. Each micropixel has a silicon multilayered structure where each layer has a different type and level of doping as indicated in the simplified example given in Fig. 1.10b. The micropixels are reverse-biased with voltages that are 10-20% above the breakdown voltage required for the APD to conduct after a new electron-hole pair is created by the impingement of a photon. Above this voltage, when the photon strikes the micropixel the high electric field created by the voltage results in a Geiger avalanche effect. The avalanche is produced as electron-hole pairs are drifted by the electric field at high velocities with enough kinetic energy to release more electron-hole pairs through ionisation, in a chain reaction manner. The micropixel and thus the SiPM is therefore said to

operate in Geiger Mode with typical gains between 10^5 and 10^6 [40].

Just like in a Geiger-Müller tube the output charge created by the avalanche within one micropixel has always the same magnitude regardless of the initial number of charge carriers produced by the photon interaction. This means that each micropixel on its own acts as a binary photon detector but an analogue detection is obtained from the SiPM as a whole by collecting this binary information from all the micropixels. Given the fixed number of micropixels and their Geiger-mode operation it is evident that the analogue behaviour of the SiPM and its linearty is limited by its dynamic range and by single-micorpixel saturation effects. The resistor present in every micropixel serves as a quencher with the purpose of terminating the avalanche effect. As the effect propagates it increases the current being transmitted through the resistor which results in the creation of an electric field with an opposite direction to that of the initial one quenching the avalanche until its termination [40].

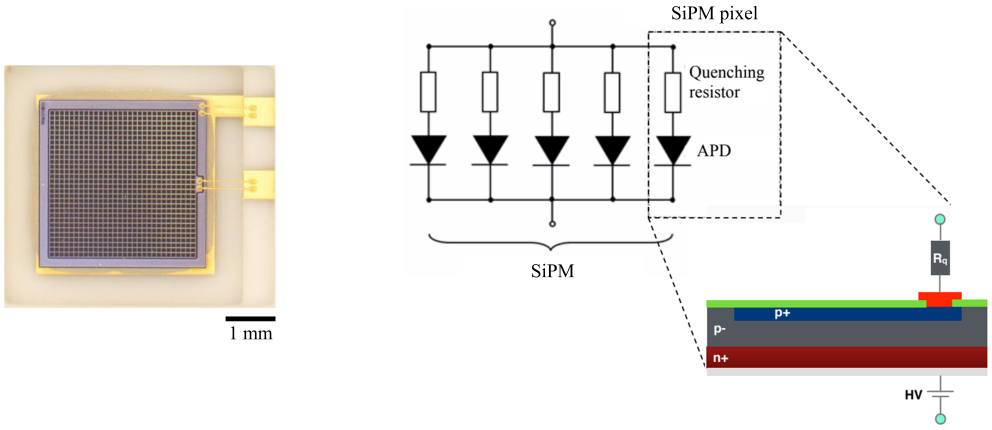

Figure 1.10: Left: Photograph of a single-channel SiPM. Right: Diagram of the electronic structure of a SiPM and example of the semiconductor structure of each pixel. Diagram modified from [41].

1.2.3 Monolithic detectors

Several different approaches have been proposed in the past few decades to improve the spatial resolution of PET scanners. Two of the these regard expanding the limits of conventional scintillating crystal sizes, each however, in opposite directions. In pixelated crystal detectors the POI determination resolution is directly given by the crystals' cross-sectional size. Crystal sizes of down to 0.5 mm have therefore been proposed in the past. With such configuration, higher spatial resolutions have been achieved at the cost, however, of a lower

scanner sensitivity [11]. The other approach, on the contrary, consists in using one single monolithic crystal per module with a volume corresponding to that of the entire pixelated array that would be employed in a conventional design. In this case with no crystal pixels, the need of optically isolating material to separate pixels is absent and thus the whole crystal volume is active, resulting instead in a higher detection sensitivity.

In order to characterise the events obtained from gamma-ray interactions within a monolithic crystal, and in particular the position at which the interaction occurred, the use of an additional algorithm is required. This position is often referred to as the point of interaction (POI)[2] of the impinging gamma-ray. This type of algorithm can be based on analytic, statistical or machine learning methods that in all cases are based on the inverse mapping of the scintillation light distribution recorded at the crystal's photosensing face, back to its emission point. With most of these techniques information about the depth at which the event occurred along the crystal is also retrievable, a feature that is not present in conventional segmented detectors. The acquisition of scintillation light distributions is possible due to the use of positioning-sensitive photomultiplier tubes or SiPM arrays with several channels (known also simply as SiPMs) coupled to at least one of the crystal faces [42]. A photograph displaying various sizes and configurations of SiPM arrays such as those that make monolithic detectors possible is presented in Fig. 1.11. It must be noted that statistical and machine learning algorithms used for the estimation of gamma-rays POIs come with the requirement of a physical calibration process necessary to obtain the reference data that characterises the detectors' response.

1.2.4 Coincidence sorting

The PET imaging technique relies on the detection of the correlated back-to-back gamma-rays emitted from the annihilation of a positron with an electron. The positrons are being in turn emitted by a radiotracer injected into the subject and travel only the short positron range, previously discussed, before annihilating. The capacity of retrieving the paths distended by gamma-ray pairs, along which their creation point lies, is thus what allows PET to identify the distribution of the radiotracer within the subject and provide the corresponding biological information of interest. This is accomplished by a coincidence sorting mechanism that requires the characterisation of all gamma-ray interaction events based on their time-stamp, the energy deposited by them in the corresponding detector and their global position within the scanner. By applying an energy window requirement to the de-

[2]The reader is invited to memorise this acronym hereafter very often used. Point of interaction (POI).

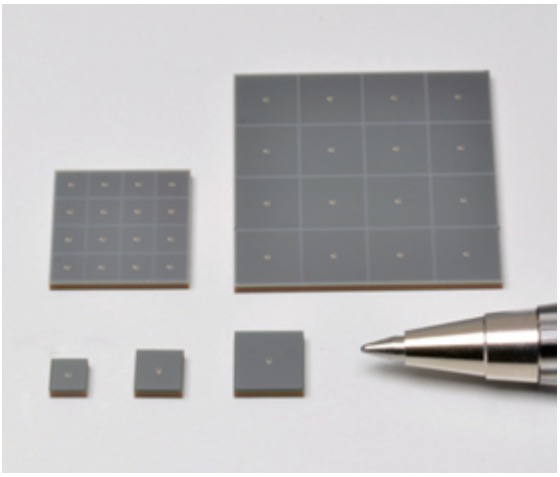

Figure 1.11: Photograph displaying various sizes and configurations of SiPM arrays. Reprinted from [41].

posited energy, the events obtained from scattered gamma-rays that thus exited the straight back-to-back path are excluded. By applying a coincidence time window, events with time-stamps within it can be considered as possibly coming from the same positron annihilation.

The positions within the scanner, given either as a crystal segment location or a POI in a monolithic crystal, of two coincident gamma-rays can then be connected through a so-called line of response (LoR) that represents their path and thus the region where their emission could have occurred. The collection of all LoRs corresponding to a PET acquisition is then the PET data that can be represented in different formats such a list-mode or histogram data and subsequently used to reconstruct the source distribution in the scanner's FOV. Given the presence of scattering, the ratio between the coincidence window and the time that takes the gamma-rays to reach the scanner, and the high level of activity usually employed, not all coincidences detected as such actually belong to correlated back-to-back gammas. Instead, three types of coincidences, illustrated in Fig. 1.12 can be obtained and are defined as follows:

True coincidences: also known simply as Trues, consist in the detection two gamma-rays whose back-to-back emission path was not deflected by scattering or by the non-colinearity effect away from a 180-degree path. Their emission point thus indeed lie along the LoR obtained by them.

Scattered coincidences: obtained from the detection of two gamma-rays emitted by the same positron annihilation where at least one of them got deflected away from a

colinear path either after being scattered or due to the non-colinearity effect. In this case their emission point does not lie along the LoR obtained.

Random coincidences: in which two gamma-rays detected within the same coincidence window were actually emitted by different positron annihilations. In this case the emission points of both gamma-ray are non retrievable and instead an LoR is obtained along which neither of them lies.

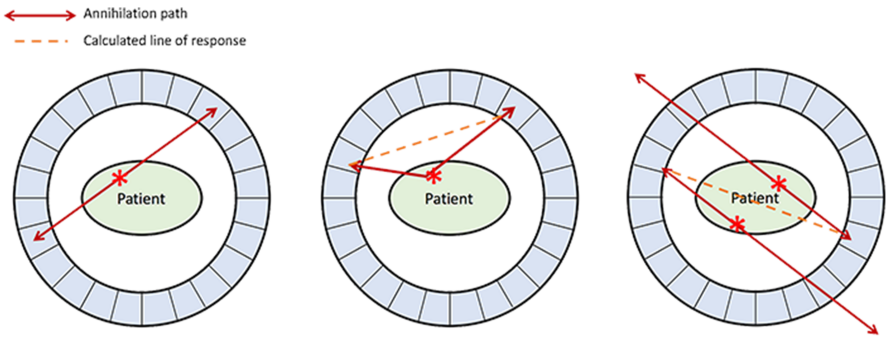

Figure 1.12: Diagram illustrating the three types of coincidence events that can be detected by a PET scanner. From left to right these are: true, scattered and random coincidences. Both the real annihilation path and the obtained LoR are indicated for each case. Reprinted from [11].

2

System conception, optimisation and evaluation

Imagination is more important than knowledge

- Albert Einstein

In this chapter the methodology used in order to develop the concept of an integrated PET-OT system is presented. The procedures employed to design and evaluate each of the subsystems are described in detail, both of them consisting in dedicated Monte Carlo simulation and image reconstruction frameworks. For the PET subsystem a workflow that also includes gamma-ray POI estimation algorithms was created in order to focus on the investigation of monolithic-detector designs. The system optimisation processes based on these frameworks as well as the concept design being proposed are explained. Finally, the methods and criteria used to evaluate the performance of the subsystems both in the optimisation process and in the final concept are described.

2.1 Design considerations and proposition

In light of the advantages of monolithic detectors and the potentiality of plenoptic cameras for optical tomography presented in Ch. 1 these two types of instruments were identified as the PET and OT subsystem candidates of choice. Considering the compactness and design simplicity that can be achieved with both instruments they were further recognised as optimal for being fully merged into an integrated multimodal PET-OT imaging system. Previously proposed concepts for such type of system involved a higher level of mechanical complexity introduced by components such as large mirrors, numerous optical fibres or rotational stages. Moreover, they had special characteristics that resulted in additional complications or loss of performance, such as the need to have the subject in contact with the scintillating crystals or to increase the radius of the system's bore [2, 3, 4, 43]. Fully integrated concepts were based on the use of a single photosensor per detector module employed to detect both gamma-rays and optical photons coming from radiotracers and optical probes in the subject respectively [2, 44]. This required the entrance face of the scintillator block not to be light-covered, as is customary, but instead to be completely exposed or covered by a dichroic mirror that would let optical-probe photons enter it but would reflect scintillation photons back in. A simplified schematic of this detector concept is illustrated in Fig. 2.1 (left) where it is labelled as a *distinguishing* concept based on the mechanism used to separate the two different types of events. Given that the amount of scintillation photons produced by a gamma-ray interaction in the crystal is much higher than the number of optical-probe photons reaching and traversing the crystal, their respective signals were distinguished by the very different intensities of their corresponding photosensor output signals. As a consequence of this event separation mechanism the two types of events cannot be detected simultaneously and a veto must be used when a scintillation event is being recorded [2, 44].

To address the aforementioned complications and disadvantages the system concept being proposed by this work, illustrated in Fig. 2.1 (right), uses a *sieving* event separation mechanism instead. In this case, a second type of photosensor is attached to the entrance face of the scintillator block and thus detects the optical-probe photons coming from the subject before they are able to reach the crystal. The gamma-rays coming form the radiotracers simply go through the photosensor and can then interact in the crystal and be detected, as if the second photosensor was a sieve that lets them through while instead stopping the optical-probe photons. As mentioned above, the type of photosensor deemed most appropriate for this purpose was the plenoptic camera and the crystal configuration

proposed to match it is the monolithic crystal one, indicated by the solid-line brown rectangle in Fig. 2.1. A PET-OT system of this type has minimal cross-subsystem leakage and presents event time stamping capabilities for both types of signals, given by the non-integrative operation modes of both photosensors. It does not require the subject to be in contact with any part of the detectors, neither does it require any external components such as mirrors or optical fibres, and thus leaves ample space for the use of excitation lasers required by fluorescence optical tomography. Lastly, it is MRI-compatible and thus presents the opportunity for further future multimodality.

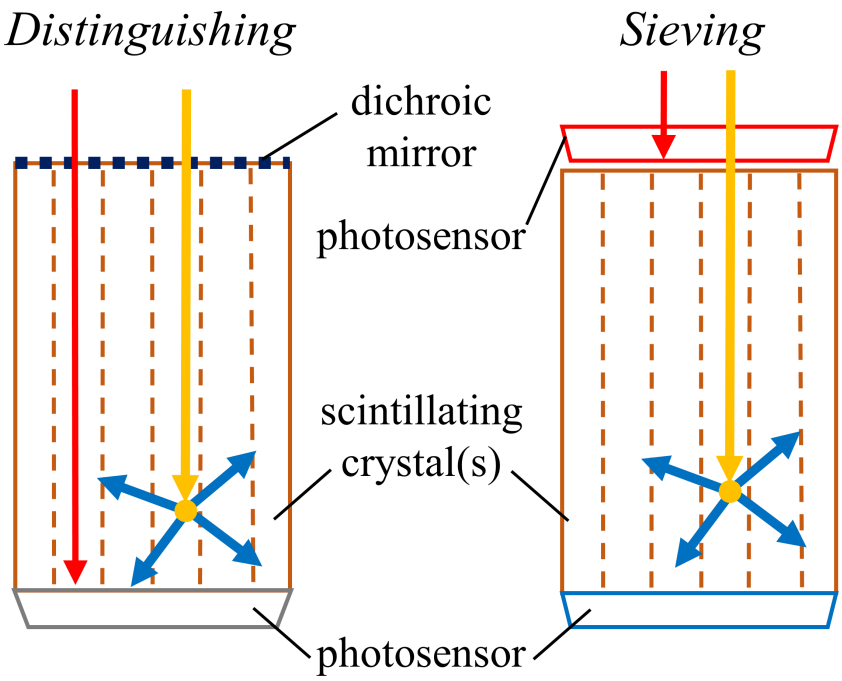

Figure 2.1: Comparison diagrams of two different design approaches for a bi-modal PET-OT detector module. Gamma-rays are shown as yellow arrows, while scintillation photons as blue ones and photons emitted by optical probes as red ones. The brown vertical dashed lines represent the optional segmentation of the scintillating crystal block into separate elements. Left: *Distinguishing* concept suggested by previous works where the same photosensor is used to detect both the scintillation photons and the photons coming from optical probes in the subject. The use of a dichoric mirror ensures that the former stay trapped in the crystal(s) while the latter are allowed to to enter it. Right: *Sieving* concept proposed by this work were the photons coming from optical probes in the subject are detected by a photosensor at the frontal face of the crystal(s) preventing them from entering it. While the gamma-rays from radio-tracers in the subject can go through it to enter the crystal(s) and scintillate.

2.2 Simulation and reconstruction frameworks

Given the versatility, convenience and accuracy of computational simulations based on Monte Carlo methods, they have been chosen as the main tool to be used in this work. The aforementioned characteristics make them highly suitable for investigating the structures and mechanisms of each imaging subsystem down to the level of individual photons. One of the main advantages that simulations have is the fact of providing a ground truth, meaning that the exact information describing every single particle interaction, such as its position and energy deposition, are inherently available. This means that the performance of any system being simulated under realistic conditions can be compared to the corresponding ideal conditions, a procedure that is conversely limited and cumbersome in real experiments. Furthermore, another obvious advantage is the possibility of simulating countless different geometries without the need of actually building them, which facilitates and encourages the development of new types of systems, however unconventional. In order to study the feasibility of such an integrated PET-OT system as mentioned in the previous section, a separate dedicated framework, based on Monte Carlo simulations and image reconstruction, was therefore developed for each of the two subsystems, representing different imaging techniques. Both frameworks are described in detail in the following subsections.

2.2.1 PET subsystem

In order to be able to study the monolithic-detector PET subsystem on which the multimodal system being proposed is based, a simulation and reconstruction framework for the investigation of monolithic-detector PET systems was developed. The scheme takes as initial input the combination of scanner and phantom geometry being investigated in the form of a macro for the Gate Monte Carlo simulation toolkit (Opengate collaboration [45]). As its final output, it produces a reconstructed image of the corresponding simulated PET acquisition after following the workflow described below. To the knowledge of the author there is no publicly available tool that allows the complete simulation to reconstruction process for the specific case of monolithic-detector PET designs. Hence the need for the development of intermediary steps, between the input design and the output image of this framework, that are able to produce appropriate PET data after the execution of a POI estimation algorithm. Along this workflow, illustrated in Fig. 2.2, the different operational characteristics particular to monolithic-crystal designs can be therefore investigated by individually evaluating them and by assessing their impact on the final reconstruction

output.

Gamma-rays (Fig. 2.2A-B)

The workflow begins with the gamma-ray production and interaction simulation in Gate according to the phantom's activity distribution and the system's configuration. The Penelope low energy physics list from GEANT4 is chosen as the model for the physical processes. From this initial step the gamma-ray points of interaction (POIs) where photoelectric absorption occurred within the scanner layout are obtained as coordinates in the reference frame of the monolithic crystal where they took place, along with its crystal identification number. These POIs are then coincidence-sorted with the specified energy and coincidence-time windows.

Scintillation photons (Fig. 2.2C)

The coincidence-sorted POIs are then used as emission origin points for scintillation-light distributions simulated with a dedicated Monte Carlo method previously developed for modelling light transport in monolithic crystals. A defined number of individual scintillation photons are generated and isotropically emitted at the POIs inside the monolithic crystal. The number of photons produced is established according to the scintillation characteristics of the crystal material employed. Each photon is propagated within the crystal where it may be scattered, absorbed, internally reflected or transmitted out of the crystal block depending on the optical characteristics of the material, its surface conditions and the sensor photon detection efficiency (PDE) being considered. Given the opaque nature of crystals, the probabilities for light scattering and absorption are essentially inconsequential, thus yielding comparatively fast photon propagation without the need of extensive variance reduction techniques.

Once the photon intersects one of the crystal faces its survival probability is added to the corresponding discretised sensor pixel, thus forming an integral fluence image for that face. This process repeats for the number of light photons being simulated per photoelectric absorption. After which, the fluence images obtained are stored and cleared for the next scintillation emission. The sizes of the faces and their sensor pixels determine the dimensions of 2D arrays that represent the fluence images. Said sizes be chosen to resemble the two-dimensional size and number of channels of conventionally used light sensors such as SiPM arrays or position sensitive PMTs.

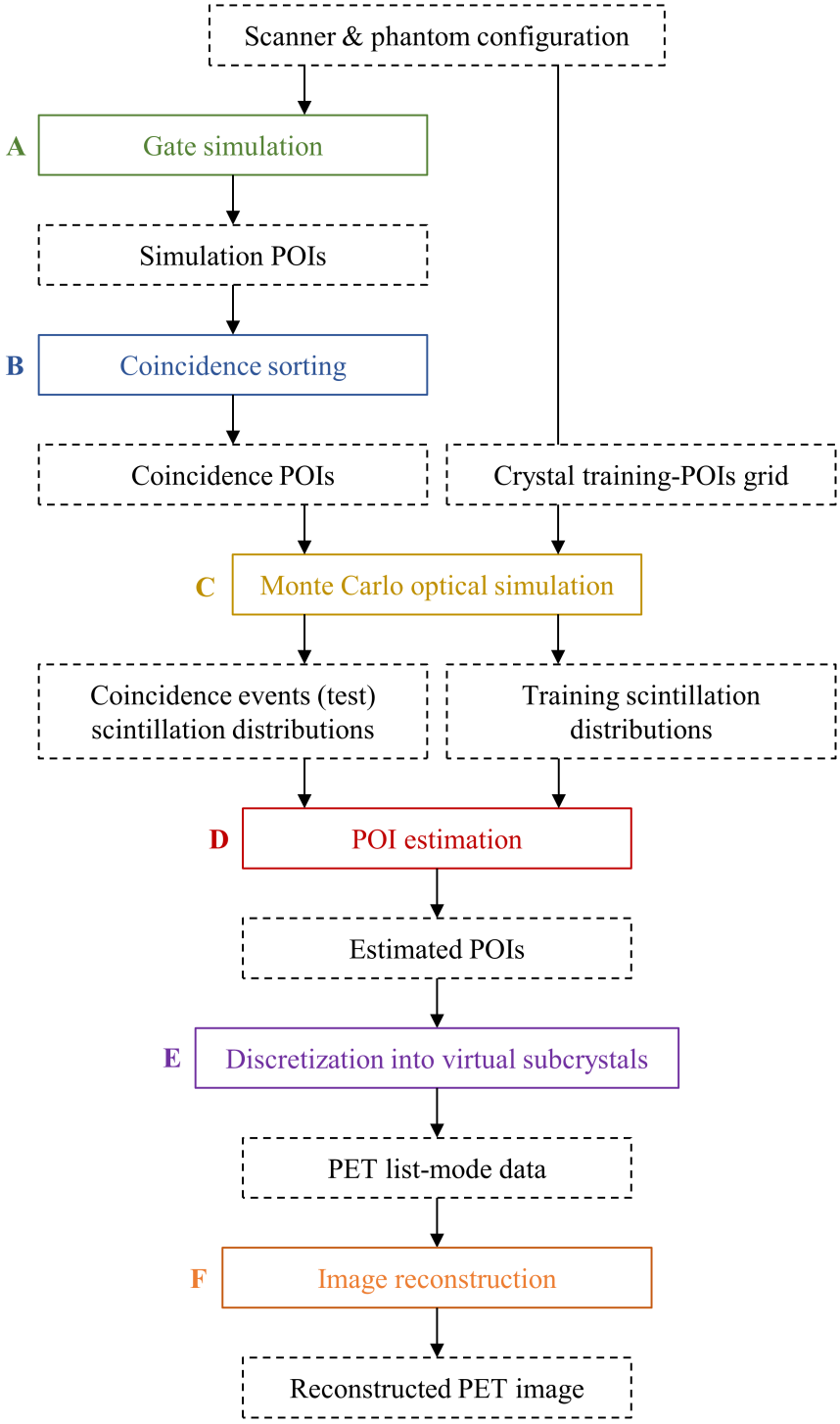

Figure 2.2: Simulation and reconstruction framework developed for the investigation of monolithic-detector PET systems. Each of its main stages are framed by coloured solid-line boxes while their inputs and outputs by black dashed-line boxes.

The crystal faces that are not selected as photosensing faces are set to be perfectly non-reflective, corresponding to an ideal black-painted crystal surface in real detectors. Using the same Monte Carlo method, a designated number of the same type of scintillation-light distributions are also generated for a 3D grid of emission points that spans the whole volume of the monolithic crystal starting and ending 0.5 mm away from all faces. The number of scintillation-light distributions per grid point, n_p, is a parameter that can be chosen by the user. The fluence images from these distributions are stored as training data to be used for the statistical estimation of the simulation's POIs (later pretended to be unknown) thus mimicking the calibration procedure performed for real monolithic crystals but in an idealised 3D manner.

POIs and PET image (Fig. 2.2D-F)

The 3D gamma-ray POIs, whose ground-truth is only known in simulations, are then estimated from the scintillation fluence images by means of an algorithm of choice, for this study two different algorithms have been developed and compared. One based on the k-nearest neighbours (kNN) approach and the other one based on a convolutional neural network, both of them described in detail below. The algorithm uses the previously generated test and training data (step C in the workflow) in order to accomplish the task of determining the POIs corresponding to the coincidence-sorted events obtained from the processing of the Gate simulation results (step B in the workflow). In this part of the workflow, and if required by the POI estimation algorithm, the fluence images can be reduced into specific features of interest. The estimated POIs from the coincidence-sorted events (test data) are finally discretised into 1 mm^3 virtual crystals and used to create list-mode PET data suitable for tomographic image reconstruction, which is implemented with the CASToR toolkit [46].

2.2.2 k-nearest neighbours algorithm

The first POI estimation algorithm developed is based on the k-nearest neighbours (kNN) supervised statistical machine learning method. In this method usually applied as a classifier, a specific number, k, of training data instances are selected which are closest (in terms of a chosen metric) to a given test data instance. These training data instances are thus termed the k-nearest neighbours to the test data instance being analysed. From these neighbours a single training data instance label can be predicted for that test data instance

with the use of a statistical operation such as a mode or mean computation, thus classifying it into a specific class [47].

For the kNN-based algorithm developed in this study the six fluence images obtained for all of the scintillating events are preprocessed by reducing them into specific features in order to prepare them for the subsequent distance metric applied and to save computational time. Training data is obtained by reducing the fluence images from the 3D emission-point grid while test data by reducing the fluence images from the coincidence-sorted Gate simulation results instead. Each image is reduced to three features: its 2D centre of gravity (*CoG*), the index of the pixel with the highest number of photons recorded (i_{max}) and the sum of all pixels (sum_{fi}); which are stored as a 4-element list representation of the image to be used by the kNN algorithm. The centre of gravity of a fluence image is calculated with the following equation:

$$x = \frac{\sum_{i=1}^{n} m_i \times x_i}{\sum_{i=1}^{n} m_i}, \quad y = \frac{\sum_{i=1}^{n} m_i \times y_i}{\sum_{i=1}^{n} m_i} \tag{2.1}$$

where *i* represents the the image pixel index, *n* is the total number of pixels, m_i is the value of pixel *i* (i.e. the number of photons recorded by that pixel), and x_i, y_i are the indices of pixel *i* along the x and y dimensions of the image respectively. The denominator in Eq. 2.1 is the image feature previously referred to as sum_{fi} that represents the sum of all pixels in a fluence image and thus the total number of photons detected by the corresponding photosensor. The values obtained with Eq. 2.1 for a two-dimensional CoG are therefore not limited to the discrete pixel indices but lie within a continuous space that spans the whole area of the photosensor.

A simplified schematic representation of a fluence image corresponding to one crystal face is illustrated in Fig. 2.3, where the coordinates of the *CoG* feature are indicated by a brown dot and the pixel with the highest value (the i_{max} feature) by a white x. Fig. 2.3 shows how these two features of a fluence image do not necessarily correspond to the same pixel. This is an effect of the fact that when a scintillation event occurs away from the centre of a photosensor the scintillation light cone projected onto that photosensor results only in a partial 2D Gaussian-like distribution. This distribution corresponds to the sector of the circular cross-section of the scintillation cone directly impinging on the photosensor. Hence, the

closer a scintillation origin in the crystal is to a photosensor, the better Gaussian-defined the scintillation light distribution from the light cone cross-section being detected. While the closer the scintillation origin in the crystal is to the centre of the photosensor, the closer the *CoG* of the corresponding fluence image to the i_{max} pixel.

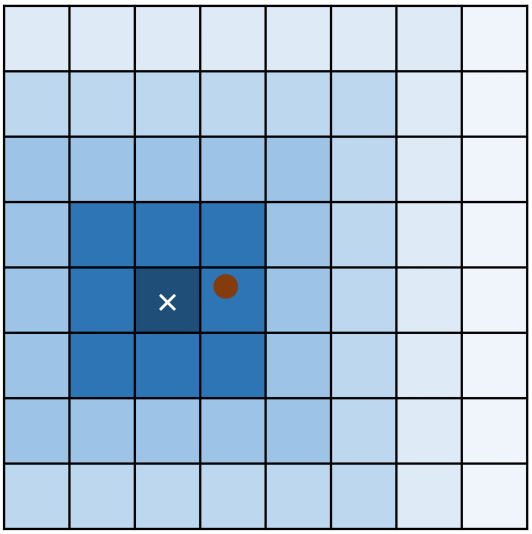

Figure 2.3: Simplified example of a fluence image. The intensity of a pixel colour represents the relative number of photons detected by the corresponding photosensor channel. A white x indicates the pixel with the highest value (i_{max} feature) and a brown dot indicates the coordinates of the image's centre of gravity (*CoG* feature).

After all the fluence images in the data have been reduced to the features of interest described above, the kNN algorithm designed for this study begins by reducing the feature and target spaces of the training data to be used for each individual test event. Given the sum_{fi} from a face image of a test event, lower and upper bounds are established indicating the segment of the crystal along the orthogonal dimension to the plane of that face where the gamma-ray interaction could have occurred. This is done by finding the minimum and maximum locations along that dimension where training events with the same i_{max} as the test event had a similar sum_{fi} to it. An example of the type of data used for this process is given in Fig. 2.4 and hereby described. Considering a test-event fluence image from a photosensor XY_1 lying on the xy-plane, the pixel with the highest number of photons recorded ($i_{max,\,XY1}$) is noted. Out of all the training events, those whose i_{max} for that same photosensor XY_1 are equal to $i_{max,\,XY1}$ (from the test image) are selected. These selected events are further grouped by the discrete z-coordinate (i.e. along the axis orthogonal to photosensor XY_1 and in this case with a 1-mm spacing) of their POI in the crystal.

For each z-coordinate group, the minimum and maximum sum_{fi} values within the group are extracted, and here plotted in Fig. 2.4 for exemplary data. These values represent the range of possible sum_{fi} that photosensor XY_1 can have for a test event with i_{max} equal to $i_{max,\,XY1}$ at each of the 1-mm discretised training event positions along the z-axis, i.e. at 1-mm steps towards or away from it.

In the case represented by Fig. 2.4 the photosensor XY_1 was placed at the xy-plane lying on the crystal face where z = 25 mm. The range of sum_{fi} values at each training grid z-coordinate thus increases with increasing magnitude of the coordinate as the event gets closer to the photosensor. The initial minimum value and the final maximum value are manually set to 0 and to infinity respectively in order to include events that occur closer to the crystal surfaces than the closest training grid POI. To conclude the example, in this case, if the test event being considered were to have a sum_{fi} value of 4000 (that is 4000 photons detected by photosensor XY_1), as can be observed in Fig 2.4 the possible z-coordinates at which its POI could have occurred are given by the range $16.5 \leq z \leq 17.5$. Only the training data corresponding to that subsector of the crystal would therefore be used for the rest of the algorithm's operation on that test event, in other words, the target space of the training data in which to look for the closest event to the test event has been reduced.

The target space reduction with which the kNN algorithm begins can be applied along any combination of the three crystal dimensions. If, for example, two faces are being considered as photosensing, the target space reduction occurs in two dimensions, as illustrated in Fig. 2.5a in 2D and in Fig. 2.5b in 3D. The green and blue dotted lines represent the space reduction obtained from the image produced by the sensor of the corresponding colour while the red volume represents the resulting crystal segment where the POI (red sphere) could be situated.

The algorithm then computes the euclidean distance only between the *CoG* features of the test event and the *CoG* features of the reduced training data, subsequently minimising it to select the k nearest neighbours. The *CoG* features belonging to a specific event are appended into a single vector $\vec{C}$ whose dimension is twice the number of crystal faces being considered as photosensing, given that for each photosensor a *CoG* with an x and a y coordinate is obtained. The euclidean distance between any two $\vec{C}s$ is thus computed

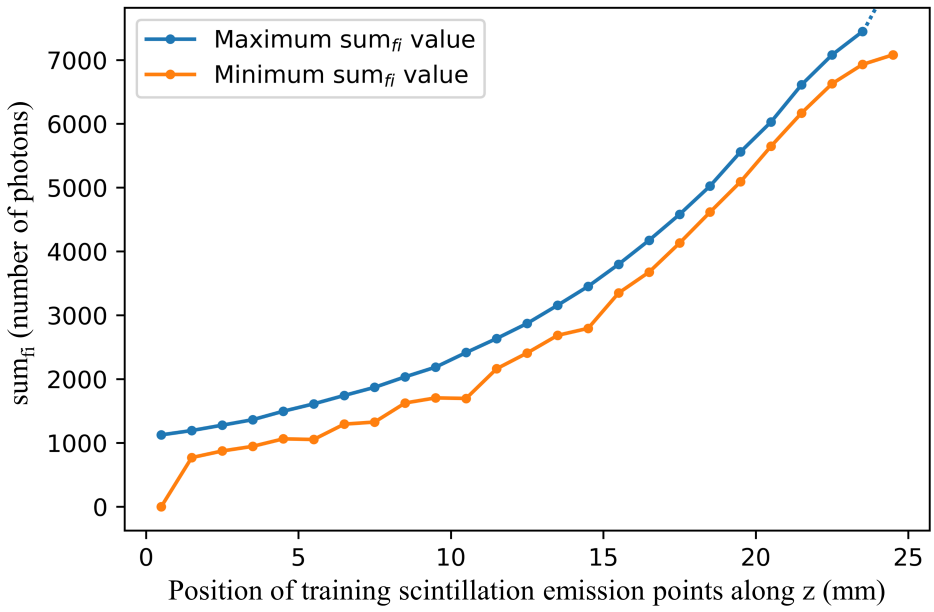

Figure 2.4: Minimum and maximum sum_{fi} values for all training fluence images corresponding to a specific i_{max} grouped by the z-coordinate of their POI and obtained from a photosensor at the xy-plane lying on the crystal face where z = 25 mm.

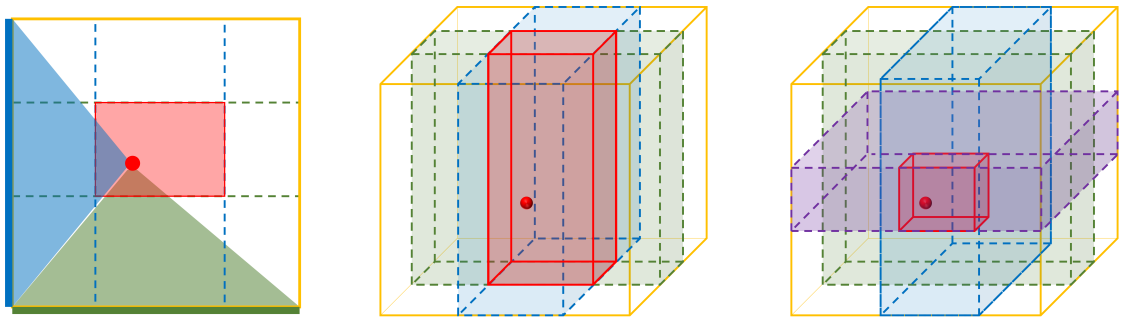

Figure 2.5: Diagrams illustrating the target space reduction obtained along two dimensions (*a* and *b*) and three dimensions (*c*) as part of the developed POI estimation algorithm. Two perpendicular photosensors are shown in *a* as thick blue and green lines. The triangles of corresponding colours represent a 2D slice of the scintillation light cone detected by each one of them and originating from a gamma-ray interaction whose position is indicated by the red dot. The parallel dashed lines of the same colours represent the target space reduction obtained in the dimension orthogonal to the photosensor using the training information recorded by that photosensor. Highlighted in red is the final reduced target space subsequently used by the estimation algorithm. Diagram *b* shows the same scenario as *a* but as a 3D visualisation. Diagram *c* illustrates the further target space reduction obtained if a photosensor is coupled to at least one of the crystal faces along each of the three crystal planes. Not to scale.

with the following equation:

$$\begin{aligned} ED(\vec{C_a}, \vec{C_b}) &= \|\vec{C_a} - \vec{C_b}\| \\ &= \sqrt{(C_{a,1} - C_{b,1})^2 + (C_{a,2} - C_{b,2})^2 + \cdots + (C_{a,n} - C_{b,n})^2} \end{aligned} \tag{2.2}$$

where n is the dimension of the $\vec{C}s$, equal to twice the number of photosensors being considered.

To conclude, the 3D average of the labels (scintillation emission points from the 3D training grid) corresponding to the k nearest neighbours is computed as the estimated POI for the test event. In this last step the discrete values of the POI labels corresponding to the k nearest neighbours are surmounted as their average lies in a continuous space between them and is not anymore limited to the training POI grid. Given the characteristics of this developed algorithm it will be hereon referred to as the *ReSCoGs A-kNN* algorithm, which stands for Reduced-Space Centres of Gravity Averaged-kNN.

Initial trial of the framework with the *ReSCoGs A-kNN* algorithm

In order to test the functionality of this simulation and reconstruction framework (employing the *ReSCoGs A-kNN* POI estimation algorithm) and to evaluate the preliminary feasibility of a preclinical monolithic-detector PET subsystem, an initial trial PET system with 15 cubic monolithic LYSO crystals was considered. Each crystal cube had a length of 30 mm and had two perpendicular photosensors attached to it, one at the back crystal face (as conventional in PET detectors) and one at a lateral face. Both photosensors had dimensions of 20 x 20 pixels. The 15 crystals were arranged in a single ring yielding an inner diameter of 15.5 cm close to those of commercial preclinical systems [48]. The phantom being imaged consisted of two point sources with a 1 mm diameter and 1 mm surface-to-surface distance that was configured in Gate to directly emit back-to-back 511 keV gamma-rays. A 4 ns coincidence window was used for the data coincidence sorting and a total of five million coincidence events were recorded, while the number of scintillating photons emitted per scintillation event was set to 18,000 corresponding to the approximate number emitted by LYSO crystals at such gamma-ray energies. The n_p and k values used in the *ReSCoGs A-kNN* algorithm were 30 and 60 respectively.

Furthermore, the ground-truth POIs obtained from the coincidence-sorting stage were also blurred according to Gaussian distributions with FWHMs of 0.25 mm, 0.5 mm, 0.75 mm

and 1.5 mm yielding four new data sets. These data sets were then reconstructed along with the estimated POIs and the ground-truth POIs in order to obtain six different images. In this way, the effect of the accuracy of the POI estimation step could be observed on the final reconstructed image. Image reconstruction was carried out using the standard Maximum Likelihood Expectation Maximisation (MLEM) algorithm and Joseph projector in the CASToR toolkit. The algorithm was applied with 10 iterations of 16 subsets to obtain images with 0.2 mm^3 voxels for a FOV of 80 x 80 x 20 mm.

In-depth investigation of the *CoG* feature

In favour of further investigating and understanding the performance of the *ReSCoGs A-kNN* algorithm specific scintillation simulations were carried out for a 25 mm^3 LYSO crystal compatible with standard 1-inch SiPM photosensors. With a focus on exploring the characteristics of the representation of fluence images by their *CoG* feature the following examinations were performed:

- A single scintillation event was simulated at the (12.5, 18.5, 22.5) mm position inside the crystal (with the origin at a vertex) and fluence images were recorded by a photosensor lying on the xy-plane at z = 25 mm. Six different fluence images of that same event were produced as photosensors with the following six different channel numbers were studied: 3 x 3, 4 x 4, 6 x 6, 8 x 8, 12 x 12 and 24 x 24 channels. The same procedure was repeated for four more scintillation events along the diagonal crossing the crystal from its centre to the vertex at (25, 25, 25) mm as indicated in Fig. 2.6. The *CoGs* were computed for their corresponding fluence images and compared between them for the case where the photosensors had a 100 % PDE thus detecting all photons and for the case were they had a 50 % PDE thus detecting only half of the photons.

- 50 scintillation events were simulated at each point of a 1 mm^3-spaced grid spanning the whole crystal volume and starting and ending 0.5 mm away from its faces. The *CoGs* of the corresponding fluence images recorded by a photosensor of 8 x 8 channels lying on the xy-plane at z = 25 mm were then computed. The *CoGs* were then visualised either all together or in specific subgroups in order to study their distinctiveness as a function of the distance between the photosensor and the scintillation event and to study the effect of the target space reduction.

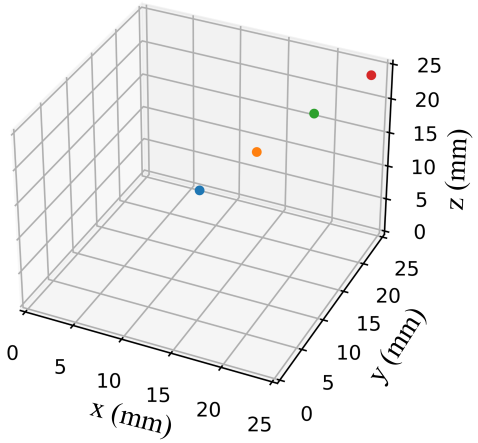

Figure 2.6: Four scintillation event points, along the diagonal between the centre of the crystal and the vertex at (25, 25, 25) mm, used to investigate the *CoG* feature.

2.2.3 Convolutional neural network algorithm

The second POI estimation algorithm developed in this work is based on a convolutional neural network (CNN)[1]. In such type of machine learning, or deep learning, one or several fully connected convolutional layers are used in order to extract, or learn complex features representative of the data that would otherwise not be identified by a person using their limited human image processing capabilities. This is accomplished by their ability to handle large amounts of data and to use a convolution process with a kernel or filter that allows them to create and probe many different representations of the data in order to identify certain characteristics or patterns [50]. CNNs have found particular applicability for image processing tasks given that the kernel used can have two or three dimensions and effectively identify features in image arrays of corresponding dimensions [49]. In the previously described kNN-based algorithm the features into which each fluence image is reduced are deliberately chosen to be sum_{fi}, i_{max} and *CoG* based on the knowledge of the physics behind the processes that result in the formation of the image. In the CNN algorithm, by contrast, the large number of image features identified and employed are unknown to the user, hence the referral to this type of method as a black box is commonly heard.

The CNN-based algorithm designed for this work is composed of the neural network ar-

[1]For a detailed description of CNNs and deep learning in general the reader is invited to consult [49].

chitecture illustrated in Fig. 2.7. Said network carries out a regression process that starts with a given test 2D fluence image as input and predicts one of three coordinates of the gamma-ray POI that produced it, as an output label that lies in the continuous 3D space of the crystal. The network is thus trained three times, once per crystal dimension, and applied those same three times to each test event in order to get a prediction for the three coordinates of the POI. As represented in Fig. 2.7, the architecture of the network consists of 4 layers. The first two are convolutional layers where a ReLU activation function is applied and a 3x3 kernel is used. The third layer simply applies a flattening operation that produces a 1D list of features that is then processed by the fourth fully-connected layer, also activated with ReLU. Since the prediction process is seen as a regression, a mean squared error loss function is used as the criterion to train the network, which is done with the same training data used for the *ReSCoGs A-kNN* algorithm. The implementation of this neural network was carried out using the PyTorch platform with its stochastic gradient descent optimiser [51] and always using an n_p value of 50 training events per point in the 3D POI training grid.

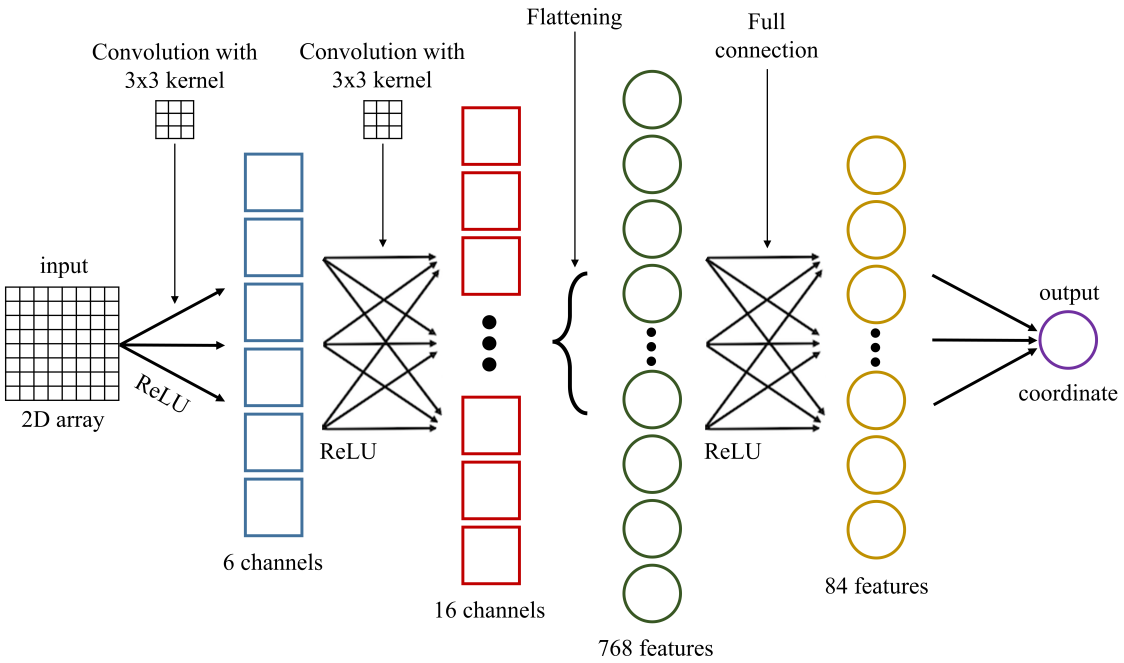

Figure 2.7: Architecture of the CNN designed for this work. The size of the data at each layer is labelled under it and the process applied to it is labelled above. The use of a ReLU activation function is also indicated where appropriate.

2.2.4 Optical imaging subsystem

In order to study the optical imaging subsystem included in the multimodal concept being proposed a previously developed tool for the investigation of plenoptic-detector imaging systems was used. This Monte Carlo tool takes as an input the description of the phantom and the plenoptic detectors to be simulated. The phantom can be provided as a 3D mesh representation including a bioluminescent or fluorescent source distribution from which the propagation of the corresponding emitted photons is simulated. Whereas the position, size and arrangement of the imaging system are provided as a series of geometrical parameters that fully describe it. The output of the simulation process is a series of projections of the light field exiting the phantom onto the detectors surrounding it, namely one projection per plenotpic detector being considered. These projections can also be simulated as being noise-inflicted by specifying a value for the plenoptic detectors' signal-to-noise ratio of detection. From the projections, resembling those from light field cameras, the corresponding computational imaging problem can then be undertaken in order to obtain a single tomographically reconstructed image [52, 10]. This tool is part of a scientific simulation, rendering and reconstruction framework for in vivo preclinical plenoptic imaging investigation, named Lipros[2].

2.3 System design conception

2.3.1 PET subsystem optimisation

Starting with a crystal size of 25 x 25 x 25 mm and two standard 1-inch SiPMs (with 8 x 8 channels and a PDE of 50 %) coupled to two of its perpendicular faces, three characteristics of the monolithic-detector PET module were investigated and optimised as described below. As a prerequisite, the n_p and k parameters of the *ReSCoGs A-kNN* algorithm were optimised for such configuration by minimising the estimation error obtained from one million randomly distributed scintillation events within the crystal. Each event was defined to produce 18,000 scintillation photons corresponding to the number produced by 511 keV gamma-rays interacting in LYSO crystals. The estimation error of an event is defined as the difference between the estimated POI and its ground-truth value. The minimisation, specifically of the mean absolute error (MAE) of estimation, was carried out with the error distributions obtained when using the algorithm for the same data as a function of n_p and k with values in the ranges of [5, 45] and [5, 165] in steps of 10 and 20 respectively. With the optimised n_p and k values, and using one million events, the follow-

[2]To be published by members of the research group in which this work was carried out.

ing three monolithic-detector characteristics were then in turn optimised:

Crystal depth: The effect of the crystal depth on the gamma-ray POI estimation capability of the *ReSCoGs A-kNN* algorithm was studied by computing the MAE of estimation for seven different crystal depths in the range of [6.25, 25] mm and increasing in steps of 3.125 mm. For each depth the algorithm used the training data corresponding to the section of the 3D grid of training POIs that fitted within the dimensions of the crystal. This process was then repeated for the standard case where only a single crystal face had a photosensor coupled to it instead of two perpendicular faces having photosensors coupled to them.

Number of crystal faces with a photosensor coupled to them: The effect of the number of crystal faces with photosensors coupled to them on the gamma-ray POI estimation capability of the *ReSCoGs A-kNN* algorithm was investigated for the full-sized cubic crystal with 25 x 25 x 25 mm dimensions. The MAE of estimation was computed for nine different combinations of number of faces being considered as photosensing. The number of combinations exceeds six because different arrangements of the same number of photosensors are possible. Two photosensors, for example can be coupled to opposite faces, in a so called dual ended readout configuration, or to perpendicular faces as in the starting case described above.

Number of channels per photosensor: The effect of the number of channels per photosensor on the gamma-ray POI estimation capability of the *ReSCoGs A-kNN* algorithm was examined for the full-sized cubic crystal with 25 x 25 x 25 mm dimensions with two photosensors coupled to two of its perpendicular faces. The MAE of estimation was computed for six different 2D number of channels per photosensor: 3 x 3, 4 x 4, 6 x 6, 8 x 8, 12 x 12 and 24 x 24 channels.

2.3.2 Optical imaging subsystem precursor

In order to verify the preliminary functionality of a preclinical optical imaging subsystem composed of plenoptic detectors an initial test system of ten squared plenoptic detectors was considered. The detectors were arranged in a ring pattern yielding a diameter of 80 mm and had the geometrical parameters summarised in Table 2.1. Each plenoptic detector consisted of a light sensor set to resemble commercially available CMOS flat sensors with a sensitive area of 25 x 25 mm and pixelated into 11 x 11 μm photodiodes thus yielding a total of 2250 x 2250 sensor pixels. A microlens array having the same overall dimensions was added to the top of the flat sensor. Each microlens had a refractive index equal to 1.8292 and a diameter of 500 μm, thus yielding a total of 50 x 50 microlenses.

Each one of them therefore corresponded to a locally separated array of 45 x 45 sensor pixels. A distance of 1 mm corresponding to the effective focal length of the microlens array was kept between the flat sensor and the microlens array, such distance is usually implemented through the use of septa. The imaging acquisition of a two point source phantom with this system was simulated using the tool and process described in section 2.2.4, in which the obtained projections were reconstructed with the computational tomographic method described in [10]. In this process each of the plenoptic detectors in the system were assigned a detection signal-to-noise ratio of 5 dB. The phantom had the same geometry as the PET phantom described in section 2.2.2, namely it consisted of two spheres with a diameter of 1 mm and a centre-to-centre distance of 2 mm between them. In this case, however, each sphere emitted 10^5 photons, resembling a red firefly luciferase (RFL) bioluminescent probe, whose scatter-free propagation onto the plenoptic detectors was simulated.

Table 2.1: Values for the geometrical parameters describing the plenotpic detectors of the optical imaging system used as a precursory design of the PET-OT optical imaging subsystem.

Parameter	Value
Sensitive area (mm)	25 x 25
Number of sensor pixels	2250 x 2250
Sensor pixel size (μm)	11 x 11
Number of microlenses	50 x 50
Microlens diameter (μm)	500
Refractive index of microlenses	1.8292
Effective focal length (mm)	1

2.4 Proposed system

Following the optimisation of the modules for the monolithic-detector PET subsystem and the verification of the optical imaging subsystem a final PET-OT conceptual prototype was conceived in order to be evaluated and subsequently proposed. The detector concept being ultimately proposed is already foreshadowed and presented here in order to be able to continue with the description of the processes by which it was evaluated. The system is based on 10 bi-modal detector modules that contain two distinct, yet integrated, components. The modules are arranged to form a ring shape with an inner diameter of 83 mm. A schematic of the system with an enlargement of a comounted detector module is shown in Fig. 2.8, where both components can be seen. The two components of a module corresponding to each of the two subsystems are described in detail below.

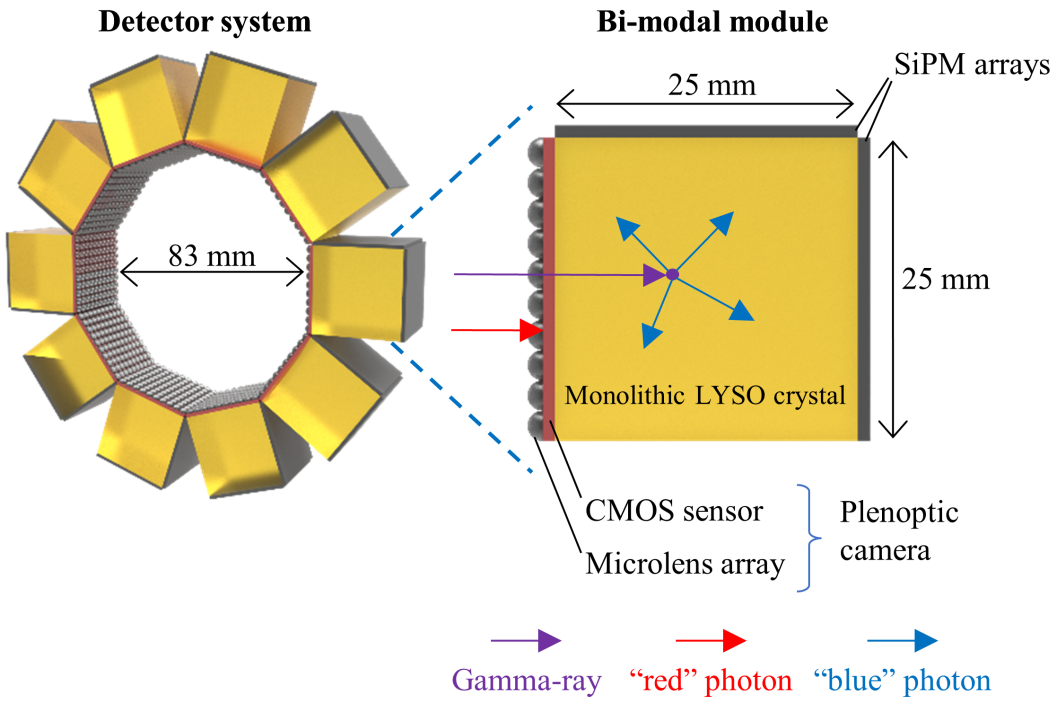

Figure 2.8: Schematic of the proposed PET-OT system and enlargement of a bi-modal detector module. The elements that constitute both the PET and the optical imaging components within a module are indicated. For illustrative purposes, the plenoptic camera and SiPMs are represented with augmented dimensions and not to scale

2.4.1 PET subsystem

The PET subsystem component, is dedicated to the detection of gamma-rays emitted by radiotracers and consists of a 25 x 25 x 25 mm monolithic LYSO crystal and two 25 x 25 mm SiPM-array photosensors with 8 x 8 channels each, one coupled to its back face and the other one to a perpendicular side face. By itself, this subsystem comprises a fully operational monolithic-detector preclinical PET scanner. As mentioned in section 2.1, due to the *sieving* strategy used to robustly separate the optical imaging and PET signals, optical-probe photons coming form the subject being imaged cannot reach this component. In contrast, the gamma-rays emitted form radiotracers simply travel through the optical imaging component and can interact in the monolithic crystal producing scintillation light as shown in Fig 2.8.

Comparison between estimation algorithms

Being a monolithic-detector preclinical PET scanner, this PET subsystem requires a computational algorithm to determine the POIs of the gamma-rays produced by radiotracers and interacting in the crystals. The two POI estimation algorithms described in sections 2.2.2 and 2.2.3 were therefore compared for said task, namely the *ReSCoGs A-kNN* and CNN-based algorithms. Considering the geometry and configuration of a single monolithic-crystal PET detector, the estimation error obtained by both algorithms from one million randomly distributed scintillation events within the crystal was investigated. Each event was defined to produce 18,000 scintillation photons corresponding to the number produced by 511 keV gamma-rays interacting in LYSO crystals, while the PDE of the photosensors was set to be 50 %. The global estimation error distribution within the whole crystal volume as well as the dependence of the error on the ground-truth position of the POIs were examined. In the case of the *ReSCoGs A-kNN* algorithm the previously optimised n_p and k parameters were employed with a 1 mm^3-spaced training POI grid representing a realistic irradiation step as used in normal 2D calibration of monolithic crystals with an added step along the depth dimension [53]. For the CNN-based algorithm six training epochs were used with all other parameters kept as indicated in section 2.2.3.

2.4.2 Optical imaging subsystem

The optical imaging subsystem component is dedicated to the detection of optical photons emitted from fluorescent or bioluminescent probes and consists of a plenoptic detector mounted on the front face of the monolithic crystal with its sensing face pointing towards the centre of the scanner. The design of this component was established as an enhancement of the preliminary design presented in section 2.3.2 considering the experience with and knowledge of plenoptic-detector PET inserts built in the past by the research group within which this work was carried out [54]. Its geometrical parameters are summarised in Table 2.2 and described below. Similarly, it consists of a light sensor set to resemble commercially available CMOS flat sensors with a sensitive area of 22.5 x 22.5 mm and pixelated into 11 x 11 µm photodiodes thus yielding a total of 2048 x 2048 sensor pixels. The coupled microlens array with the same overall dimensions has a refractive index equal to 1.8292 and a lens diameter of 450 µm, thus yielding a total of 45 x 45 microlenses. Each one of them therefore corresponding to a locally separated array of 45 x 45 sensor pixels. A distance of 1 mm corresponding to the effective focal length of the microlens array is kept between the flat sensor and the microlens array.

Table 2.2: Values for the geometrical parameters describing the plenotpic detector that constitutes the optical imaging component of the system's bi-modal modules.

Parameter	Value
Sensitive area (mm)	22.5 x 22.5
Number of sensor pixels	2048 x 2048
Sensor pixel size (μm)	11 x 11
Number of microlenses	45 x 45
Microlens diameter (μm)	450
Refractive index of microlenses	1.8292
Effective focal length (mm)	1

2.5 Performance evaluation

Using the simulation and reconstruction frameworks presented in section 2.2, both subsystems of the proposed system concept were independently evaluated by investigating their performance through the different criteria described in the following sections. The preclinical monolithic-detector PET subsystem and the optical imaging subsystem described in section 2.4 were therefore simulated and studied with the final goal of assessing the feasibility of the proposed system concept.

2.5.1 PET spatial resolution and sensitivity

Spatial resolution

The spatial resolution of the monolithic-detector PET subsystem was studied with a procedure based on the protocol established in the NEMA Standards Publication NU 4-2008 [55]. A ^{22}Na spherical point source with a diameter of 0.25 mm and an activity of 4 μCi was simulated at the axial centre of the FOV at six different radial positions from 0 to 25 mm away from the transversal (in this case also global) centre of the FOV in steps of 5 mm. The point source was embedded at the centre of an acrylic cube with 10 mm dimensions. For each position, 5 million events were recorded using the monolithic-PET simulation and reconstruction framework presented in section 2.2.1 employing the *ReSCoGs A-kNN* algorithm with the parameters optimised as described in section 2.3.1. A 450 keV lower energy acceptance bound and a 4 ns coincidence window were used for the coincidence-sorting step while the image reconstruction was carried out using the standard MLEM algorithm and Joseph projector in the CASToR toolkit. The algorithm was

applied with 10 iterations of 16 subsets to obtain images with 0.2 mm^3 voxels for a FOV of 60 x 60 x 12 mm. For each image, a system's response function along each of the three FOV dimensions (radial, tangential and axial) was obtained by summing all one-dimensional profiles along the dimension and its corresponding FWHM was calculated by linearly interpolating the two pixels adjacent to half its maximum value.

This spatial resolution evaluation procedure was carried out for two different cases. One where the optical imaging subsystem was present and one where it was absent. In the former, a 25 x 25 x 0.9 mm silicon layer was coupled to the entrance face of the monolithic crystals in the simulation. In this way the plenoptic cameras that compose the optical imaging subsystem were considered in a simplified way and their effect on the spatial resolution of the PET subsystem was examined. The dimensions chosen for the silicon layer representing the plenoptic cameras was chosen in accordance with those of commercially available CMOS sensors [56]. The procedure was repeated three times for each of the two cases considered.

Geometrical efficiency

Given that this work is based on the use of simulations, the sensitivity of the monolithic-detector PET subsystem was investigated by using an accordingly adapted version of the NEMA standard protocol that measures the ideal axial geometrical efficiency of the scanner. The same Na22 point source described above was placed at the transversal centre of the scanner and moved in steps of 0.5 mm along its axial dimension. At each step an acquisition yielding 5 million events was performed using the same coincidence-sorting parameters stated above. The geometrical efficiency was then measured as a function of the axial position of the point source. In this case, the geometrical efficiency GE is defined as the number of true coincidences detected (Trues) divided by the activity $A_{\gamma-pairs}$ given by the number of simulated positron-electron annihilations that resulted in a pair of backscattered gamma-rays, as summarised in the following equation:

$$GE\,(\%) = \frac{Trues}{A_{\gamma-pairs}} \tag{2.3}$$

2.5.2 Derenzo phantom imaging

In order to assess the overall imaging capability of the PET subsystem the PET scanning acquisition of a Derenzo hot rod phantom was simulated and reconstructed using the

framework presented in section 2.2.1. The phantom consists of an acrylic cylinder with a diameter of 35 mm and a depth of 10 mm that includes six triangular arrays of embedded hot rods defined to emit back-to-back 511 keV gamma-rays. An image of the transverse slice at the axial centre of the phantom is displayed in Fig 2.9. The rods in one array all have the same diameter and are spaced centre-to-centre by twice that length. The rod-diameters of the arrays vary from 0.75 mm to 2 mm in steps of 0.25 mm, as indicated in the figure. A a 4 ns coincidence window were used for the coincidence-sorting stage until 20 million coincidence events had been acquired. After the coincidence-sorting stage both algorithms presented in section 2.2 were used to estimate the gamma-rays POIs in order to compare the effect of their performance on the final reconstructed image. For the *ReSCoGs A-kNN* algorithm the parameters optimised as described in section 2.3.1 were used with a 1 mm^3-spaced training POI grid. For the CNN-based algorithm six training epochs were used with all other parameters kept as indicated in section 2.2.3. The image reconstruction was carried out using the standard MLEM algorithm and Joseph projector in the CASToR toolkit. The algorithm was applied with 10 iterations of 16 subsets to obtain images with 0.2 mm^3 voxels for a FOV of 40 x 40 x 12 mm.

Moreover, in order to further study the effect of the POI estimation resolution on the quality of the final reconstructed image, the reconstruction procedure was repeated six more times for different theoretical POI estimation resolutions (i.e. the FWHM of the estimation error distribution). Each time the ground-truth POIs from the coincidence-sorting stage were shifted in all three dimensions by a distance randomly selected from a Gaussian distribution with a specific FWHM defined to reproduce one of the six different theoretical POI estimation resolutions from 0 mm^3 to 1.25 mm^3 in steps of 0.25 mm^3. These blurred POIs were then directly turned to list-mode PET data and reconstructed into images as described above since the blurring procedure represented the POI estimation stage and thus substituted it.

2.5.3 Mouse phantom imaging

As a final inspection of the proposed system concept the bi-modal imaging acquisition of a mouse phantom was simulated with the PET and optical tomography simulation frameworks described in section 2.2. In this way the overall imaging capability of the proposed PET-OT system was assessed in a realistic preclinical context. The mouse phantom imaged was a version of the publicly available Digimouse Atlas shown in Fig. 2.10 that has been created from coregistered cryosection and CT images of a 28g normal male mouse

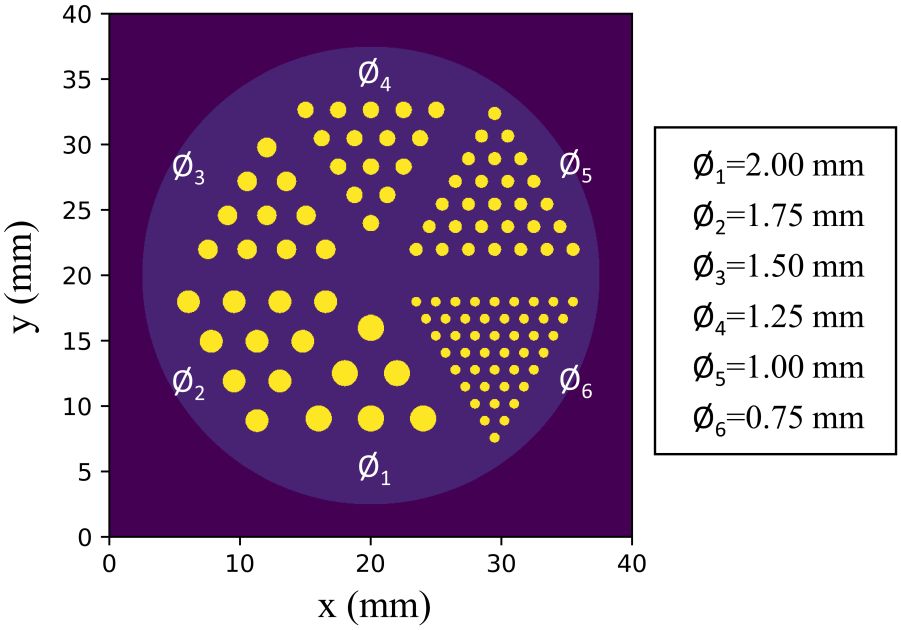

Figure 2.9: Image of the transverse slice at the axial centre of the Derenzo phantom with a diameter of 35 mm and a depth of 10 mm. The diameters of the rods in each of the triangular arrays (equal to the surface-to-surface distance between them) are labelled next to them.

[57].

PET imaging

For the PET imaging acquisition a voxelized representation of the phantom with voxel size equal to 0.2 mm^3 and overall dimensions of 164 x 98 x 444 voxels was used. The phantom included an implanted tumour on the left flank of the mouse, specifically above the left hindlimb, having an amorphous quasi-spherical shape with an approximate radius of 2.5 mm. The different organs and tissues, as well as the tumour, were specified by their voxel values and assigned a corresponding density from the standard list of material densities in the Gate simulation tool. The density of the tumour was assigned according to the values presented for melanoma tumours in [58]. The radioactivity distribution in the phantom was defined by assigning specific activity values to the voxels corresponding to each organ and tissue as well as to the tumour. The relative magnitude of these activity values was determined according to data obtained from the literature for 18F-Galacto-RGD radiotracer uptake PET studies in the presence of an M21 melanoma tumour [59]. Both the density and the activity used for the mouse phantom components are presented below in Table 2.3.

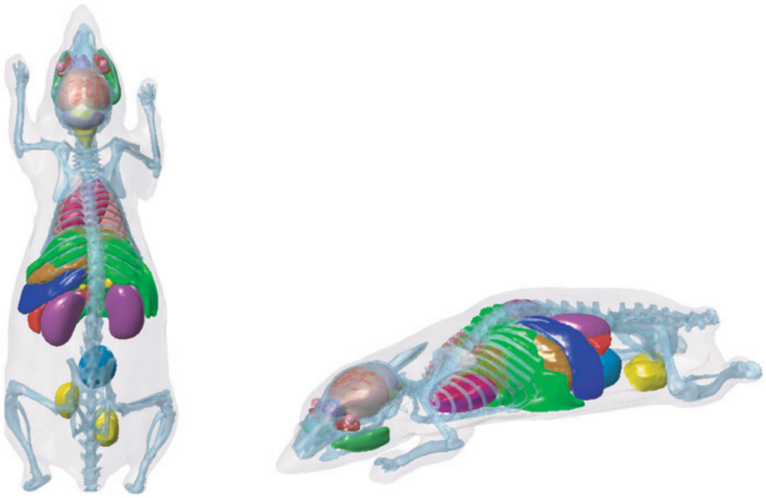

Figure 2.10: 3D rendering of the Digimouse Atlas. Image reprinted from [57].

The PET acquisition simulation was divided in four stages where the scanner was translated each time by 20 mm along its axial direction in order to cover the entire length of the mouse. A 450 keV lower energy acceptance bound and a 4 ns coincidence window were used for the coincidence-sorting of the data obtained until 20 million events had been acquired in total. After the coincidence-sorting step the *ReSCoGs A-kNN* algorithm presented in section 2.2.2 was used to estimate the gamma-rays POIs with its parameters optimised as described in section 2.3.1 and a 1 mm^3-spaced training POI grid. The image reconstruction was carried out using the standard MLEM algorithm and Joseph projector in the CASToR toolkit. The algorithm was applied with 10 iterations of 16 subsets to obtain images with 0.2 mm^3 voxels for an individual-stage FOV of 40 x 40 x 20 mm thus yielding a total FOV of 40 x 40 x 80 mm.

Optical tomography

For the optical imaging acquisition simulation the mesh representation of the same phantom and tumour combination described above and displayed in Fig. 2.11 was used. In this case the tumour was defined to emit 10^5 photons, resembling the accumulation of a red firefly luciferase (RFL) bioluminescent probe. The propagation of these photons onto the plenoptic detectors of the system was simulated using the tool and process described in section 2.2.4. A detection signal-to-noise ratio of 5 dB was assigned to all plenoptic detectors of the system.

Table 2.3: Density and activity values for the organs, tissues and tumour included in the PET mouse phantom.

Organ/tissue	Density (g/cm^3)	Activity (kBq)
Heart	1.05	31
Lung	0.26	83
Liver	1.06	223
Spleen	1.06	96
Pancreas	1.04	23
Stomach	1.03	96
Bladder & testis	1.04	63
Intestines	1.03	220
Brain	1.04	131
Kidney	1.05	243
Muscle	1.05	17
Bone	1.42	36
M21 tumour	1.04	153

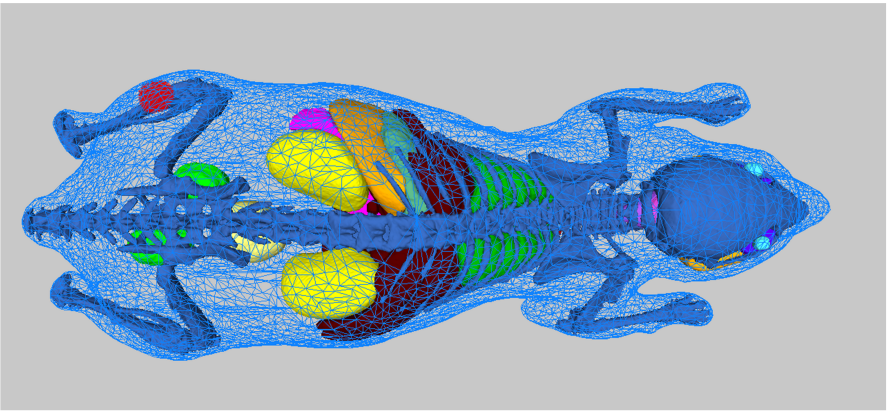

Figure 2.11: Mesh representation of the tumour-bearing mouse phantom based on the Digimouse Atlas used for the simulation of the optical imaging subsystem.

3

System development and performance results

The journey of a thousand miles starts from beneath your feet

- Lao Tzu

The results of the procedures developed and utilised in this work are presented and discussed in this chapter. The outcomes of the functionality analysis of the monolithic-detector PET simulation and reconstruction framework are examined together with those of the characterisation of the proposed POI estimation algorithms. Moreover, the results of the optimisation methodology used to design the proposed system as well as those of its performance evaluation are displayed and assessed.

3.1 PET simulation and reconstruction framework

3.1.1 Initial trial with the *ReSCoGs A-kNN* algorithm

The outcomes of the initial trial with which the functionality of the monolithic-detector PET simulation and reconstruction framework was evaluated are summarised as a flowchart in Fig. 3.1. As described in section 2.2.2, in this case the POI estimation method used was the *ReSCoGs A-kNN* algorithm, represented in box *c* of Fig. 3.1. A rendering of the system considered is presented in the left side of box *a*, where the 15 monolithic crystals are depicted in red and the two perpendicularly-attached photosensors per crystal in blue. An enlargement of the two-point-source phantom imaged is included and examples of the trajectories of several gamma-rays being emitted by it are represented as thin green lines within the simulation's rendering. In the right side of box *b* a single scintillation event occurring at a gamma-ray POI within one of the crystals of the system is schematically illustrated with blue lines representing the trajectories of the scintillating optical photons that are isotropically emitted. In the left side of box *b* an example of a group of scintillation fluence images obtained at five of the six faces in one of the monolithic crystals is presented for a single scintillation event. Blue frames indicate the two fluence images that correspond to the two crystal faces to which photosensors are coupled in the detector's design and that are therefore actually used by the *ReSCoGs A-kNN* algorithm. Each fluence image contains 20 x 20 pixels corresponding to the number of channels in the photosensors being simulated.

A 2D distribution of the POI estimation error for the five million coincidence events recorded is presented in the right side of box *c* for the x and y dimensions of the crystal. The FWHM of this error distribution along all three dimensions was 1.02 mm, 1.22 mm and 0.82 mm in the x,y and z axes respectively. The discrepancy between the errors along different dimensions is mainly a result of the combination of two factors. The first one being the large size of the monolithic crystals being "photo-sensed" at perpendicular faces, which means that there is an asymmetric response to scintillations being produced within the crystal. Namely, the *CoG* feature, being four elements long in this case, contains information about the POI along the z dimension twice since both photosensors lie on crystal planes along this dimension (the xz and yz planes) and only once for the other two dimensions. The second factor is that at the stage of this trial the target space reduction component of the algorithm had not yet been fully optimised. The finalisation of this component was hypothesised to reduce the asymmetric noise produced by training data belonging to

sectors of the crystal far from that at which the gamma-ray actually interacted. Particularly those locations far from the photosensing faces where the recorded scintillation distribution resembles a Gaussian distribution the least. The final reconstructed image obtained after the application of the framework is shown in the left side of box *d*. As observed, both point sources can be clearly visually identified. The functionality of the framework and successful operation of the *ReSCoGs A-kNN* algorithm were thus confirmed while providing insight into possible improvements for both the framework and the design of the multimodal system concept.

The effect of the accuracy of the POI estimation step of the framework on the final reconstructed image is shown in Fig. 3.2. The reconstructed image obtained from the initial trial and already shown in Fig. 2.2d is presented once more in Fig. 3.2e and compared to five other reconstruction cases. The image obtained when reconstructing list-mode PET data from the direct discretisation of the exact POIs of the gamma-rays generated in the initial simulation stage (Fig. 2.2a) is presented in Fig. 3.2a. For the generating of such image, the scintillation simulation step and the POI estimation step of the framework (Fig. 2.2b,c) are therefore skipped. This image thus represents the ideal imaging capabilities of such a PET system design if the exact POI of all the gamma-rays emitted from the subject could be accurately and precisely determined. The reaming four images show the deterioration of the imaging quality of the system as the resolution of the POI estimation method decreases. In each one of them the ground-truth POIs were blurred according to factors randomly selected form a Gaussian distribution whose FWHM is reported above each image. The FWHM therefore represents that of the thus created estimation error distribution and so it mimics the resolution of a hypothetical imperfect POI estimation algorithm.

Beyond a certain resolution, for example 1.5 mm^3 shown in Fig. 3.2f, visually discerning the geometry of the phantom becomes not possible anymore. The importance of the resolution of the POI estimation algorithm employed in a monolithic-detector PET system is in this way demonstrated by Fig. 3.2. This is equivalent to the well known dependence of the spatial resolution of conventional segmented-detector PET systems on the size of their individual crystal elements, which in that case straight-forwardly determines the 2D POI determination resolution [60]. Furthermore, this figure shows a useful application of the developed simulation and reconstruction framework in that it can allow the user to set the required POI determination resolution for a system based on the desired quality of the final reconstructed image.

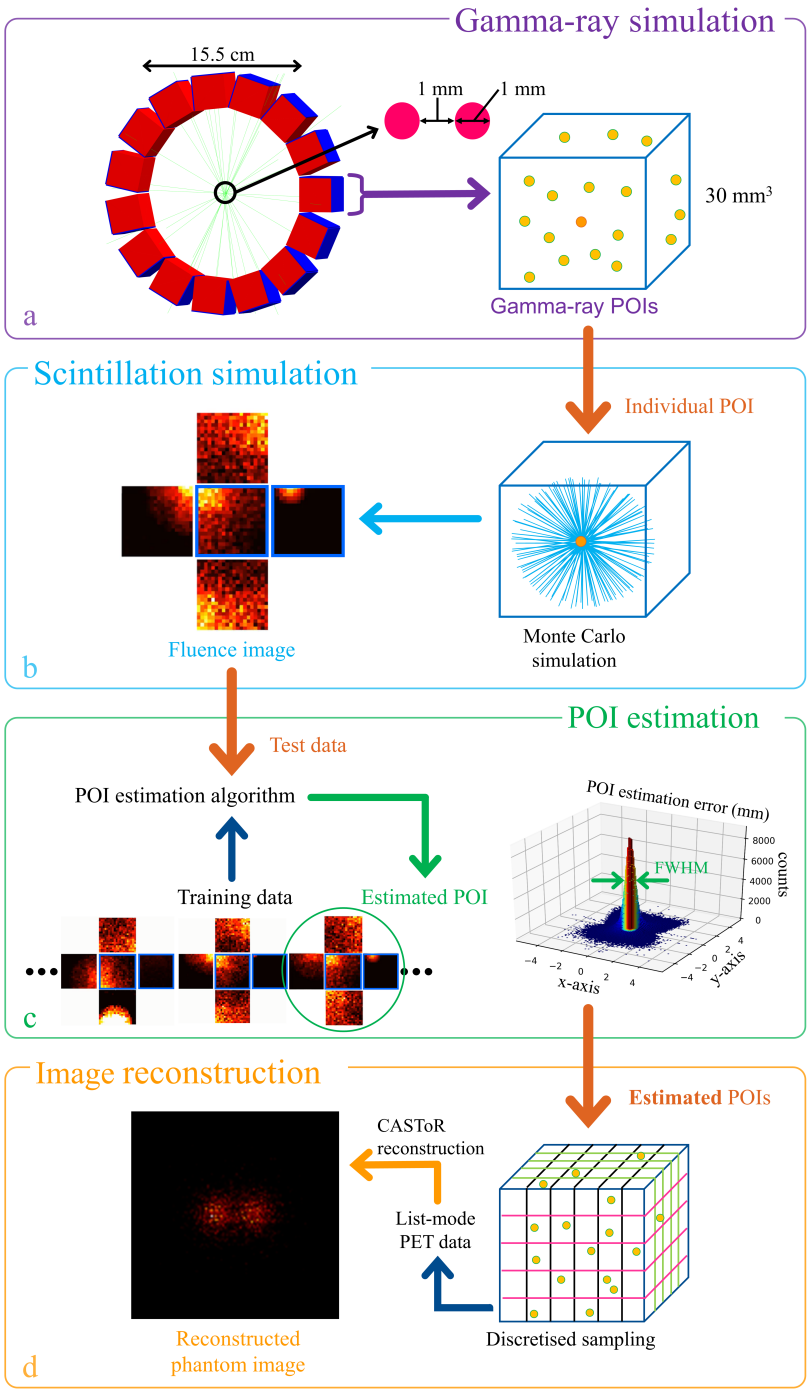

Figure 3.1: Outcome of the initial trial for the PET simulation and reconstruction framework employing the *ReSCoGs A-kNN* algorithm. a) Gamma-ray simulation: rendering of the scanner-phantom configuration simulation and schematic of the POIs in a single monolithic crystal, b) scintillation simulation: schematic of a scintillation light emission and example of five fluence images obtained for such a single event, c) POI estimation: simplified representation of the POI estimation process and graph displaying the 2D distribution of estimation errors obtained in the trial simulation, d) image reconstruction: schematic of the 3D discretisation of the estimated POIs into list-mode PET data and final reconstructed image of the the imaged phantom.

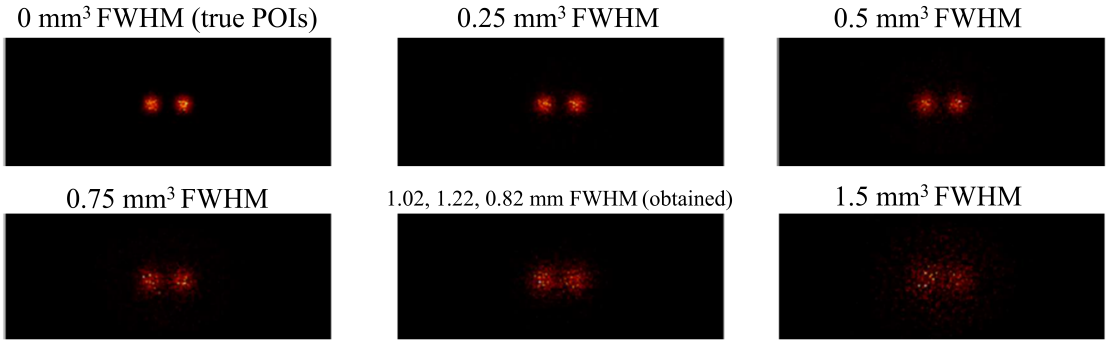

Figure 3.2: Effect of the POI estimation resolution on the final reconstructed image. Transverse slice at the axial centre of the reconstructed images from the same ground-truth POIs being blurred by Gaussian distributions of different FWHM, mimicking the estimation error of a POI estimation algorithm. The FWHM of the distribution used is indicated above each image. Image *e* is the actual reconstructed image obtained from the trial simulation and is thus labelled with the corresponding FWHM of the estimation error distribution obtained.

3.1.2 In-depth investigation of the *CoG* feature

The *CoG* feature is a pillar of the *ReSCoGs A-kNN* algorithm and as such was characterised with a thorough procedure, described in section 2.2.2, whose outcome is summarised below. To show the type of fluence images obtained from the simulation of monolithic detectors, six different fluence images of the same scintillation event are presented in Fig. 3.3. These images were recorded by photosensors with different number of channels, indicated above them. In all cases the photosensor is located at the crystal face lying on the xy-plane at z = 25 mm and the scintillation event at the (12.5, 18.5, 22.5) mm crystal coordinates. As expected, the pixel intensity, i.e. the number of photons recorded by the corresponding channel, increases as the number of channels decreases.

It is evident from Fig. 3.3 that with coarser images the task of identifying the centre of gravity (indicated as a red dot) precisely using simply the human eye becomes harder. Given the high number of photons being distributed among the photosensor channels, the use of Eq. 2.1 yields, however, a comparable *CoG* in all cases. It can also be observed how the *CoG* is not constrained to lie on the centre of any pixel but rather lies on a space that approaches a continuum as the number of channels and photons being considered increases and thus the combinations of possible collective wights of the pixel coordinates multiply. This effect stresses the importance of the light yield property of the scintillator to be used in a monolithic PET detector, and its desirable maximisation motivates the use of LYSO crystals for the system concept being proposed.

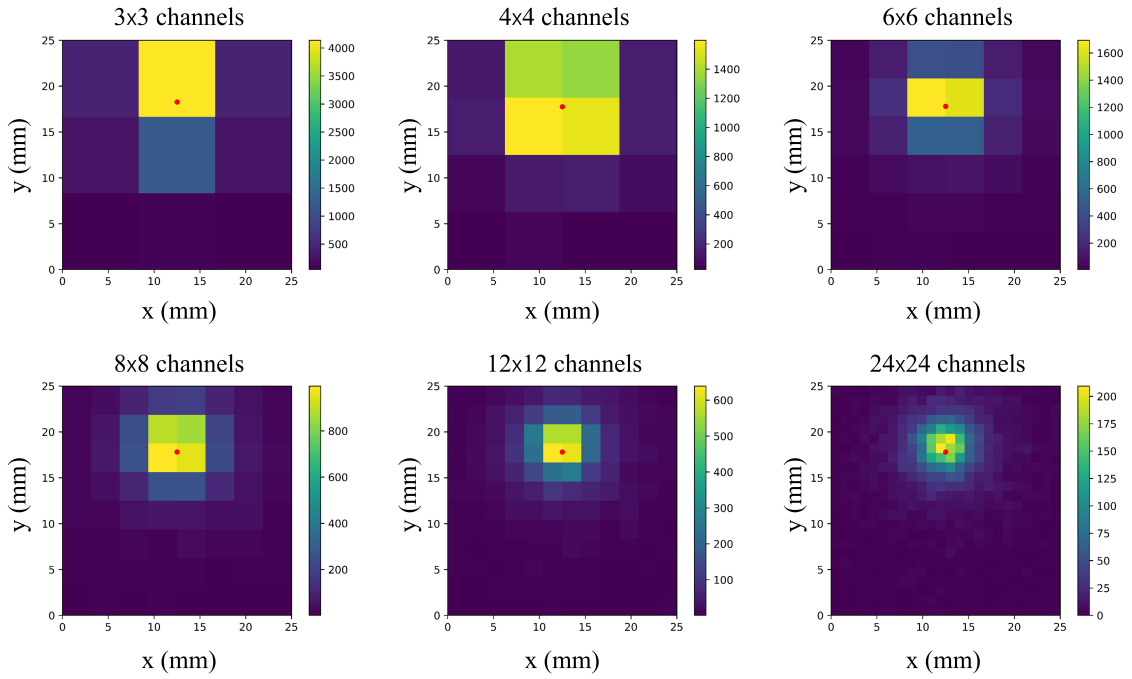

Figure 3.3: Six different fluence images obtained at the same crystal face lying on the xy-plane at z = 25 mm for the same scintillation event located at the (12.5, 18.5, 22.5) mm crystal coordinates. Each image was produced by a photosensor at that face with a different number of channels and thus has a different number of corresponding pixels, indicated above it. In all cases, for every photosensor channel one fluence image pixel of the same size is displayed. The colour of the pixels represents the number of photons detected by the corresponding photosensor channel. A red dot indicates the computed *CoG* for each image, using Eq. 2.1.

The effect that the number of channels in the photosensor being considered has on the position of the *CoG* is shown in the two figures below for the four points lying along the diagonal of the crystal indicated in Fig. 2.6. Fig. 3.4 shows the value of the x coordinate of the *CoG* for a scintillation emitted at each of the four POIs and being recorded by each of the six different photosensors. Both the realistic case where the photosensors have a 50% PDE and the ideal case where they have a 100% PDE are displayed. Fig. 3.5 shows instead the y value of the same *CoGs*. As can be observed, the difference between the two cases with different PDE values is imperceptible for both coordinates, being in all cases below 1%. This suggests that such difference in the number of photons detected is not enough to change the shape of their projected distribution, which is an effect only expected to be significant as the number of photons decreases beyond the point where their distribution can be still statistically defined.

Given that the x and y coordinates of the points were always equal to each other, so were the x and y coordinates of their respective *CoGs* almost equal to each other too, again always with a difference below 1%. This is an expected effect of the squared symmetry of the crystal and photosensor spaces that also emphasises the independence of the two coordinates. Furthermore, with the exception of the point closest to the photosensor and to the orthogonal edges of the crystal, the *CoGs* of all points show a fluctuation below 1% when being computed from the different number of photosensor channels. An effect that is also visible in Fig. 3.3. The reason for the shift in the *CoG* of the event occurring at $(24, 24, 24)$ is that for the channel numbers below 24×24 this point lies outside the perimeter delineated by the centres of the outer pixels and thus outside the quasi-continuum where a *CoG* can exist.

The previous figures suggest that the *CoG* feature is a well-defined 2D representation of individual scintillation distributions created in the whole crystal volume and one that is independent of the sensor configuration. When estimating the unknown POI corresponding to a given test fluence image having as its only representation its *CoG*, a classifying estimation algorithm must consider the *CoGs* of the fluence images from all training scintillation events. It becomes therefore necessary to verify that the 2D *CoGs* preserve their uniqueness for all points in the training grid and especially as the distance along the third dimension, i.e. orthogonal to the photosensor, increases. A 2D scatter-plot image of all the *CoGs* obtained from all the POIs in the training grid whose fluence images were recorded by a photosensor lying on the xy-plane is shown in Fig. 3.6. In this case the photosensor had 8 x 8 channels. In the plot a faint grid of *CoGs* can be seen along with a high intensity central area of squared symmetry. The former is obtained from the *CoGs* corresponding

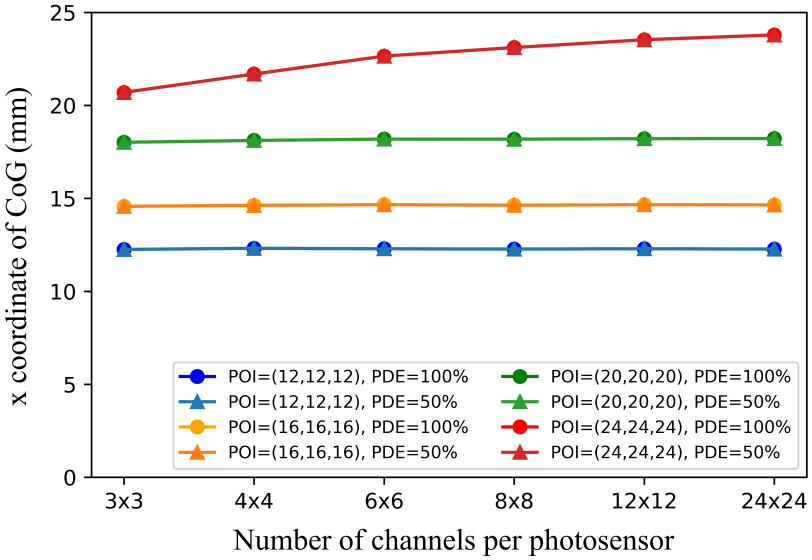

Figure 3.4: Effect of the number of photosensor channels on the x-coordinate of the *CoG* feature. The x-coordinate of the *CoG* obtained from four scintillation events with different POIs recorded by six different configurations of photosensor number of channels are shown in different colours. The two cases for the photosensors having a 50% and a 100% PDE are labelled and distinguished by their marker shape.

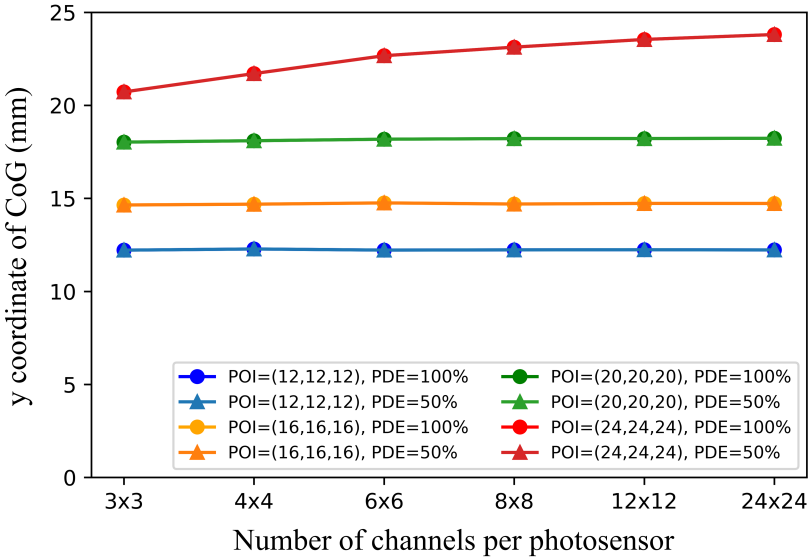

Figure 3.5: Effect of the number of photosensor channels on the y-coordinate of the *CoG* feature. The y-coordinate of the *CoG* obtained from four scintillation events with different POIs recorded by six different configurations of photosensor number of channels are shown in different colours. The two cases for the photosensors having a 50% and a 100% PDE are labelled and distinguished by their marker shape.

to scintillating POIs close enough to the photosensor for their fluence image to preserve a sharp Gaussian-like shape that peaks along the line between the x,y coordinates of the POI and the centre of the photosensor in that same plane, as shown in Fig. 3.3. The latter is obtained from the *CoGs* corresponding to scintillating POIs with increasing distances away from the photosensor. By contrast, their fluence images present a shallower peak that when averaged with the rest of the channels for the calculation of the *CoG* has a smaller weight and thus yields a result closer to the centre. As an example of this effect one can consider the extreme case of a fluence image of pure noise where all pixels have similar random values and would thus yield a 2D *CoG* essentially at the centre of the image.

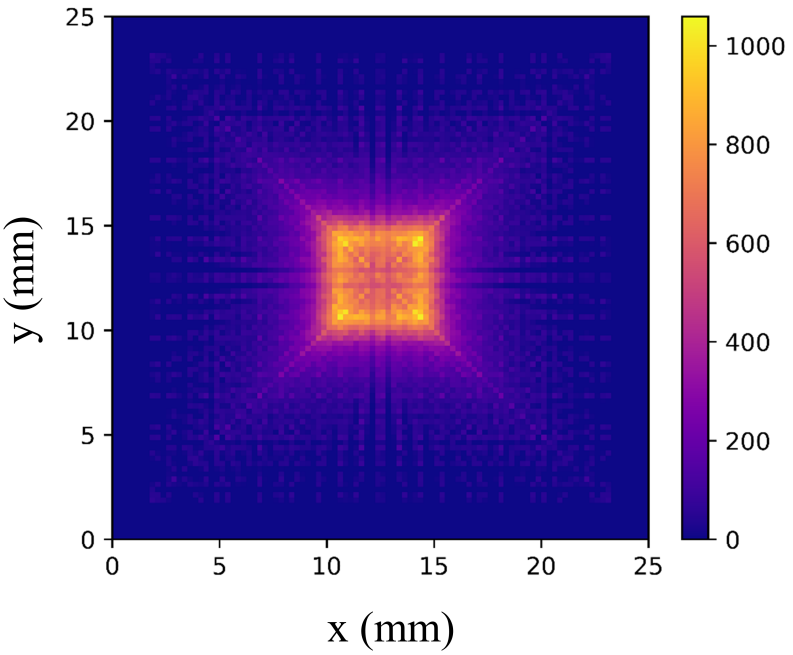

Figure 3.6: 2D scatter-plot of all the *CoGs* obtained from POIs in the training grid whose fluence images were recorded by a photosensor lying on the xy-plane.

This centre-attraction effect is further shown in Fig. 3.7, where a 2D scatter-plot of the *CoGs* obtained for all training events whose x,y coordinates were 22.5 mm and 22.5 mm respectively are shown. Each colour group represents the *CoGs* corresponding to training POIs with a particular z-coordinate labelled as the distance between the POI and the crystal face to which the photosensor is coupled. The closer to the photosensor the less spread out are the 50 *CoGs* corresponding to a training POI. Whereas with increasing distance away from the photosensor the CoGs show a higher variance suggesting a weaker definition of the fluence image by its *CoG*. Moreover for distances beyond half the depth of the crystal

the CoGs of different POIs start overlapping, which is what causes the high-intensity central region in Fig. 3.6. Such position-dependent level of uniqueness in the representation of fluence images by their *CoGs* poses a challenge for the POI estimation task, particularly if being the only one considered.

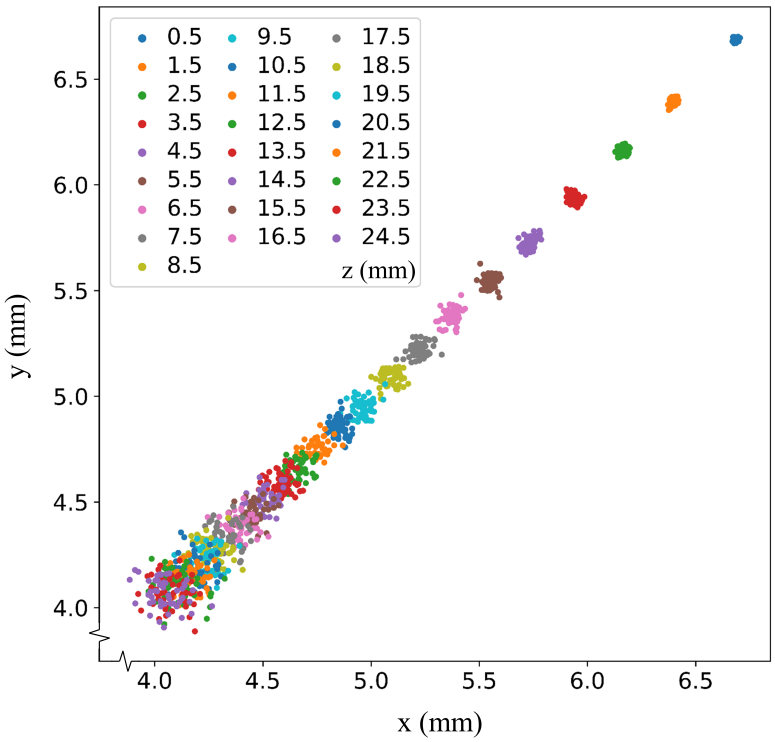

Figure 3.7: 2D scatter-plot of the *CoGs* obtained for all training events whose x,y coordinates were 22.5 mm and 22.5 mm. The 2D *CoGs* are expressed with respect to the centre of the crystal at (12.5, 12.5) mm on its xy-plane. Each colour group represents the *CoGs* corresponding to training POIs with a particular z-coordinate labelled as the distance between the POI and the crystal face to which the photosensor is coupled.

To address this challenge coming form the loss of uniqueness of *CoGs*, the consideration of two more representative characteristics, or features, of a fluence image were introduced into the POI estimation mechanism employed by the *ReSCoGs A-kNN* algorithm. These two features are the index of the channel with the highest number of photons recorded, i_{max}, and the sum over all channels, sum_{fi}. Their inclusion constitutes, as described in section 2.2.2, the target space reduction element of the *ReSCoGs A-kNN* algorithm, a concept illustrated in Fig. 2.5. As an example of the combined behaviour of these two features, Fig. 3.8 shows the sum_{fi} values for all the training events whose fluence image on an xy-plane photosensor at z = 25 mm had an i_{max} value of 18. This means that the channel that

recorded the highest number of photons had said index, which in this case corresponds to the channel centred at the (2.6, 2.6) xy-coordinates. The sum_{fi} values are grouped by the z-coordinate of their POI and assigned the same colour within that group. Two labelled solid lines join the minimum and maximum sum_{fi} values per group respectively. As expected, the closer to the photosensor an event occurs the larger the sum_{fi} value of its fluence image. Given that in this case the position of the i_{max} channel is close to the corner of the crystal, the variance of the sum_{fi} groups increases too when their POIs approach the photosensor. This occurs as multiple POIs on the same xy-plane yield the same i_{max} value and the magnitude of difference in the amount of photons produced by them and reaching the photosensor increases as they get closer to it. In this case, indeed, the sum_{fi} values for the groups with z-coordinates 21.5 mm, 22.5 mm and 23.5 mm are fragmented into discrete subgroups formed by the specific POIs, on the xy-planes lying at those z-coordinates, at which their corresponding scintillations were produced.

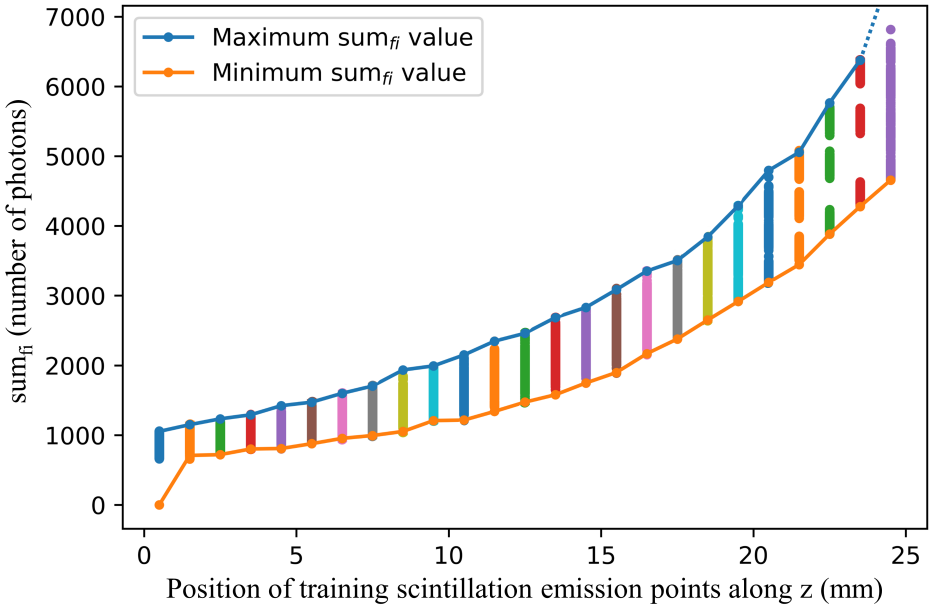

Figure 3.8: sum_{fi} values for all the training events whose fluence image on an xy-plane photosensor at z = 25 mm had an i_{max} value of 18, i.e. the channel centred at (2.6, 2.6). The values are grouped by the z-coordinate of their POI and assigned the same colour within that group. The minimum and maximum sum_{fi} values per group are joined by two solid lines labelled respectively.

The full effect of the target space reduction process on the *CoGs* to be considered by the *ReSCoGs A-kNN* algorithm is shown in Fig. 3.9. The top row displays three subsets of all the *CoGs*, shown in Fig. 3.6, obtained after a target space reduction along the z-dimension is applied, i.e. only the *CoGs* corresponding to training events with POIs within

the range indicated above each image are displayed. In this case the photosensor was placed at the crystal face lying on the xy-plane at z = 0 mm. The obtained reduction in the available *CoG* feature space is evident even though, however, the presence of intra-reduced-space *CoGs* obtained from the symmetry along the xy-plane can still be seen to act as noise for the algorithm, particularly further away form the photosensor. The bottom row shows the additional feature space reduction obtained when, for the same subsets, only the *CoGs* corresponding to training events that yielded a particular i_{max} are considered, in this case $i_{max} = 18$. The uniqueness pf the representation of the fluence images produced by scintillation events on the whole 3D space of the crystal is thus significantly improved, implying a more accurate POI estimation. In this way the *ReSCoGs A-kNN* algorithm is improved by being able to apply a euclidean distance minimisation on only that subset of *CoGs* without the confusion of the rest of the training data.

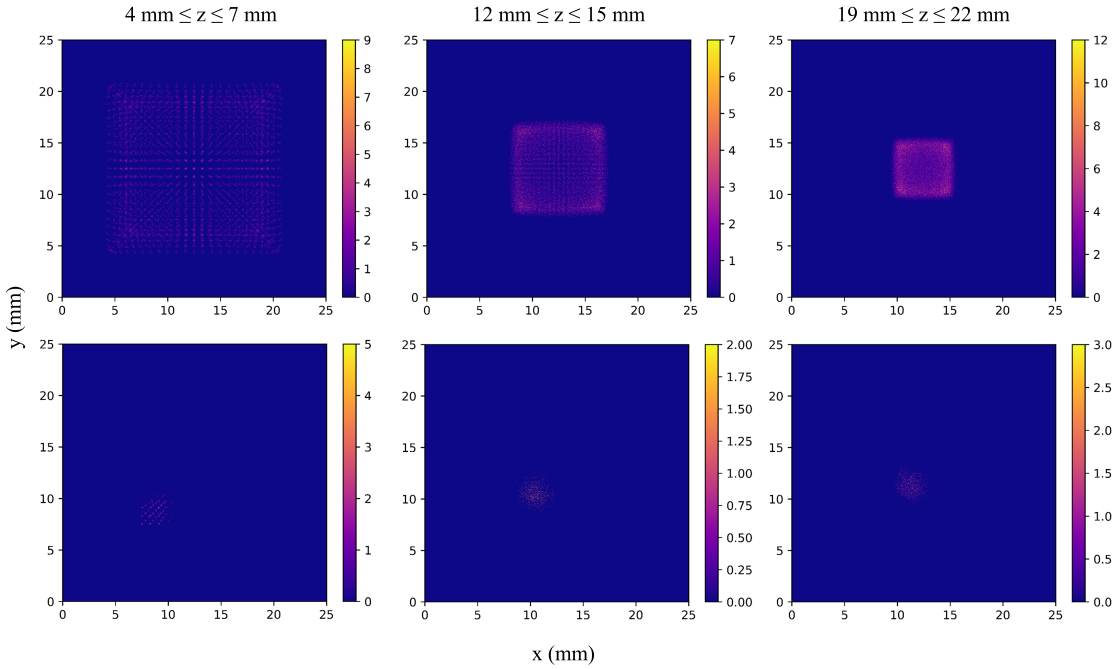

Figure 3.9: Effect of the target space reduction on the subset of CoGs being considered by the *ReSCoGs A-kNN* algorithm. Top row: the *CoGs* corresponding to training events with POIs within the crystal sector indicated above each image are displayed. Bottom row: only the CoGs within the same subsets as above that had an $i_{max} = 18$ are displayed.

3.2 System design conception

3.2.1 PET subsystem optimisation

The optimisation of the *ReSCoGs A-kNN* algorithm for a crystal size of 25 x 25 x 25 mm and two standard 1-inch SiPMs (with 8 x 8 channels and a PDE of 50%) coupled to two of its perpendicular faces yielded k and n_p values of 85 and 35 respectively. These parameters represent the number of nearest neighbours and the number of samples per point of the training grid respectively. The parametric minimisation results can be seen in Fig. 3.10, which shows the global mean absolute error (MAE) of the POI estimation as a function of these two parameters for all 1 million randomly distributed events simulated in the crystal. The POI estimation error is a 3D vector defined as the difference between the estimated 3D POI and the simulation ground truth 3D POI.

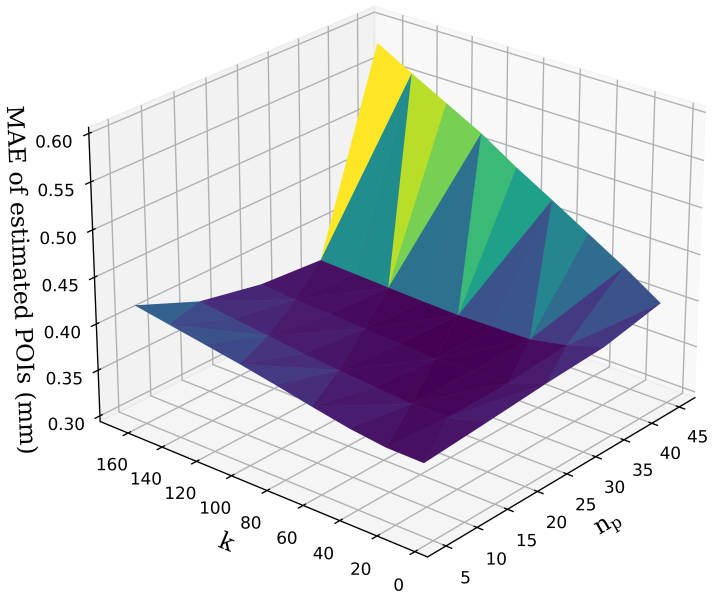

Figure 3.10: Minimisation of the global MAE of estimation as a function of k and n_p for 1 million randomly distributed POIs in a 25 x 25 x 25 mm crystal with two 8 x 8-channel photosensors perpendicularly coupled to two of its faces.

The performance of the optimised *ReSCoGs A-kNN* algorithm with respect to the crystal depth is shown in Fig. 3.11. Two different photosensor configurations, indicated in the figure, are considered: a conventional single back-face photosensor configuration and a dual perpendicular photosensor readout configuration. In the former case the POI estimation performance decreases with increasing crystal depth. This is a consequence of the residual *CoG*-overlapping effect that remains even after the application of the target space

reduction technique in the absence of an additional photosensor that can provide more information and increase the space reduction. Once a second photosensor is added, however, that information is present and thus the performance improves while the decrease in performance pattern ceases to be present as it is instead sustained up until a crystal depth of 25 mm. This result supports the use of said perpendicular dual-readout configuration very seldom considered in literature, which in conjunction with the *ReSCoGs A-kNN* algorithm allows for a crystal depth of 25 mm that far exceeds that of the few commercially available preclinical PET systems reaching a maximum value of 12 mm [61].

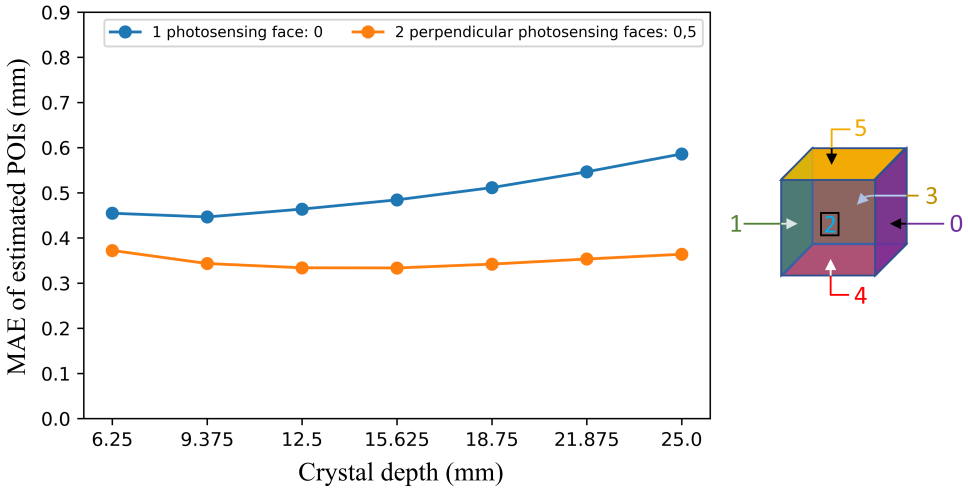

Figure 3.11: MAE of POI estimation as a function of crystal depth for 1 million randomly distributed POIs in a crystal with a cross-sectional size of 25 x 25 mm. Two different photosensor configurations are presented and labelled according to the diagram on the right.

The performance of the *ReSCoGs A-kNN* algorithm with respect to the number and arrangement of crystal faces being coupled to 8 x 8-channel photosensors is shown in Fig. 3.12 for a crystal of size 25 x 25 x 25 mm. Taking into account the cubic symmetry of the crystal, the MAE of the POI estimation for all relevant photosensor arrangements of one to six photosensors is included. For such crystal size, and as seen also in Fig. 3.11, a significant improvement to the use of a single photosensor is observed when adding a second perpendicular photosensor. If the second sensor is instead added to the face opposite to the first one, thus obtaining a conventional dual-ended readout configuration, the improvement is yet greater, at the cost, however, of the addition of components to the crystal side facing the bore of the scanner. This greater improvement is a result of the distance of any given POI to a sensor being always equal to or smaller than half the crystal length, which does not occur in the perpendicular dual-ended readout configuration. In this way a subset of *CoG* features with minor overlapping between them is always obtained, as shown in Fig. 3.9,

and the minimisation of the euclidean distance between them and the test *CoG* is thus more accurate. The importance of this distance for the operation of the algorithm relies, once more, on the fact that the closer a POI is to a sensor, the sharper its distribution is, or the better Gaussian-defined its fluence image is, and thus the more its *CoG* feature approaches a unique representation of it.

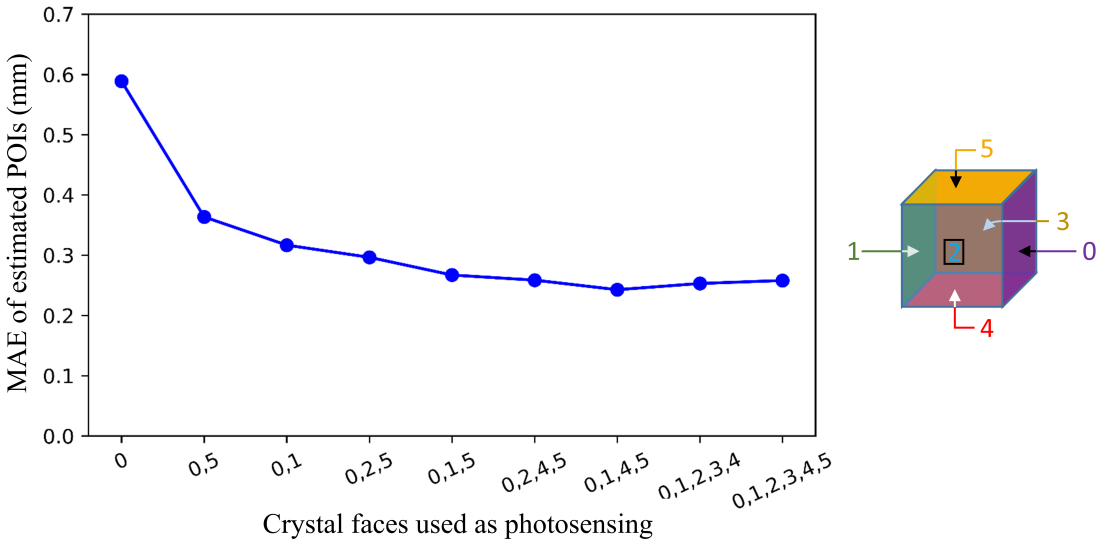

Figure 3.12: MAE of POI estimation as a function of the number and arrangement of crystal faces being coupled to 8 x 8-channel photosensors for 1 million randomly distributed POIs in a crystal with a size of 25 x 25 25 mm. The different photosensor configurations are labelled according to the diagram on the right.

For this specific crystal size and optimisation of the *ReSCoGs A-kNN* algorithm, it can also be observed that using more than four sensors does not further improve the performance as the limits imposed by the algorithm's parameters and the POI training grid spacing are reached. Furthermore, the difference from a MAE of 0.36 mm with a perpendicular dual-ended configuration to the plateau averaged at a MAE of 0.27 mm is considerably smaller than that to the single photosensor case. This raises the question of whether the practical, computational and economical investment of adding a third and fourth photosensor to a PET design is worth such an improvement in POI estimation performance. A decision to be made, perhaps, based on the effect of such estimation resolution on the final reconstructed image, as shown in Fig. 3.2, practical considerations and the aspirations for the scanner design.

The performance of the *ReSCoGs A-kNN* algorithm as a function of the number of photosensor channels in each of two perpendicular photosensing faces is shown Fig. 3.13. The results are displayed in two different scales in order to better observe the pattern presented. It can be seen that, given the number of photons produced per scintillation and the PDE of the sensors, further discretising the fluence image by having more photosensor channels, continuously yet marginally improves the algorithm's performance. Furthermore, it is evident that in these conditions a minimum MAE is reached after which further discretisation results in a higher error. Since this relationship is independent of the choice of k and n_p parameters, the pattern points out the intrinsic robustness of the algorithm given the high ratio of photons to image pixels in a fluence image.

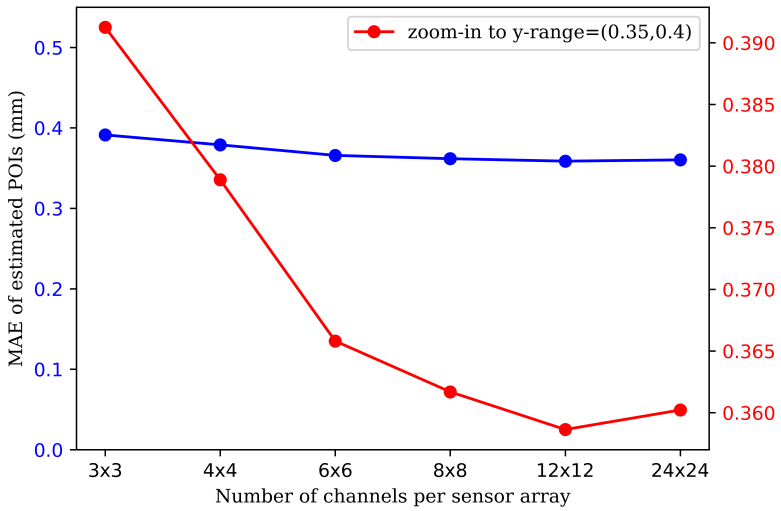

Figure 3.13: MAE of POI estimation as a function of the number of photosensor channels in each of two perpendicular photosensing faces for 1 million randomly distributed POIs in a crystal with a size of 25 x 25 25 mm. The same data is displayed in two different scales indicated by a colour corresponding to each of the y-axes.

Taking into consideration the results discussed above, the optimised design of the PET subsystem was determined to have a monolithic crystal size of 25 x 25 x 25 mm that is compatible with standard 1-inch photosensors and that has twice as much depth as conventional preclinical monolithic-detector PET scanners. Two photosensors placed one at the back face of the crystal and the other one at a perpendicular face were identified as the appropriate configuration that presents a suitable MAE of estimation performance without requiring an excessive amount of additional material and computation. Each one of the photosensors is chosen to have a commercially-available size of 8 x 8 channels that for the present configuration already provides the best performance achievable. A schematic

of the proposed system has already been presented in Fig. 2.8 and described in section 2.4.

3.2.2 Optical imaging subsystem precursor

The results of the optical simulation carried out in order to verify the preliminary functionality of a preclinical optical imaging subsystem composed of plenoptic detectors are presented below. The plenoptic-detectors system considered, the two-point-source phantom imaged and the simulation parameters employed are described in detail in section 2.3.2. An example of one of the ten dark-noise-inflicted projection images (with a signal-to-noise ratio of 5 dB) obtained from one of the ten plenoptic detectors in the system is shown in Fig. 3.14. As made evident from the enlargement on Fig. 3.14, this projection image contains the individual projections produced by each lens of the microlens array, on the corresponding subset of sensor pixels, of the light field emitted by the imaged phantom. Given the geometrical simplicity of the two-point-source phantom and the scatter-free propagation of its emitted light field, it is already possible to identify its structure in each individual lens projection within this plenoptic detector's projection image.

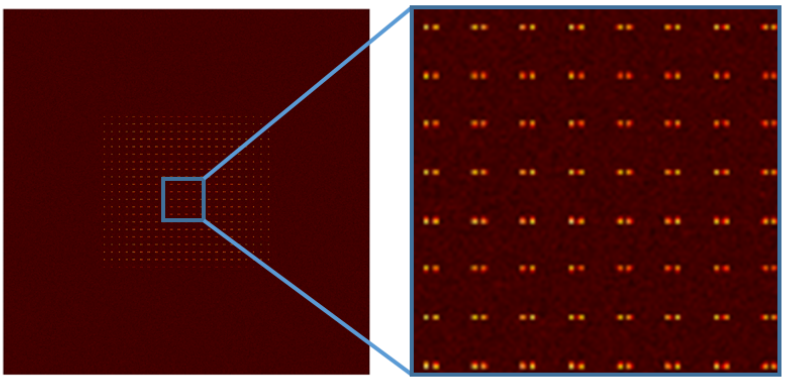

Figure 3.14: Noise-inflicted projection image corresponding to one of the 10 plenoptic detectors of the precursor system. The enlargement on the right shows the individual projections corresponding to some of the lenses in the microlens array.

As a consequence of the absence of photon scattering outside the spheres representing the point sources, for example caused by tissue, a simplification of the tomographic reconstruction process undertaken within the tool described in section 2.2.4 is attained. The ten dark-noise-inflicted projection images can therefore straightforwardly be reconstructed into a single three-dimensional image displayed in Fig. 3.15.

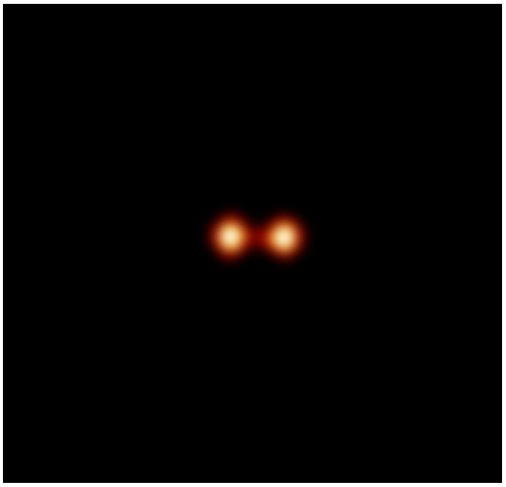

Figure 3.15: Tomographically reconstructed image using the ten projections obtained from the ten plenoptic detectors in the optical imaging precursor system. The imaged object is the two-point-source phantom, located at the centre of the FOV, with the point sources having a 1 mm diameter and being separated centre-to-centre by 2 mm.

As observed in Fig. 3.15, both point sources can be clearly visually identified and distinguished. This result suggests that such a system configuration has the capability of resolving volumetric light sources, such as the accumulation of an optical probe, with a resolution of 1 mm under ideal scatter-free conditions. It must be noted that said capability of optical imaging systems is known to be hindered by the presence of a scatter medium, such as tissue, of increasing depth and by the absence of additional positional information about the light sources [62].

3.2.3 Comparison between estimation algorithms

The results of the comparison between the two POI estimation algorithms described in section 2.2.2 and section 2.2.3 are presented below, namely the *ReSCoGs A-kNN* and CNN-based algorithms. Considering a single monolithic-crystal module of the PET subsystem, the POI estimation error obtained by both algorithms for one million randomly distributed scintillation events within the crystal is displayed. The full distribution of the obtained POI estimation errors along all three dimensions of the crystal is shown in Fig. 3.16 and in Fig. 3.17 for the *ReSCoGs A-kNN* and CNN-based algorithms respectively. For each of the three distributions per algorithm an interpolation curve as well as a Gaussian fit curve are also presented. The Gaussian fits are included with the purpose of showing how the error distributions do not fully approach them and how simply calculating their FWHM through their variance might therefore not be a reliable indicator of the POI estimation

resolution.

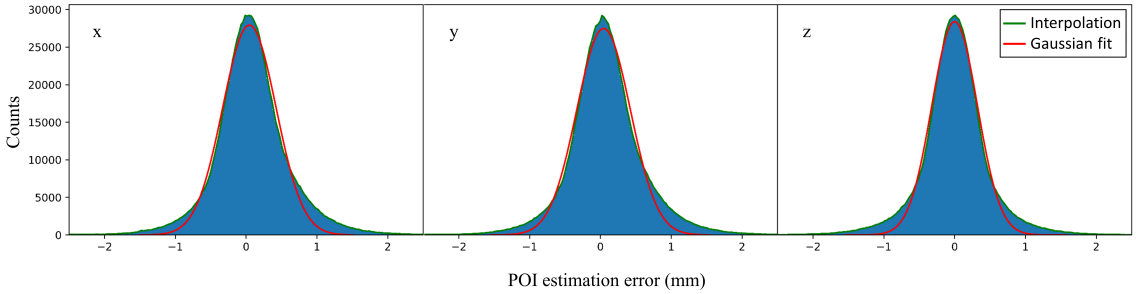

Figure 3.16: POI estimation error (estimated POI – simulation ground truth POI) histograms for the one million randomly distributed scintillation events within the crystal along each x, y, z dimension of the crystal obtained when using the *ReSCoGs A-kNN* algorithm. An interpolation of the distribution as well as a Gaussian fit of it are presented and labelled by their colour.

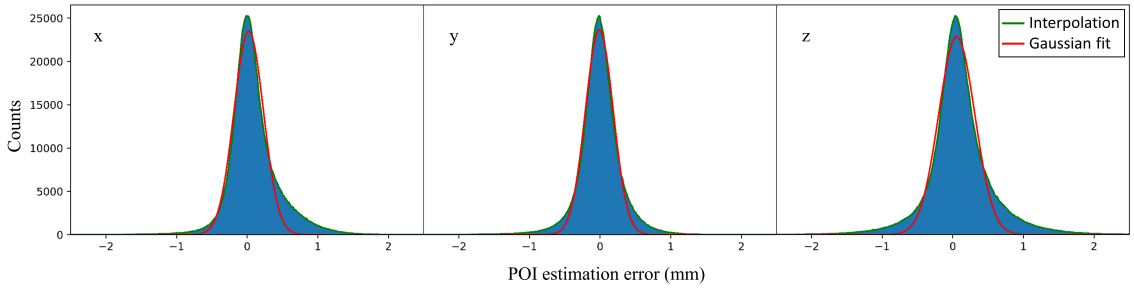

Figure 3.17: POI estimation error (estimated POI – simulation ground truth POI) histograms for the one million randomly distributed scintillation events within the crystal along each x, y, z dimension of the crystal obtained when using the CNN-based algorithm. An interpolation of the distribution as well as a Gaussian fit of it are presented and labelled by their colour.

In distributions such as these ones with so-called fat tails the FWHM or the half-width-at-half-maximum (HWHM) might be not statistically defined [63]. In this work the analytic FWHM of the distribution's interpolation, calculated with the procedure established by the NEMA Standards Publication NU 4-2008, along with the percentage of counts falling inside of it are therefore proposed as a representative of the distribution and thus as an indicator of the POI estimation resolution [55]. The FWHMs of the estimation error distributions obtained with the *ReSCoGs A-kNN* were 0.68 mm, 0.66 mm and 0.52 mm along the x, y and z dimensions respectively. With 59.3%, 59.4% and 56.7% of the counts occurring within them respectively. For the CNN-based algorithm the FWHMs of the estimation error distributions were 0.42 mm, 0.41 mm and 0.49 mm along the x, y and z dimensions respectively. With 61.0%, 69.3% and 57.6% of the counts occurring within them respectively.

The superior resolution observed along the z-dimension for the *ReSCoGs A-kNN* algorithm is explained by the fact that the sensors are placed on crystal faces lying on the xz and yz-planes, meaning that information about the z-coordinate of a POI is obtained twice at the CoG reduction step, once per sensor. Thus improving the euclidean minimisation stage of the algorithm along this dimension. The error distribution along the z dimension is also more symmetrical due to the same reason, which is amplified by the fact that no target space reduction is applied along that dimension. The resolutions along all three dimensions could therefore be made similar if at least three perpendicular crystal faces were coupled to sensors. The CNN-based algorithm, in contrast, shows a lower resolution along the z-dimension and a larger asymmetry in the tails of the error distribution along the x-dimension. Since it is not possible to know the features extracted and used by said algorithm it can only be theorised that these asymmetry effects are a result of the perpendicular photosensor readout configuration. In both cases the xy POI estimation resolution is below that obtained by other advanced POI estimation methods based on neural networks presented in literature that yield values of 0.78 mm and 0.96 mm using crystal depths of 8 mm and 10 mm respectively [64, 65]. Furthermore, the resolution along the z-dimension of the crystal, i.e. its depth, reported in these two studies is slightly above 1 mm. The combination of the system being proposed by this work and the two developed POI estimation algorithms thus present a high potential to be evaluated with an experimental study.

Using the same data as above, the intra-crystal position dependence of the estimation error along each of the three dimensions is shown in Fig. 3.18 and in Fig. 3.19 for the *ReSCoGs A-kNN* and CNN-based algorithms respectively. In these figure the crystal volume is divided into 25 x 25 x 25 1 mm^3 voxels, each one represented by one pixel in the plot. In each pixel, the MAE of estimation is shown for all events whose real POI occurred within that voxel. Each of the 25 images thus represents a one-voxel thick slice along the z-dimension of the crystal with increasing z-value from left to right and top to bottom as indicated by the z-arrow. In the new reference frame provided, the two sensors are coupled to the crystal one at the face lying on the xy-plane behind the image in the top left corner and the other at the face lying on the yz-plane going into the page perpendicular to the left side of each image. The average of the individual estimation MAEs along the three dimensions is presented in Fig. 3.20 and in Fig. 3.21 for the *ReSCoGs A-kNN* and CNN-based algorithms respectively. A gradual increase of the estimation error as the POIs occur further away from the photosensors can be observed for both algorithms. This effect suggests that neither of them is able to completely and uniformly overcome the asymmetry of the infor-

mation collected in the fluence images form such a perpendicular photosensor dual readout configuration. In order to increase the uniformity of the algorithms' response a third perpendicular photosensor could be added or alternatively a computational approach could be adopted where the positional estimation errors are considered at the PET reconstruction stage as confidence weights that would counteract such effect. Moreover, in both cases the estimation error along the y-dimension appears to be the most uniformly distributed. In this reference frame this is the dimension along which both planes of the photosensors lie and thus once more the effect of being able to represent the fluence images from a POI symmetrically and twice along this dimension is obtained.

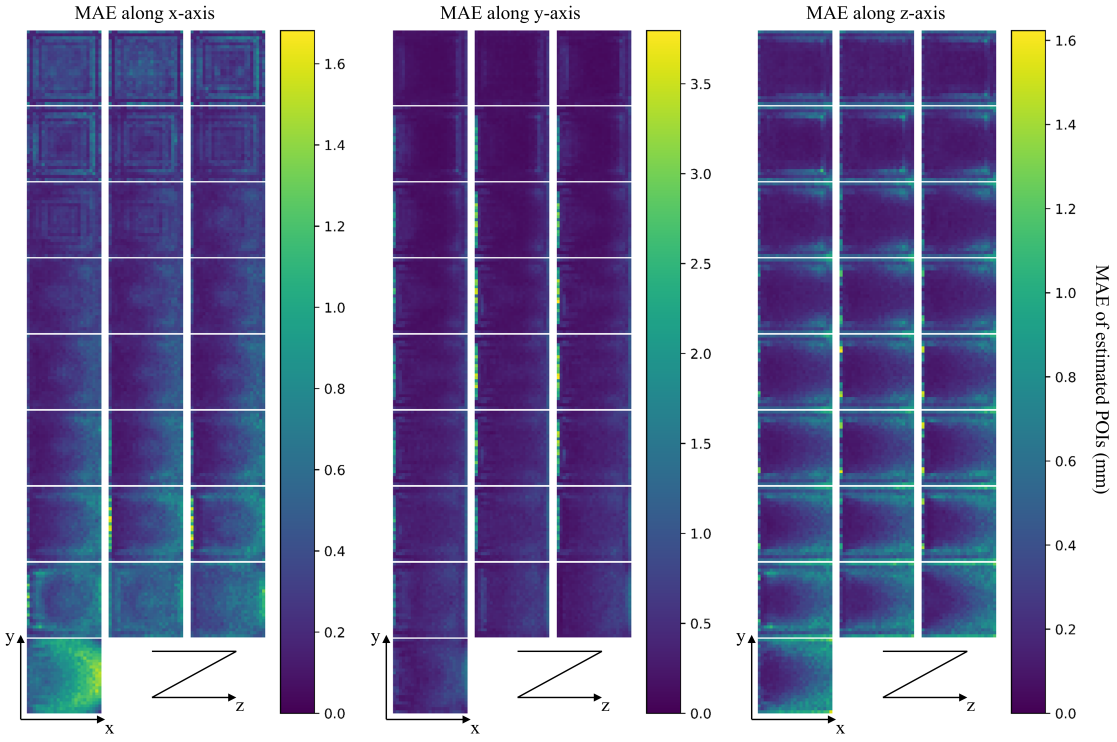

Figure 3.18: Position dependence of the estimation error along each of the three dimensions for the *ReSCoGs A-kNN* algorithm. The MAE of estimation is shown for all the events whose POI occurred at each 1 mm^3 voxel within the crystal, represented by one pixel in the images.

3.3 Performance evaluation

The performance evaluation of the system concept being proposed was carried out using the whole extent of the simulation and reconstruction frameworks described in detail in section 2.2 for each of the subsystems. A rendering of the Gate simulation with which the

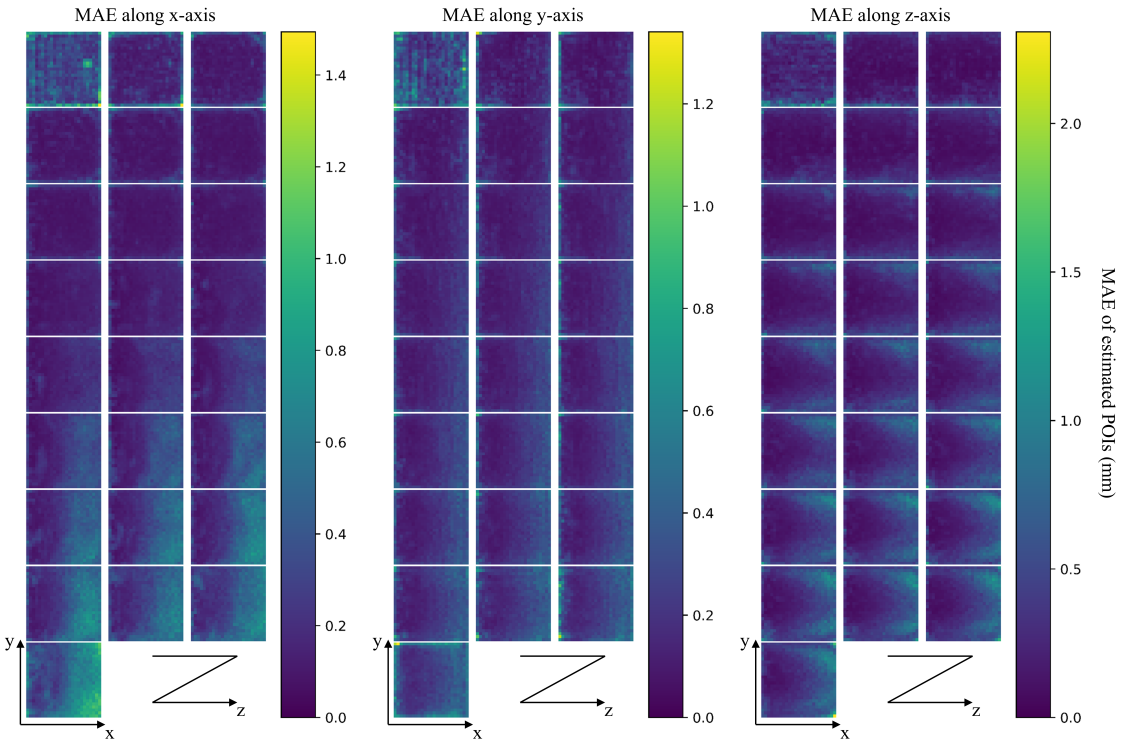

Figure 3.19: Position dependence of the estimation error along each of the three dimensions for the CNN-based algorithm. The MAE of estimation is shown for all the events whose POI occurred at each 1 mm^3 voxel within the crystal, represented by one pixel in the images.

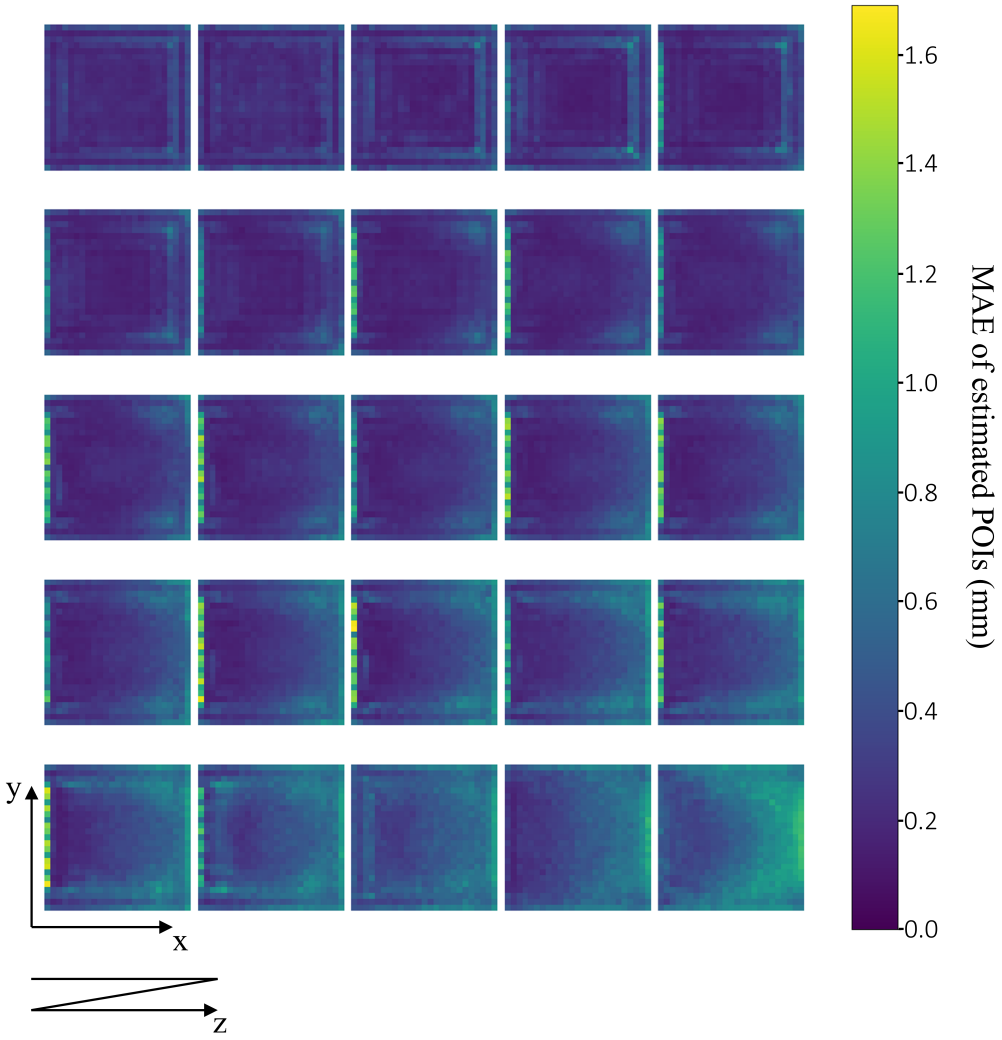

Figure 3.20: Position dependence of the estimation error averaged on the three dimensions for the *ReSCoGs A-kNN* algorithm. The MAE of estimation is shown for all the events whose POI occurred at each 1 mm^3 voxel within the crystal, represented by one pixel in the image.

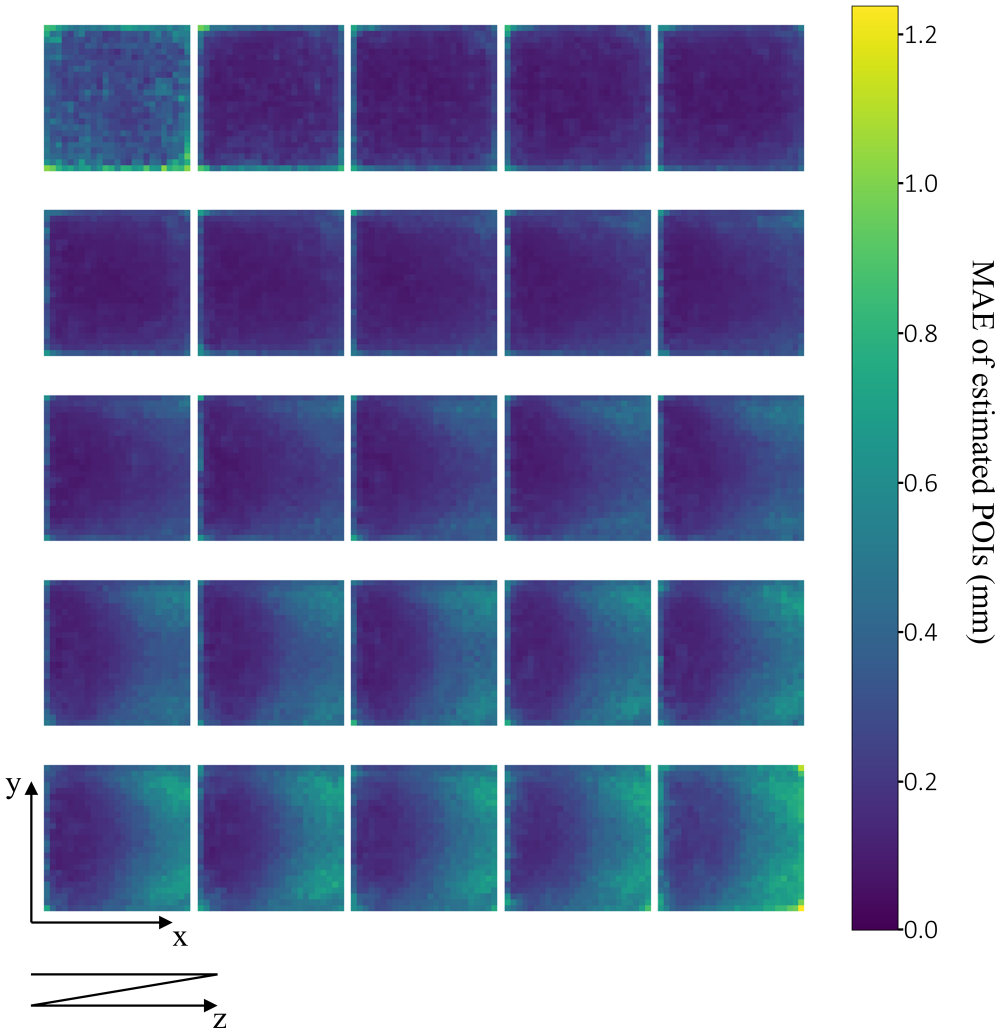

Figure 3.21: Position dependence of the estimation error averaged on the three dimensions for the CNN-based algorithm. The MAE of estimation is shown for all the events whose POI occurred at each 1 mm^3 voxel within the crystal, represented by one pixel in the image.

monolithic-detector PET framework begins is shown in Fig. 3.22 for said system being proposed by this work. The simplified structure of the system being simulated can be clearly appreciated with the monolithic crystals being represented as empty cubes with white edges, the two perpendicular photosensors per module as solid yellow rectangular prisms and the plenoptic detector as a solid blue rectangular prism. As mentioned before, the material of the crystals was set to be LYSO while that of the photosensors and plenoptic detectors was set as silicon. For visualisation purposes the phantom being simulated in this case is a point source at the centre of the scanner's FOV and only a few gamma-ray trajectories, shown as thin green lines, are displayed.

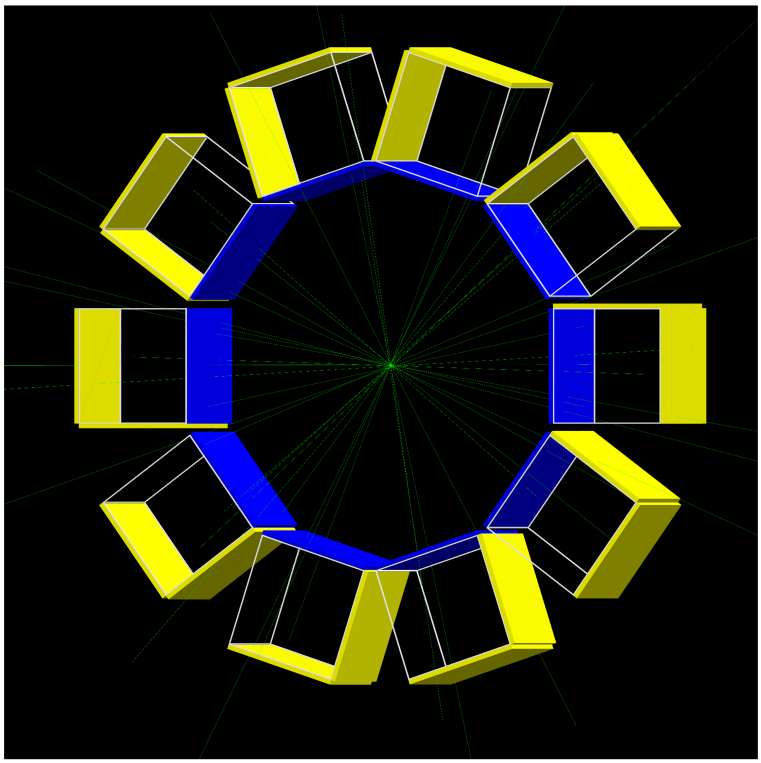

Figure 3.22: Rendering of a Gate simulation of the proposed system. Monolithic crystals are represented as empty cubes with white edges, photosensors as solid yellow rectangular prisms and plenoptic detectors as solid blue rectangular prisms. The phantom being simulated is a point source at the centre of the scanner's FOV and gamma-ray trajectories are shown as thin green lines.

3.3.1 PET subsystem performance characteristics

The performance of the PET subsystem was evaluated through the two main criteria and procedures proposed by the NEMA Standards Publication NU 4-200 protocol. These are

the spatial resolution and the sensitivity of a preclinical PET scanner. The results of the procedures, described in section 2.5.1, are presented below.

Spatial resolution

The FWHM of the point spread function obtained at the centre of the axial axis of the scanner for different positions along its radial axis is shown in Fig. 3.23 for the three scanner dimensions. Two different scanner configuration cases are presented, the complete proposed multimodal system and the isolated monolithic-detector PET subsystem in the absence of the plenoptic detectors. The minor effect of the presence of the plenoptic detectors attached to the bore-facing side of the monolithic crystals can be observed and resulted in all cases in a decrease of the FWHM of the point spread function that was under 5% for all positions. The FWHM values for the point spread functions with and without the presence of the optical imaging subsystem were obtained in a range between 0.58 mm and 1.24 mm. The values oscillate in the characteristic way observed in preclinical scanners due to the fact that the arrangement of crystals yields a polygon, in this case a decagon, that approaches a circular symmetry only to a limited extent. Furthermore, the variance of the values obtained per configuration and per radial position resulted in a FWHM uncertainty that does not exceed 1.5% in any of the points, thus making the error bars barely visible. The spatial resolution values obtained are comparable to those reported in the literature for preclinical monolithic-detector PET systems that oscillate between values in the range of 0.60 mm and 1.92 mm [61, 66].

Geometrical efficiency

The sensitivity of the scanner was determined by measuring its geometrical efficiency using Eq. 2.3 as a function of the position of a point source along the axial direction. The results obtained are presented in Fig. 3.24 for both the complete multimodal system and for an alternative system with the same design but with the only difference of having a 13 mm crystal depth corresponding to approximately half the crystal depth of the proposed system. The geometrical efficiency of both systems considered follows the same axial pattern, peaking at the axial centre of the FOV and decreasing towards the edges. This is the expected pattern for such type of analysis with a point source being placed at the radial centre of a scanner. Explained by considering its isotropic emission of back-to-back gamma-rays and the pivotal coincidence-detection mechanism of PET scanners. Indeed, at the axial edges of a scanner's FOV only the back-to-back gamma-rays emitted on the transversal planes lying at those axial edges can be detected as coincident. A slight obliqueness away from those planes would mean that one of the gamma-rays would exit the axial FOV of

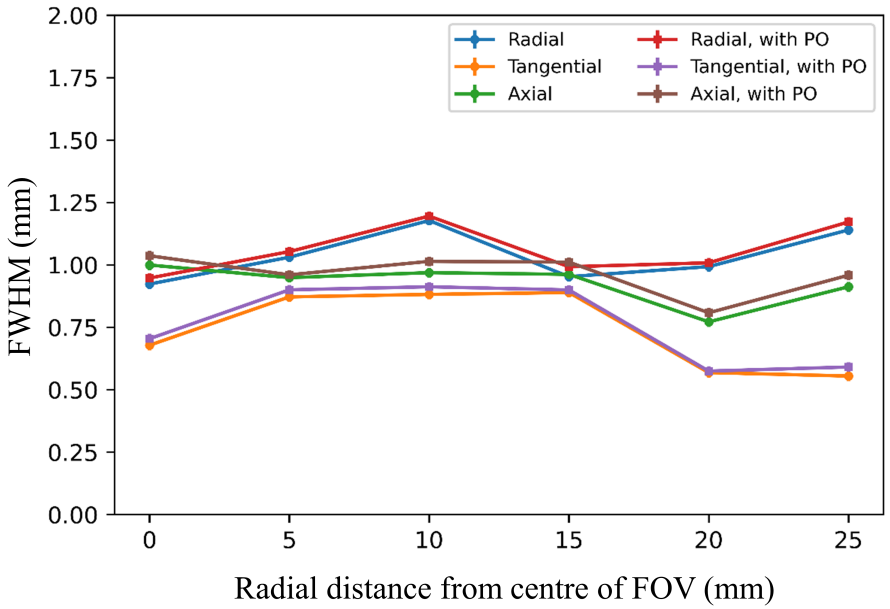

Figure 3.23: Spatial resolution of the PET subsystem on all three dimensions as a function of the position along its radial axis, measured as the FWHM of the PET subsystem's point spread function in the presence and absence of the optical imaging subsystem.

the scanner thus escaping detection. The geometrical efficiency is thus observed to vanish towards these axial edges of the subsystem's FOV. In contrast, at the axial centre of a scanner's FOV the maximum axial obliqueness of a back-to-back emission that results in a valid line of response is allowed.

As expected, the geometrical efficiency of the proposed PET subsystem across all axial positions, except for the axial edges of the FOV, is essentially twice as large as that of the alternative system. This is an obvious result of the fact that the volume of sensitive scintillating material in the proposed system is twice as much as that in the alternative one, thus making it able to detect twice as many gamma-rays emitted by the same source activity. The peak geometrical efficiency of 3.9% obtained for the proposed PET Subsystem lies close to the centre of the range of absolute sensitivities reported for a series of commercial preclinical PET scanners of 0.9% - 9.3% [61, 67]. This is however an indicative comparison taking into account the simplified way of investigating a scanner's sensitivity through its geometrical efficiency presented in this work. The PET subsystem being proposed as a proof-of-concept, however, consists of a single ring of modules yielding an axial length of 25 mm. This axial length lies below the range of 37 mm - 150 mm reported for a series of conventional commercial preclinical PET scanners [61]. Taking into account the

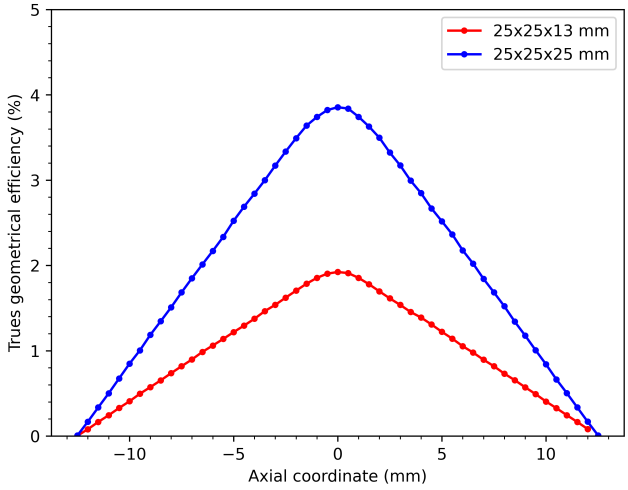

Figure 3.24: Geometrical efficiency obtained from true coincidences with respect to the position of a point source along the axial dimension. Shown both for the proposed PET subsystem and for a comparative alternative system with crystal depth of 13 mm. The two cases are labelled by the size of the monolithic crystals employed by the systems.

obliqueness-of-LoRs effect described above, it becomes evident that the larger the axial length of a scanner the larger its sensitivity. The obtained peak geometrical efficiency is therefore a notable result for such a scanner's axial length, obtained from the unconventionally large depth of the monolithic crystals being employed. In this way, such a PET subsystem concept is demonstrated to have comparable spatial resolution and geometrical efficiency to its commercially available counterparts of longer axial length while being at the same time coupled to the optical imaging subsystem.

3.3.2 PET subsystem's imaging capabilities

The PET imaging capabilities of the proposed system were evaluated through the imaging procedure of a Derenzo phantom, described in section 2.5.2, using the full PET simulation and reconstruction framework. The results of the final reconstruction stage of the framework are shown in Fig. 3.25 and in Fig. 3.26 for the cases where the *ReSCoGs A-kNN* algorithm and the CNN-based algorithm were used respectively. In both cases the central slice along the axial dimension is presented on the left side, together with an intensity line profile along y =31 mm on the right side. In both of the images the rods down to a diameter of 1 mm can be visually resolved with a slight yet evident greater clarity in the case of the image corresponding to the CNN-based algorithm. This difference is further confirmed by the peak patterns corresponding to the 1.25 mm-diameter rods in the two line profiles.

Where the peak-to-valley distances are larger than the peaks' amplitudes in both cases but even larger in the CNN-algorithm's case.

From the line profile corresponding to the *ReSCoGs A-kNN* algorithm the two peaks expected to arise from the two 1 mm rods along the profile cannot be confidently identified. In the line profile corresponding to the CNN-based algorithm these peaks become perceptible if however with a peak-to-valley extent of less than the peaks' amplitudes. The higher imaging performance obtained for the CNN-based algorithm is obtained in accordance to the superior POI estimation resolution exhibited by it and discussed in section 3.2.3. As mentioned before, however, in both cases the smallest rod diameter that can be confidently identified from the line profiles is the same one, namely a 1.25 mm diameter. Thus indicating a consistent overall imaging performance of the PET subsystem when operated with any of these two proposed algorithms. This result is comparable to the smallest rod diameters of 1.25 mm and 1.2 mm clearly resolved by both conventional preclinical PET scanners well established in the market and by recent commercial monolithic-detector ones [48, 66]. For both of which, however, the experimental imaging process of a Derenzo phantom is not limited to the acquisition of 20 million coincidence events as it is in the simulation approach used in this work by computational resources.

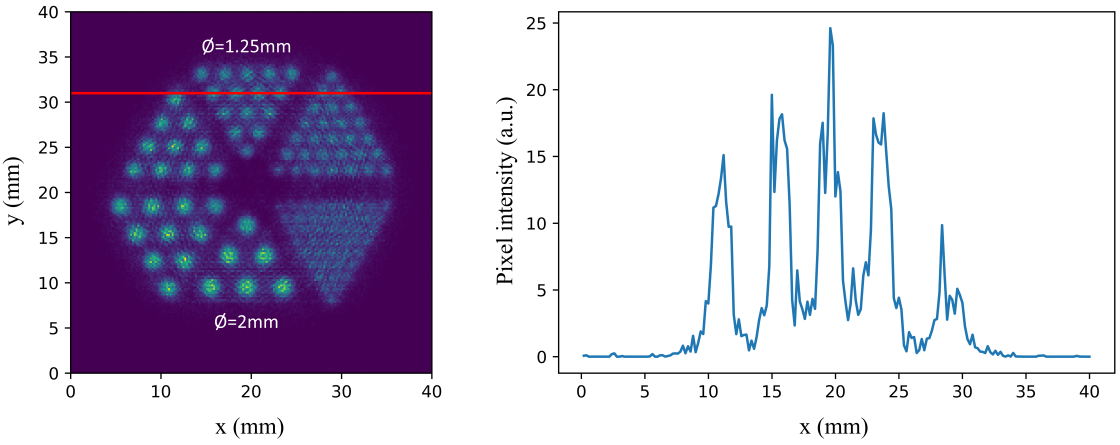

Figure 3.25: PET imaging capabilities of the proposed system displayed as the central slice along the axial dimension of the reconstructed image (left side) obtained for the Derenzo phantom using the *ReSCoGs A-kNN* algorithm in the framework. The rod diameters of the Derenzo phantom arrays are 2 mm, 1.75 mm, 1.5 mm, 1.25 mm, 1 mm and 0.75 mm respectively in the clockwise direction starting from the central array in the bottom. Right side: intensity line profile along y =31 mm.

The highest PET imaging capability of the proposed system design independent of the POI

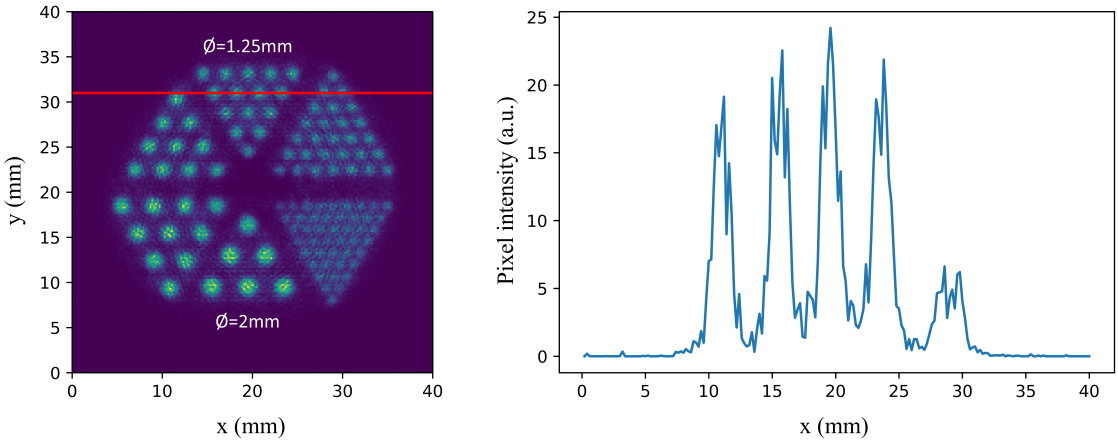

Figure 3.26: PET imaging capabilities of the proposed system displayed as the central slice along the axial dimension of the reconstructed image (left side) obtained for the Derenzo phantom using the CNN-based algorithm in the framework. The rod diameters of the Derenzo phantom arrays are 2 mm, 1.75 mm, 1.5 mm, 1.25 mm, 1 mm and 0.75 mm respectively in the clockwise direction starting from the central array in the bottom. Right side: intensity line profile along y =31 mm.

estimation algorithm being employed is shown in Fig. 3.27. Specifically by the image on the top left corner that presents the reconstruction output obtained from the ground-truth POIs of the same simulation mentioned above. These POIs are then directly discretised into PET data without the simulation of their corresponding scintillations. Thus representing the case where a POI estimation algorithm with an estimation error of FWHM = 0 mm is used. In this image even the smallest rods with a diameter of 0.75 mm can be clearly visually resolved. This results thus demonstrates the effect of the POI estimation error on the quality of the final reconstructed image and motivates the improvement of the algorithms used for said task. The rest of the images represent the cases were the same ground-truth POIs have been blurred by errors randomly drawn from a Gaussian distribution whose FWHM is indicated under the image. Once more showing the effect of the POI estimation resolution on the PET imaging performance of the proposed system.

3.3.3 Bi-modal acquisition simulation

The overall imaging capability of the proposed PET-OT system was assessed in a realistic preclinical context by simulating the imaging acquisition of a tumour-bearing mouse phantom. The results for the simulations corresponding to each of the two subsystems are presented in the sections below.

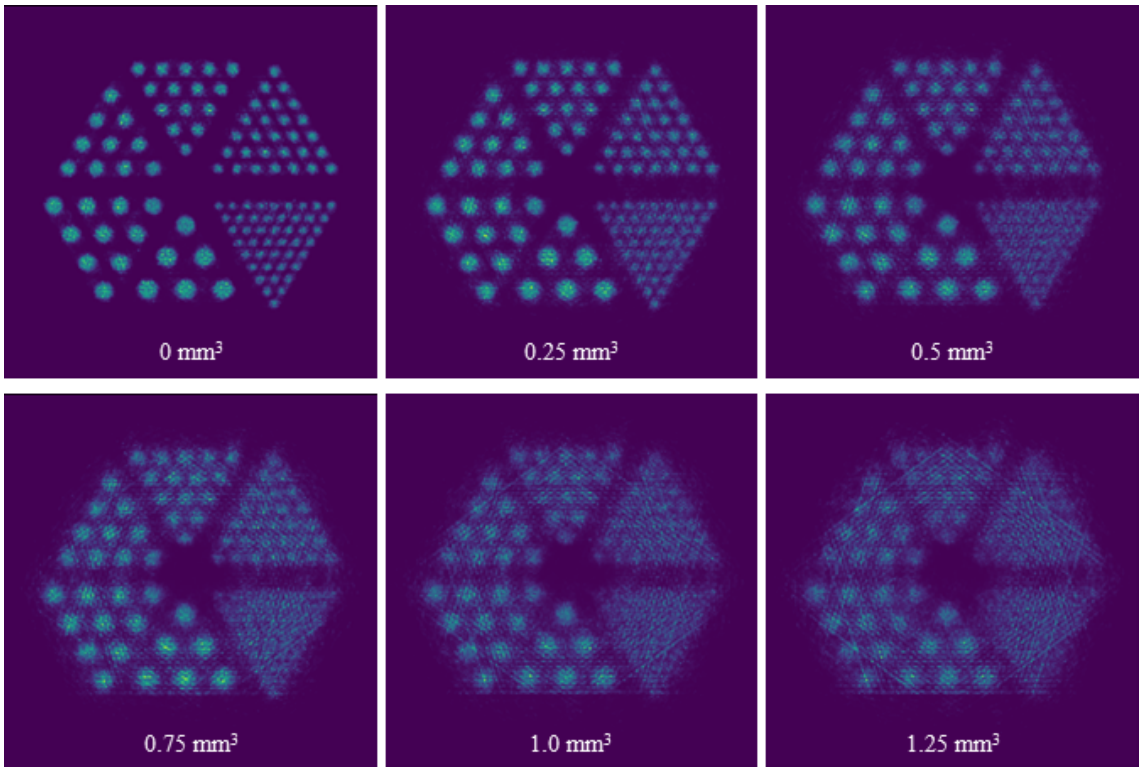

Figure 3.27: Effect of the POI estimation resolution on the final PET reconstructed image for the proposed system. Transverse slice at the axial centre of the reconstructed images from the same ground-truth POIs being blurred by Gaussian distributions of different FWHM, mimicking the estimation error of a POI estimation algorithm. The FWHM of the distribution used is indicated below each image.

PET imaging

The results of the PET simulation carried out as part of the final inspection of the proposed system are shown in Fig. 3.28. The PET subsystem considered, the characteristics of the voxelised tumour-bearing mouse phantom imaged and the simulation process employed are described in detail in sections 2.4.1, 2.5.3 and 2.2.1 respectively. The inserted tumour was approximately 2.5 mm in radius and is indicated by a white arrow on Fig. 3.28a, which is a coronal slice of the voxelised phantom along the sagittal centre of the tumour. The different colours on this image indicate the organs and tissues having a different voxel number and thus being assigned a different density and activity. The activity assigned to each tissue and organ, as indicated in Table 2.3, was determined according to the uptake values reported in an external study for the 18F-Galacto-RGD radiotracer [59]. The activity assigned to the tumour corresponds to the uptake reported in the same study for a tumour composed of M21 melanoma cells. A final 3D reconstructed image was obtained from 20 million coincidence events using the simulation framework in conjunction with the *ReSCoGs A-kNN* algorithm. Slices of said images centring the tumour are shown in Fig. 3.28b-d on the coronal, sagittal and transverse planes respectively. All three images show the reconstructed activity distribution from which some organs such as the liver and bladder can be clearly recognised due to their presence on those slices and to their uptake levels for the radiotracer being considered. In all three cases the tumour can also be clearly recognised with a clarity corresponding to its radiotracer uptake relative to that of the organs present in the slice.

Furthermore, due to the limited number of coincidence events considered the images can be seen to have a coarse activity representation and a low activity background. Nevertheless as mentioned before in spite of this limitation the tumour and organ structures can be clearly identified. In the absence of a corresponding anatomical image, the reconstructed activity distributions were overlayed on the stimulated phantom itself in order to see the agreement of the distribution with the ground-truth position of the organs. This overlayed images are shown in Fig. 3.28e-g corresponding to the slices above them. This is a practice only possible with simulation data. A clear visual positional agreement is observed particularly for the liver and the tumour. In light of the promising system performance presented in the previous sections, the accomplishment of these images as valuable biological indicators in spite of the low number of events being considered is both expectable and notable.

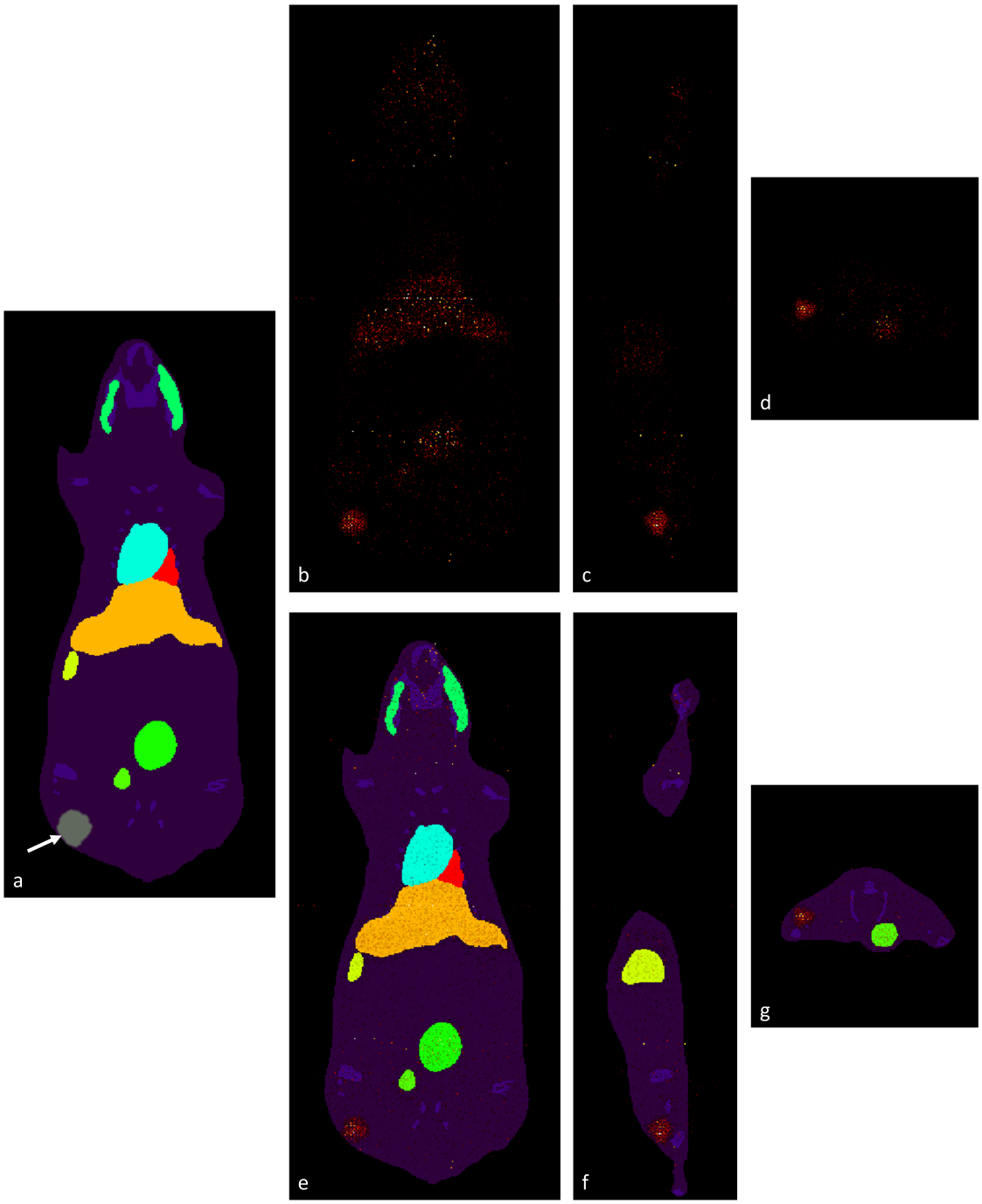

Figure 3.28: Image reconstruction results for 20 million events obtained form the simulation of a mouse phantom with an inserted M21 melanoma tumour on its flank. a) Voxelised phantom used in the simulation. The different colours indicate the organs, tissues and tumour having a different voxel number and thus being assigned a different density and activity. A white arrow indicates the tumour. b-d) Slices of the reconstructed image centring the tumour on the coronal, sagittal and transverse planes respectively. e-g) Same slices overlayed on top of the corresponding slices of the phantom. The activity assigned to the phantom is indicated in Table 2.3 and corresponds to the uptake of 18F-Galacto-RGD radiotracer [59].

Optical tomography

The results of the optical simulation carried out as part of the final inspection of the proposed system are presented below. The plenoptic-detectors subsystem considered, the mesh version of the mouse phantom imaged and the simulation process employed are described in detail in sections 2.4.2, 2.5.3 and 2.2.4 respectively. The light propagation simulated with the tool described in section 2.4.2 for the RFL-bound tumour within the phantom is shown in Fig. 3.29b-d as photon fluence images on the coronal, sagittal and transverse planes of the mouse respectively. In each of the three images the intersection of the light field with the surface of the mouse is indicated by the green colouring of the corresponding image pixels. The illuminated outer surface is what would be seen if a real mouse imaged in such conditions would be looked at with a conventional optical camera or a human eye. The photons that escape this surface are those that travel to the plenoptic detectors and generate the light field projections acquired by the system. The mesh representation of the mouse phantom used for this simulation is displayed to the left of the fluence images (Fig. 3.29)a.

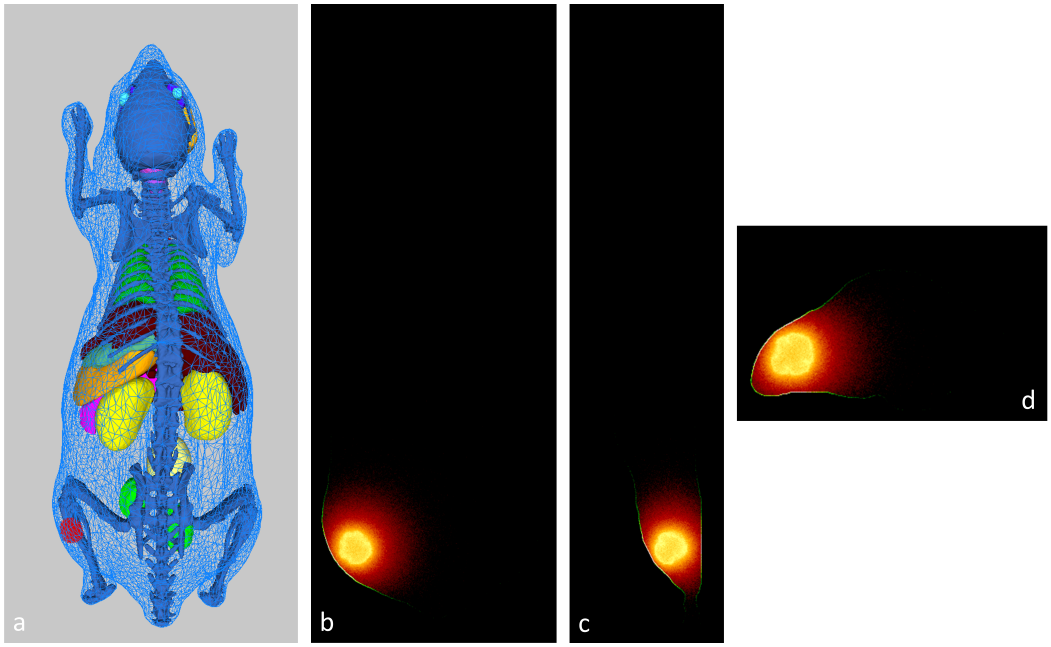

Figure 3.29: Light propagation simulation results for the RFL-bound tumour within the mouse phantom. a) Mesh representation of the mouse phantom used for this simulation, b) fluence image on the coronal plane, c) fluence image on the sagittal plane, d) fluence image on the transverse plane. The intersection of the light field with the surface of the mouse is indicated in each of the fluence images by the green colouring of the corresponding image pixels.

All ten dark-noise-inflicted projection images (with a signal-to-noise ratio of 5 dB) ob-

tained from each of the ten plenoptic detectors in the system are shown in Fig. 3.30. As seen in Fig. 3.30, most projection images can be identified to contain the individual projections produced by each lens of the microlens array, on the corresponding subset of sensor pixels, of the light field emitted by the tumour in the imaged mouse phantom. This group of individual projections shifts its relative potion within the imaging plane of the corresponding plenoptic detector and displays a different level of clarity as a consequence of the position and orientation of each of the ten plenoptic detectors with respect to the light source's position. Given the unsymmetrical position of the light source, in this case the tumour, within the mouse phantom that embodies a scatter medium, the further reconstruction of these type of projection images requires the use of additional priors to be provided to the simulation and reconstruction tool. Employing the Lipros reconstruction tool presented in section 2.2.4 and using the results of the PET simulation presented in the section above as a reconstruction prior, a final 3D reconstructed result of the complex scenario was obtained [68]. Representations of this result are shown in Fig. 3.31 as intensity point clouds visualised from six different angles. From these images, the spatially varying intensity of the reconstructed light source can be correlated to the simulated presence of the RFL-probe bound to the tumour. Said biological information could then be further correlated to the PET results in order to be better quantified and localised, thus confirming the successful integrated multimodal application of the proposed system.

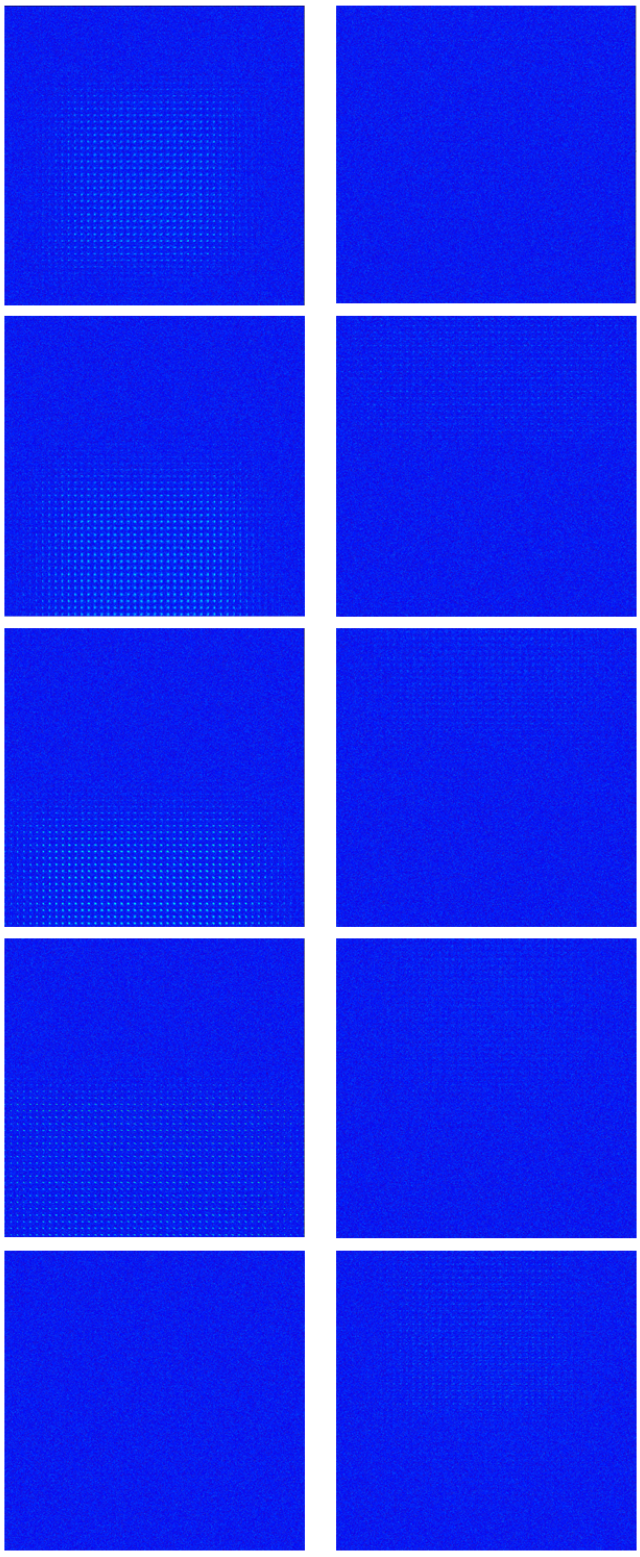

Figure 3.30: Noise-inflicted projection images corresponding to the 10 plenoptic detectors of the optical imaging subsystem. The light field being imaged is produced by the RFL-bound tumour within the mouse phantom.

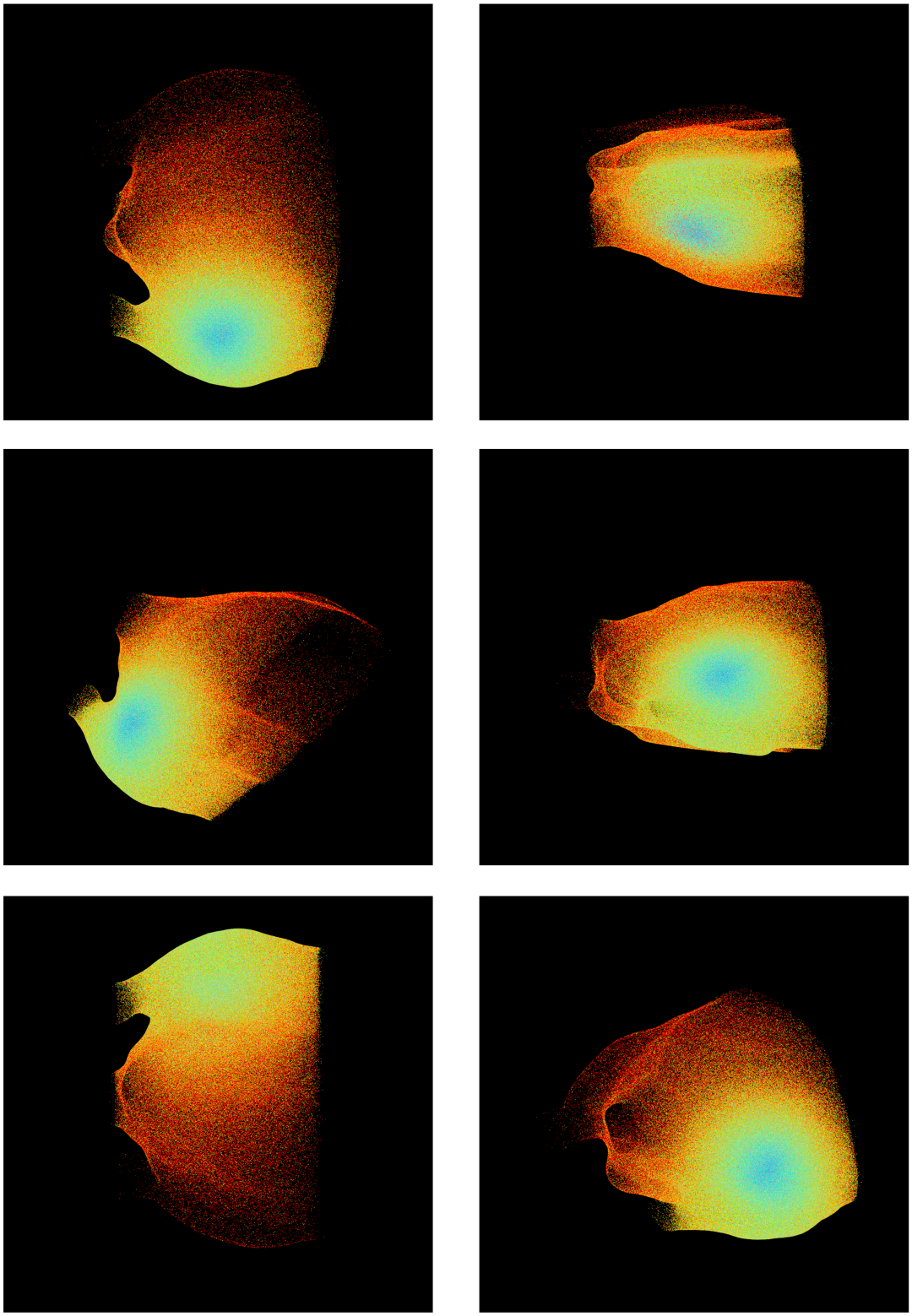

Figure 3.31: Reconstruction result for the simulated RFL-expressing tumour within the mouse phantom using the 10 plenoptic projections displayed in Fig. 3.30 and the results of the PET reconstruction as a prior. Intensity point clouds visualised from six different angles are presented.

Conclusions

Do the best you can until you know better. Then when you know better, do better
- Maya Angelou

In light of the ample potential that would be presented by the capacity of simultaneously detecting gamma-rays and optical-probe photons, this work has set to develop a concept for an integrated system being capable of achieving such task. With such a system, unprecedentedly correlated functional and anatomical information could be obtained that would be useful to a variety of applications. The main imminent applications that would benefit from said information correlation, and that therefore motivated this work too, include drug development and pharmacokinetics, the study of tumour models and radiobilogy, and the advancement of optical tomography techniques [4, 7]. As the result of a developmental process based on computational simulations and focused on the design of an appropriately suiting PET subsystem, a system concept consisting of detector modules that combine monolithic scintillating crystals with plenoptic detectors was presented. Each module of this system is specifically composed of a 25 x 25 x 25 mm LYSO crystal with two 8 x 8-channel photosensors of matching 2D size coupled to its back face and to another perpendicular face and a plenoptic detector of the same 2D size coupled to its bore-facing face as illustrated in Fig. 2.8.

A simulation and reconstruction framework for the investigation of monolithic-detector

PET systems was developed for the conception and analysis of said proposed system. Within this framework, two alternative algorithms required for the operation of monolithic-detector PET systems were developed respectively based on a k-nearest neighbours (kNN) and a convolutional neural network (CNN) approach. The former, named *ReSCoGs A-kNN*, is based on the reduction of the fluence images obtained for each event by the photosensors in a module into three representative features. These are their centre of gravity, the index of the photosensor channel with the highest number of photons recorded and the sum of recorded photons over all channels. Using the latter two features the algorithm applies a target space reduction that then allows it to effectively minimise the distance between the centre of gravity feature of a test event and those of the reduced space. In this way the POIs of the detected gamma-rays can be determined with a POI estimation FWHM-resolution of 0.68 mm, 0.66 mm and 0.52 mm in the x, y and z dimensions respectively for a monolithic-detector module such as the one in the proposed system. In order to obtain said resolution values the characteristics of the *ReSCoGs A-kNN* were previously investigated in depth with a focus on the representation fidelity and uniqueness of the *CoG* feature. This then led to the introduction of the target space reduction component of the algorithm. The optimisation of this algorithm for such detector configuration yielded k and n_p values of 85 and 35 respectively.

The other POI estimation algorithm developed, referred to as CNN-based, consists of a convolutional neural network whose structure is illustrated in Fig. 2.7. In contrast to the first algorithm, for this one no conscious fluence image reduction into specific features is initially applied. The POI estimation FWHM-resolution obtained from this algorithm was 0.42 mm, 0.41 mm and 0.49 mm in the x, y and z dimensions respectively for a monolithic-detector module such as the one in the proposed system. In the case of both algorithms the xy POI estimation resolution is below that obtained by other advanced POI estimation methods based on neural networks presented in literature that yield values of 0.78 mm and 0.96 mm using shallower crystal depths of 8 mm and 10 mm respectively [16, 17]. As a result of the perpendicular photosensor configuration the POI estimation resolution is innovatively sustained at such high levels for all three dimensions of the crystal in spite of its exceptional depth. The uniformity of this resolution within the crystal volume was also investigated and shown to fluctuate with a greater extent in the two dimensions spanned only once by a photosensor. Thus indicating the intrinsic effect of the perpendicular dual readout configuration of the proposed system on the POI estimation process.

Three main characteristics of the PET subsystem were optimised in order to reach the fi-

nal proposed design. These were the crystal depth, the number of crystal faces to which a photosensor was coupled and the number of channels per photosensor. For the employed perpendicular readout configuration no significant loss of POI estimation resolution was observed when increasing the crystal depth from conventional values around 10 mm until the chosen value of 25 mm. Furthermore, the improvement observed when coupling three or more photosensors to the crystal was not deemed significant enough for the design to incorporate such higher number that would result in increased complexity. In a similar way, the effect of increasing the number of channels per photosensor was observed to be insignificant thus justifying the choice of using commercially available 8 x 8 channel SiPM photosensors. In an equivalent procedure, the functionality of an optical imaging subsystem precursor was confirmed by using a previously developed tool for the simulation and reconstruction of plenoptic-detector optical tomography systems. The reconstruction of two light field- emitting point sources was used as a proof-of-concept for such type of system. The development and characterisation of the proposed multimodal system was therefore primarily based on the conception and investigation of its PET subsystem through the pertinently created framework. While the feasibility of the proposed system was evaluated through the investigation and optimisation of its components' characteristics and their impact on different performance criteria as well as on reconstructed-image quality.

The performance of the proposed system was initially evaluated through the analysis of standard PET figures of merit, namely its spatial resolution and sensitivity. These were assessed with procedures based on those established by the NEMA Standards Publication NU 4-2008. The spatial resolution obtained ranged between 0.58 mm and 1.24 mm FWHM of the point spread function of the system across the radial dimension. Such values obtained are comparable to those reported in the literature for preclinical monolithic-detector PET systems that oscillate between values in the range of 0.60 mm and 1.92 mm [61, 66]. The sensitivity of the PET subsystem was evaluated as its geometrical efficiency which presented a peak value of 3.9% that lies close to the centre of the range of absolute sensitivities reported for a series of commercial preclinical PET scanners of 0.9% - 9.3% [61, 67]. In this way, the PET subsystem was demonstrated to have comparable spatial resolution and geometrical efficiency to its commercially available counterparts of longer axial length while being at the same time coupled to the optical imaging subsystem.

The imaging capabilities for both of the imaging modalities were assessed with the use of phantom simulations. A Derenzo PET phantom as well as a tumour-bearing mouse phantom were composed and investigated. The reconstruction of the Derenzo phantom

was carried out using the two proposed POI estimation algorithms, both of which yielded image results from which rods of 1.25 mm could be clearly identified by line profiles with peak-to-valley ratios of more than half of the peaks' amplitudes. These results are comparable to the smallest rod diameters of 1.25 mm and 1.2 mm clearly resolved by both conventional preclinical PET scanners well established in the market and by recent commercial monolithic-detector ones [48, 66]. For both of which, however, the experimental imaging process of a Derenzo phantom is not limited to the acquisition of 20 million coincidence events as it is in the simulation approach used in this work by computational resources.

The simulation of a tumour-bearing mouse phantom was used to represent a realistic multimodal imaging situation in a preclinical context. The radiotracer activity assigned to each tissue, organ and to the tumour, as indicated in Table 2.3, was determined according to the uptake values reported in an external study for the 18F-Galacto-RGD radiotracer [59]. Image slices across all three phantom planes showed the reconstructed activity distribution from which some organs such as the liver and bladder can be clearly recognised. In the three cases the tumour can also be clearly recognised with a clarity corresponding to its radiotracer uptake relative to that of the organs present in the slice. Given the promising system performance obtained through the evaluation procedures applied, the accomplishment of these images as valuable biological indicators in spite of the low number of events being considered is both expectable and a favourable result indicating the notable performance of the system.

As a result of the performance evaluation and imaging assessments, the feasibility of the proposed multimodal system was demonstrated through its imaging outcomes that indicate a successful multimodal functionality with high PET performance characteristics. The first main outcome of this work is therefore a simulation and reconstruction framework for the development and investigation of monolithic-detector PET designs along with two high-performing algorithms used for the operation of said types of systems. The other main outcome of this work is the concept for an integrated multimodal PET-OT system whose promising potential has been demonstrated through the use of computational simulations.

The demonstrated potential of the proposed system and the insight obtained about the detailed operation of monolithic-detector PET systems finally appeal for a new experimental study to validate the results here obtained and to further advance the development of this

system concept. In particular two main areas of further investigation have been identified. The first one regards the experimental acquisition of the 3D grid of training POIs. Said grid of POIs is a key element of the proposed PET subsystem on which the POI estimation algorithms rely. The physical generation of such type of grids is an ongoing challenge being explored by the monolithic-detector PET community due to the so-far time and effort-consuming process of generating enough data with an appropriate distribution and uniqueness [69]. Furthermore, obtaining also the depth coordinate of a POI of collimated gamma-rays with the use of a single photosensing crystal face is an added challenge even for shallow monolithic crystals. Using the advantage of having a second perpendicular photosensor, as included in the proposed multimodal system, a potential method for achieving the creation of such 3D training POI grid has already been hypothesised as conceptual collateral product of the work here presented.

Lastly, the advantage of a PET image reconstruction method tailored to data obtained from monolithic detectors has been identified. In the monolithic-detector PET simulation and reconstruction framework developed as part of this work the estimated POIs are discretised into 1 mm^3 voxels within the crystal volume. This limitation imposed on the 3D coordinates of the POIs constitutes a loss of information in the form of an added systematic POI determination resolution. Said limitation arises from the data format requirements of universal image reconstruction tools employing conventional reconstruction techniques. To address this undesired constraint, the development of a novel appropriate image reconstruction method for raw monolithic-detector PET data has been identified as a need and preliminarily attempted. In this reconstruction method the direct 3D coordinates of the POIs would be connected to form LoRs with their uncertainty indicated instead by the resolution of the POI estimation algorithm for each voxel in the crystal volume, as previously shown in the error estimation uniformity maps. The POI estimation resolution corresponding to each voxel would then be considered as a confidence weight tied to the LoRs obtained form events occurring within that voxel. Developing said image reconstruction method thus constitutes another project that branches out of this work.

The outcomes and outlook of this work therefore not only motivate the conduction of a new study to experimentally validate the potential of the proposed system but also strive to contribute to the transition towards monolithic detectors for the advancement of PET systems and the development of new multimodal techniques that might one day be used in a clinical setting.

Appendix

List of Figures

1.1 Decay scheme for the conventional PET radiotracer $^{18}_{9}\mathrm{F}$ 7
1.2 Diagram showing the path travelled by a positron after the β^+ decay of a $^{18}_{9}\mathrm{F}$ nucleus and the direct annihilation with an electron 8
1.3 Probability of interaction between an incident photon and a NaI(Tl) medium, subdivided into different interaction mechanisms 11
1.4 Relative importance of the three interaction mechanisms between energetic photons and matter 12
1.5 Schematic of the energy band structure of an inorganic scintillator 14
1.6 Normalised scintillation emission spectra of four inorganic crystals 14
1.7 Simplified representation of a scintillation radiation detector composed of a scintillator coupled to a PMT 16
1.8 Photograph of a conventional PET block detector configuration 17
1.9 Schematic of a PET block detector and flood map obtained by a real detector with such configuration 19
1.10 SiPM: photograph and diagrams of its electronic and semiconductor structures 20
1.11 Photograph displaying various sizes and configurations of SiPM arrays . . 22
1.12 Diagram illustrating the three types of coincidence events detected by a PET scanner 23

2.1 Comparison of the *distinguishing* PET-OT detector concept previously proposed in the literature and the *sieving* PET-OT detector concept proposed by this work 27
2.2 Simulation and reconstruction framework developed for the investigation of monolithic-detector PET systems 30
2.3 Simplified example of a fluence image 33

2.4 Example of minimum and maximum sum_{fi} training values used for the target space reduction applied by the kNN algorithm 35
2.5 Target space reduction applied by the kNN algorithm, illustrated in two and three dimensions 35
2.6 Four scintillation event points used to investigate the *CoG* feature 38
2.7 Architecture of the CNN designed for this work 39
2.8 Schematic of the proposed PET-OT system and enlargement of a bi-modal detector module 43
2.9 Image of the transverse slice at the axial centre of the Derenzo phantom . 48
2.10 3D rendering of the Digimouse Atlas 49
2.11 Mesh representation of the tumour-bearing mouse phantom used for the simulation of the optical imaging subsystem 50

3.1 Outcome of the initial trial for the PET simulation and reconstruction framework employing the *ReSCoGs A-kNN* algorithm 54
3.2 Effect of the POI estimation resolution on the final reconstructed image . 55
3.3 Six different fluence images obtained at the same crystal face lying on the xy-plane at z = 25 mm for the same scintillation event located at the (12.5, 18.5, 22.5) mm crystal coordinates. Each one from a photosensor with a different number of channels 56
3.4 Effect of the number of channels per photosensor on the x-coordinate of the *CoG* feature 58
3.5 Effect of the number of channels per photosensor on the y-coordinate of the *CoG* feature 58
3.6 2D scatter-plot of all the *CoGs* obtained from all the POIs in the training grid whose fluence images were recorded by a photosensor lying on the xy-plane 59
3.7 2D scatter-plot of the *CoGs* obtained for all training events whose x,y co-ordinates were 22.5 mm and 22.5 mm 60
3.8 sum_{fi} values for all the training events whose fluence image on an xy-plane photosensor at z = 25 mm had an i_{max} value of 18 61
3.9 Effect of the target space reduction on the subset of CoGs being considered by the *ReSCoGs A-kNN* algorithm 62
3.10 Minimisation of the global MAE of estimation as a function of k and n_p for 1 million randomly distributed POIs in a 25 x 25 x 25 mm crystal with two 8 x 8-channel photosensors perpendicularly coupled to two of its faces 63

3.11 Performance of the optimised *ReSCoGs A-kNN* algorithm with respect to the crystal depth for two photosensor configurations 64
3.12 Performance of the optimised *ReSCoGs A-kNN* algorithm with respect to the number and arrangement of crystal faces being coupled to 8 x 8-channel photosensors 65
3.13 Performance of the optimised *ReSCoGs A-kNN* algorithm with respect to the number of photosensor channels in each of two perpendicular photosensing faces 66
3.14 Noise-inflicted projection image corresponding to one of the 10 plenoptic detectors of the precursor system 67
3.15 Tomographically reconstructed image of the two-point-source phantom imaged with the optical imaging precursor system 68
3.16 POI estimation error histograms along each dimension of the crystal obtained when using the *ReSCoGs A-kNN* algorithm 69
3.17 POI estimation error histograms along each dimension of the crystal obtained when using the CNN-based algorithm 69
3.18 Position dependence of the estimation error along each of the three dimensions for the *ReSCoGs A-kNN* algorithm 71
3.19 Position dependence of the estimation error along each of the three dimensions for the CNN-based algorithm 72
3.20 Position dependence of the estimation error averaged on the three dimensions for the *ReSCoGs A-kNN* algorithm 73
3.21 Position dependence of the estimation error averaged on the three dimensions for the CNN-based algorithm 74
3.22 Rendering of a Gate simulation of the proposed system 75
3.23 Spatial resolution of the PET subsystem on all three dimensions as a function of the position along its radial axis, measured in the presence and absence of the optical imaging subsystem 77
3.24 Geometrical efficiency of the PET subsystem as a function of the position of a point source along its axial dimension 78
3.25 PET imaging capabilities of the proposed system displayed as the central slice along the axial dimension of the reconstructed image obtained for the Derenzo phantom using the *ReSCoGs A-kNN* algorithm in the framework 79
3.26 PET imaging capabilities of the proposed system displayed as the transverse slice at the axial centre of the reconstructed image obtained for the Derenzo phantom using the CNN-based algorithm in the framework . . . 80

3.27 Effect of the POI estimation resolution on the final PET reconstructed image for the proposed system 81
3.28 Image reconstruction results for the simulation of the tumour-bearing mouse phantom 83
3.29 Light propagation simulation results for the RFL-bound tumour within the mouse phantom 84
3.30 Noise-inflicted projection images corresponding to the 10 plenoptic detectors of the optical imaging subsystem 86
3.31 Reconstruction result for the simulated RFL-expressing tumour within the mouse phantom 87

Glossary of acronyms

CASToR Customizable and Advanced Software for Tomographic Reconstruction

CMOS Complementary metal-oxide semiconductor

CNN Convolutional neural network

CoG Centre of Gravity

FOV Field of view

FWHM Full width at half maximum

kNN k-nearest neighbours

LoR Line of Response

MAE Mean absolute error

MC Monte Carlo

MLEM Maximum likelihood expectation minimization

MOMIA monomolecular multimodality imaging agents

NEMA National Electrical Manufacturers Association

OT Optical Tomography

PBRT Physically Based Rendering Toolkit

PDE Photon detection efficiency

PET Positron Emission Tomography

PMT Photomultiplier tube

PO Plenoptic

POI Point of interaction

ReLU Rectified Linear Unit

ReSCoGs Reduced-Space Centre of Gravity

RFL Red firefly luciferase

SiPM Silicon photomultiplier

Scientific contributions

Conferences

- Pazos Clemens, L., Peter, J.; Oral presentation: Investigating monolithic-detector PET design by direct simulation of scintillation photons. 2022 Crystal Clear Collaboration meeting, CERN, 2022.
- Pazos Clemens, L., Peter, J.; Poster: Investigating monolithic-detector PET design, direct simulation of scintillation photons and evaluation of its impact on image reconstruction. 2022 European Congress of Medical Physics, Dublin, Ireland, 2022.
- Pazos Clemens, L., Peter, J.; Poster: Integrated preclinical PET-OT employing monolithic modules comounted with plenoptic cameras. 2022 IEEE Nuclear Science Symposium & Medical Imaging Conference, Milan, Italy, 2022.
- Pazos Clemens, L., Peter, J.; Poster: Integrated preclinical PET-OT employing monolithic modules comounted with plenoptic cameras. 2022 DKFZ PhD Poster Presentation, Heidelberg, Germany, 2022.
- Pazos Clemens, L., Peter, J.; Poster: Integrated preclinical PET-OT employing monolithic modules comounted with plenoptic cameras. 2023 DKFZ PhD Retreat, Heilbronn, Germany, 2023.
- Pazos Clemens, L., Peter, J.; Oral presentation: 3D gamma-ray interaction position identification in monolithic crystals: simulation comparison of a convolutional neural network and k-nearest neighbors algorithm for different crystal-sensor geometries. 2023 AI & Informatics in Nuclear Medicine Symposium, Groningen, Netherlands, 2023.

Articles

- Pazos Clemens, L., Peter, J. (submitted in 2023). Simulation study of the feasibility of an integrated preclinical PET-OT system based on monolithic crystals and plenoptic detectors[1]. IEEE Transactions on Radiation and Plasma Medical Sciences.

1. Part of the content of this work is included in this article.

References

[1] James E Bowsher et al. “Bayesian reconstruction and use of anatomical a priori information for emission tomography”. In: *IEEE transactions on medical imaging* 15.5 (1996), pp. 673–686.

[2] DL Prout, RW Silverman, and Arion Chatziioannou. “Detector concept for OPET-A combined PET and optical imaging system”. In: *IEEE transactions on nuclear science* 51.3 (2004), pp. 752–756.

[3] Jin Ho Jung et al. “Development of a dual modality imaging system: a combined gamma camera and optical imager”. In: *Physics in Medicine & Biology* 54.14 (2009), p. 4547.

[4] Changqing Li et al. “Simultaneous PET and multispectral 3-dimensional fluorescence optical tomography imaging system”. In: *Journal of Nuclear Medicine* 52.8 (2011), pp. 1268–1275.

[5] Jörg Peter. “Dual-Modality Preclinical PET-OI Concepts and Instrumentation”. In: *Molecular Imaging of Small Animals: Instrumentation and Applications*. Springer, 2014, pp. 447–465.

[6] Florian Stuker, Jorge Ripoll, and Markus Rudin. “Fluorescence molecular tomography: principles and potential for pharmaceutical research”. In: *Pharmaceutics* 3.2 (2011), pp. 229–274.

[7] Joseph Culver, Walter Akers, and Samuel Achilefu. “Multimodality molecular imaging with combined optical and SPECT/PET modalities”. In: *Journal of Nuclear Medicine* 49.2 (2008), pp. 169–172.

[8] Andrea Gonzalez-Montoro et al. “Evolution of PET detectors and event positioning algorithms using monolithic scintillation crystals”. In: *IEEE Transactions on Radiation and Plasma Medical Sciences* 5.3 (2021), pp. 282–305.

[9] Daniel Unholtz et al. “Image Formation with a Microlens-Based Optical Detector: a 3D Mapping Approach”. In: *Journal Applied Optics* 48.10 (2009), pp. D273–D279.

[10] Liji Cao and Jörg Peter. “Iterative reconstruction of projection images from a microlens-based optical detector”. In: *Optics express* 19.13 (2011), pp. 11932–11943.

[11] Dale L Bailey et al. *Positron emission tomography*. Vol. 2. Springer, 2005.

[12] Simon R Cherry et al. *Physics in nuclear medicine*. Vol. 3. Soc Nuclear Med, 2003.

[13] Kenneth S Krane. *Introductory nuclear physics*. John Wiley & Sons, 1991.

[14] Maurizio Conti and Lars Eriksson. “Physics of pure and non-pure positron emitters for PET: a review and a discussion”. In: *EJNMMI physics* 3 (2016), pp. 1–17.

[15] P Moskal, K Dulski, N Chug, et al. *Positronium imaging with the novel multiphoton PET scanner Sci*. 2021.

[16] Savely G Karshenboim. “Precision study of positronium: Testing bound state QED theory”. In: *International Journal of Modern Physics A* 19.23 (2004), pp. 3879–3896.

[17] Kengo Shibuya et al. “Limit of spatial resolution in FDG-PET due to annihilation photon non-collinearity”. In: *World Congress on Medical Physics and Biomedical Engineering 2006: August 27–September 1, 2006 COEX Seoul, Korea “Imaging the Future Medicine”*. Springer. 2007, pp. 1667–1671.

[18] Lukas M Carter et al. “The impact of positron range on PET resolution, evaluated with phantoms and PHITS Monte Carlo simulations for conventional and non-conventional radionuclides”. In: *Molecular imaging and biology* 22 (2020), pp. 73–84.

[19] Glenn F Knoll. *Radiation detection and measurement*. John Wiley & Sons, 2010.

[20] Raj Kumar Parajuli et al. “Development and applications of Compton Camera—a review”. In: *Sensors* 22.19 (2022), p. 7374.

[21] SJ Jeon et al. “Pixelated scintillator-based compact radio thin layer chromatography scanner for radiopharmaceuticals quality control”. In: *Journal of Instrumentation* 12.11 (2017), T11003.

[22] JA Brown et al. “Absolute light yield of the EJ-204 plastic scintillator”. In: *Nuclear Instruments and Methods in Physics Research Section A: Accelerators, Spectrometers, Detectors and Associated Equipment* (2023), p. 168397.

[23] Fabrizio Davı. "A brief overview of existence results and decay time estimates for a mathematical modeling of scintillating crystals". In: *Mathematical Methods in the Applied Sciences* 44.18 (2021), pp. 13833–13854.

[24] Matthew Lowdon et al. "Evaluation of scintillator detection materials for application within airborne environmental radiation monitoring". In: *Sensors* 19.18 (2019), p. 3828.

[25] David Jenkins. "Scintillator detectors for gamma-ray detection". In: *Radiation Detection for Nuclear Physics*. 2053-2563. IOP Publishing, 2020, 5-1 to 5–31. ISBN: 978-0-7503-1428-2. DOI: 10.1088/978-0-7503-1428-2ch5. URL: https://dx.doi.org/10.1088/978-0-7503-1428-2ch5.

[26] Piotr J Slomka, Tinsu Pan, and Guido Germano. "Recent advances and future progress in PET instrumentation". In: *Seminars in nuclear medicine*. Vol. 46. 1. Elsevier. 2016, pp. 5–19.

[27] Simon R Cherry et al. *PET: physics, instrumentation, and scanners*. Springer, 2006.

[28] Artem Zatcepin and Sibylle I Ziegler. "Detectors in positron emission tomography". In: *Zeitschrift für Medizinische Physik* 33.1 (2023), pp. 4–12.

[29] Carl K. Hoh. *Positron Emission Tomography: Physics, Instrumentation, Data Analysis*.

[30] Christoph W Lerche et al. "Maximum likelihood positioning and energy correction for scintillation detectors". In: *Physics in Medicine & Biology* 61.4 (2016), p. 1650.

[31] Jihoon Kang et al. "PET detector configuration with thick light guide and GAPD array having large-area microcells". In: *IEEE Nuclear Science Symposuim & Medical Imaging Conference*. IEEE. 2010, pp. 2495–2499.

[32] ND Volkow, NA Mullani, and B Bendriem. "Positron emission tomography instrumentation: an overview." In: *American journal of physiologic imaging* 3.3 (1988), pp. 142–153.

[33] WW Moses et al. "OpenPET: A flexible electronics system for radiotracer imaging". In: *2009 IEEE Nuclear Science Symposium Conference Record (NSS/MIC)*. IEEE. 2009, pp. 3491–3495.

[34] Kei Wagatsuma et al. "Direct comparison of brain [18F] FDG images acquired by SiPM-based and PMT-based PET/CT: phantom and clinical studies". In: *EJNMMI physics* 7.1 (2020), pp. 1–14.

[35] P Lecoq and S Gundacker. “SiPM applications in positron emission tomography: toward ultimate PET time-of-flight resolution”. In: *The European Physical Journal Plus* 136.3 (2021), p. 292.

[36] Ilia Britvitch et al. “Characterisation of Geiger-mode avalanche photodiodes for medical imaging applications”. In: *Nuclear Instruments and Methods in Physics Research Section A: Accelerators, Spectrometers, Detectors and Associated Equipment* 571.1-2 (2007), pp. 308–311.

[37] Jun Kataoka et al. “Recent progress of MPPC-based scintillation detectors in high precision X-ray and gamma-ray imaging”. In: *Nuclear Instruments and Methods in Physics Research Section A: Accelerators, Spectrometers, Detectors and Associated Equipment* 784 (2015), pp. 248–254.

[38] Hao Peng and Craig S Levin. “Recent developments in PET instrumentation”. In: *Current pharmaceutical biotechnology* 11.6 (2010), pp. 555–571.

[39] Valeri Saveliev. “The recent development and study of silicon photomultiplier”. In: *Nuclear Instruments and Methods in Physics Research Section A: Accelerators, Spectrometers, Detectors and Associated Equipment* 535.1-2 (2004), pp. 528–532.

[40] V Golovin and Valeri Saveliev. “Novel type of avalanche photodetector with Geiger mode operation”. In: *Nuclear Instruments and Methods in Physics Research Section A: Accelerators, Spectrometers, Detectors and Associated Equipment* 518.1-2 (2004), pp. 560–564.

[41] L Piatek. “Physics and operation of the MPPC silicon photomultiplier”. In: *http:// www.hamamatsu.com/ us/en/community/optical_sensors_sensors/sipm/physics _of_mppc* (2014).

[42] Andrea Gonzalez-Montoro et al. “Evolution of PET detectors and event positioning algorithms using monolithic scintillation crystals”. In: *IEEE Transactions on Radiation and Plasma Medical Sciences* 5.3 (2021), pp. 282–305.

[43] Xin Wang et al. “In vivo validation of dual-modality system for simultaneous positron emission tomography and optical tomographic imaging”. In: *Journal of Innovative Optical Health Sciences* 4.02 (2011), pp. 165–171.

[44] Hideaki Tashima et al. “A feasibility study of the 3D fluorescent image reconstruction for the simultaneous PET and fluorescent CT imaging system using depth of interaction PET detector”. In: *Medical Imaging 2008: Physics of Medical Imaging*. Vol. 6913. SPIE. 2008, pp. 1286–1293.

[45] David Sarrut et al. “Advanced Monte Carlo simulations of emission tomography imaging systems with GATE”. In: *Physics in Medicine & Biology* 66.10 (2021), 10TR03.

[46] Thibaut Merlin et al. “CASToR: a generic data organization and processing code framework for multi-modal and multi-dimensional tomographic reconstruction”. In: *Physics in Medicine & Biology* 63.18 (2018), p. 185005.

[47] Shichao Zhang et al. “A novel kNN algorithm with data-driven k parameter computation”. In: *Pattern Recognition Letters* 109 (2018), pp. 44–54.

[48] Cristian C Constantinescu and Jogeshwar Mukherjee. “Performance evaluation of an Inveon PET preclinical scanner”. In: *Physics in Medicine & Biology* 54.9 (2009), p. 2885.

[49] Yann LeCun, Yoshua Bengio, and Geoffrey Hinton. “Deep learning”. In: *nature* 521.7553 (2015), pp. 436–444.

[50] Eric Berg and Simon R Cherry. “Using convolutional neural networks to estimate time-of-flight from PET detector waveforms”. In: *Physics in Medicine & Biology* 63.2 (2018), 02LT01.

[51] Adam Paszke et al. “Pytorch: An imperative style, high-performance deep learning library”. In: *Advances in neural information processing systems* 32 (2019).

[52] M. Levoy. “Light Fields and Computational Imaging”. In: *Computer* 39.8 (2006), pp. 46–55. DOI: 10.1109/MC.2006.270.

[53] Giacomo Borghi, Valerio Tabacchini, and Dennis R Schaart. “Towards monolithic scintillator based TOF-PET systems: practical methods for detector calibration and operation”. In: *Physics in Medicine & Biology* 61.13 (2016), p. 4904.

[54] Joerg Peter et al. “Development and initial results of a tomographic dual-modality positron/optical small animal imager”. In: *IEEE Transactions on Nuclear Science* 54.5 (2007), pp. 1553–1560.

[55] National Electrical Manufacturers Association (NEMA). “NEMA NU4-2008: performance measurements of small animal positron emission tomographs”. In: (2008).

[56] Andrey S Shugarov et al. “CCD272-64 and GSENSE400BSI-GP CMOS quantum efficiency measurement in EUV and VUV”. In: *International Conference on Space Optics—ICSO 2020*. Vol. 11852. SPIE. 2021, pp. 2214–2222.

[57] Belma Dogdas et al. “Digimouse: a 3D whole body mouse atlas from CT and cryosection data”. In: *Physics in Medicine & Biology* 52.3 (2007), p. 577.

[58] Mizuki Nishino et al. “Response assessment in metastatic melanoma treated with ipilimumab and bevacizumab: CT tumor size and density as markers for response and outcome”. In: *Journal for immunotherapy of cancer* 2.1 (2014), pp. 1–12.

[59] Karolin Pohle et al. “68Ga-NODAGA-RGD is a suitable substitute for 18F-Galacto-RGD and can be produced with high specific activity in a cGMP/GRP compliant automated process”. In: *Nuclear medicine and biology* 39.6 (2012), pp. 777–784.

[60] William W Moses. “Fundamental limits of spatial resolution in PET”. In: *Nuclear Instruments and Methods in Physics Research Section A: Accelerators, Spectrometers, Detectors and Associated Equipment* 648 (2011), S236–S240.

[61] Mahsa Amirrashedi, Habib Zaidi, and Mohammad Reza Ay. “Advances in preclinical PET instrumentation”. In: *PET clinics* 15.4 (2020), pp. 403–426.

[62] Seokchan Yoon et al. “Deep optical imaging within complex scattering media”. In: *Nature Reviews Physics* 2.3 (2020), pp. 141–158.

[63] Thomas Mikosch. “Regular variation, subexponentiality and their applications in probability theory”. In: (1999).

[64] Pietro Carra et al. “A neural network-based algorithm for simultaneous event positioning and timestamping in monolithic scintillators”. In: *Physics in Medicine & Biology* 67.13 (2022), p. 135001.

[65] Amirhossein Sanaat and Habib Zaidi. “Depth of interaction estimation in a preclinical PET scanner equipped with monolithic crystals coupled to SiPMs using a deep neural network”. In: *Applied Sciences* 10.14 (2020), p. 4753.

[66] Srilalan Krishnamoorthy et al. “Performance evaluation of the MOLECUBES β-CUBE—a high spatial resolution and high sensitivity small animal PET scanner utilizing monolithic LYSO scintillation detectors”. In: *Physics in Medicine & Biology* 63.15 (2018), p. 155013.

[67] Peng Peng, Martin S Judenhofer, and Simon R Cherry. “Compton PET: a layered structure PET detector with high performance”. In: *Physics in Medicine & Biology* 64.10 (2019), 10LT01.

[68] Xiaoming Jiang et al. “A surface recognition approach for in vivo optical imaging applications using a micro-lens-array light detector”. In: *Biomedical Optics*. Optica Publishing Group. 2012, BTu3A–1.

[69] Andrea Gonzalez-Montoro et al. “Validation of photon collimation techniques for monolithic PET detector calibration”. In: *IEEE Transactions on Radiation and Plasma Medical Sciences* 5.6 (2020), pp. 783–792.

Acknowledgements

You are not a drop in the ocean, you are the entire ocean in a drop
∼ often attributed to Rumi

A short story of gratitude, giants and being.
Shoulders carry, shoulders hurt, shoulders welcome affectionate comfort. Shoulders are what I stand on, my starting point, my ground and support. Like everyone, like everything, this work and I stand on the shoulders of giants. Everything I do, everything I achieve, everything I fail can happen because of what others before me have done, because of what others around me do along my side and because of the strength that those with me directly gift to me. This work was no exception. After quite a lot of effort, hardship, fun and growth, and one hundred thirteen thousand one hundred thirteen lines of code later this work, this chapter, reaches its end, for now. This was only possible because of you. It is no coincidence that one of the main tools with which this work was carried out is named after the ancient African concept of Ubuntu.
I am because we are.
In humble realisation of this I want to thank those who supported me along the completion of this work.
To those who shared with me their experienced advice and supervision in a modest manner that transcended the professional I extend my gratitude.
To those who shared this period of space-time, distended from my desk to my life, with me, colouring it with their presence, their smile, their help and their input I gift my deepest

appreciation.
To those who planted in me the seeds of curiosity and passion that bring me here both long ago and over and over again I express my sincerest admiration.
To those who have stayed by my side across the years and the globe challenging any obstacle and knowing no limit to their eagerness for adventure I owe my willingness to keep going.
To those who have built the home in which I grew in the past few seasons I present my warmest affection.
A chi mi ha accompagnato attraverso le valli nella scoperta di nuove cime in condivisione d'ideali, insegnandomi la bellezza e la verità del essere comunità soffio il mio più grande grazie.
A los que han sido mi familia extendida lejos de casa, que me han dejado reposar en sus ramas y me han sostenido con sus raíces les agradezco con mi más cálido cariño.
A los que han estado ahí cada día, desde el principio hasta el final, antes o ahora siendo para que yo sea, los abrazo con el más profundo e inefable amor que habita en mí.



† *by Edvard Munch*